Experimental Process Development for Scanning Thermal Microscopy in Air and Vacuum

Sai Kan Tam

MSc by Research

University of York

Physics

February 2017

Abstract

This thesis explores the procedure of making thermal and force measurements using a scanning thermal microscope (SThM) in both air and vacuum environments. The atomic force microscopy(AFM) and SThM literature will be reviewed, including thermal transport at the tip sample interface and methods of determining the spring constant of the cantilever. The thesis will then discuss the instruments that are used in the experiment, and the procedure for making thermal and force measurements. Thermal and force measurements were obtained with five different samples that cover different thermal and mechanical properties. Silicon, silicon carbide, mica and PTFE along with a thin film of gold for which the thermal conductivity would be determined. The topography analysis, interpretation of force and thermal curves will be discussed and recommendations made about the best ways to attempt quantitative measurements using these techniques.

Contents

Abstract ii

Content iii

List of Tables v

List of Figures vi

Acknowledgement xii

Declaration xiii

Chapter 1 Introduction 1

1.1. Motivation and Introduction 1

1.2. Atomic Force Microscopy 4

1.3. Scanning Thermal Microscopy 7

1.4. Objectives of this project 12

Chapter 2 Principle of force and temperature measurements using scanning probes 13

2.1. Heat Transport in SThM 13

2.2. Characteristics of a force curve measured by AFM. 18

2.3. Characteristic of a thermal measurement and thermal calibration 24

Chapter 3 Experimental Method 29

Part I: Instrumentation and preparation 29

3.1. SThM instrumentation and integration to AFM 29

3.2. Sample selection 34

Part II: Experimental procedures 36

3.3. Preparation for the force and thermal measurements 36

3.4. Methods of topography measurements 40

3.5. Force measurement and roughness procedure 44

3.6. Calibration of thermal probe and measurements procedure 47

Chapter 4 Topography and force curves measured using contact mode and thermal probes .. 54

4.1. Physical dimensions from SEM and spring constant results 55

4.2. Topography and roughness analysis 60

4.3. Force measurements comparison between samples 68

4.4. Discussion of the results 75

Chapter 5 SThM for thermal conductivity measurements 78

5.1. Thermal calibration and probe signal from the data logger 78

5.2. Thermal map and the thermal measurements 88

5.3. Discussion and interpretation of thermal results and thermal conductivity 108

Chapter 6 Conclusion and further developments 116

List of reference 122

List of tables

Table 3.1 A table summarising the properties of the materials chosen for this thesis. The table includes the thermal conductivity, hardness and the elastic modulus of the samples. [35], [36], [37], [38] 34

Table 4.1 Dimension measurements and spring constant calculation for all the probes. [35], [36], [38] 56

Table 4.2 Summary of the topography of each material. 67

Table 4.3 Table presenting the sensitivity a from inverting the overall average slope of silicon carbide. 68

Table 4.4 Retract force measurements using thermal probes. 72

Table 5.1 Table of the conversion coefficient of the thermal probes used in thermal measurements. 86

Table 5.2 Table of temperature measurements from the thermal probe in air, with a current of 0.8mA. 97

Table 5.3 Table of temperature measurements from the thermal probe in vacuum, with a current of 0.8mA. 103

Table 5.4 Table of temperature measurements from thermal probe, measured in 0.8mA. 105

Table 5.5. A summary table for overall the data. The table showed the material, the thermal conductivity, the elastic modulus, the retract force, the change in temperature for approach, retract and for the data logger. The new elements are the deformation column, where measuring the temperature dropped after the tip deforms the sample. The percentage heat loss is calculating the percentage ratio of approach to data logger. 109

List of figures

Figure 1.1 A generic diagram of the main parts of an atomic force microscope, it consists of a piezoelectric tube as the main driver of the specimen, a laser and a photodiode for feedback system a cantilever for scanning. [10] 4

Figure 1.2 a) A conventional AFM topography image of a gold sample along with b) the associated thermal image. The conversion coefficient for the scale bar to voltage is 2.34Å/V. 7

Figure 1.3 a) A typical shape of a fabricated probe. b) shows the structure of a Wollaston wire. [18] 9

Figure 2.1 A schematic diagram showing the thermal pathways of a probe in contact with a sample. a) This diagram shows the SThM operating in ambient environment. The setup is the probe when operating in active mode. The heat flow is directed from the probe to the sample. The heat transport by air, G_{gas} is also shown in the diagram. Note that G_{gas} does not exist when the setup is operating in vacuum. b) A detailed diagram of the dotted circle area in figure 2.1a), showing the heat flow paths from the tip to the sample. In both the environments, the heat transported by the radiation G_{rad} and by mechanical contact G_{mc} exist. The blue area in the ambient environment represents the water droplets formed by condensation. The heat transport via water is represented by G_{w}. Note that G_{w} does not exist in vacuum. The diagrams are modified from Poon [25] presentation. 13

Figure 2.2. A typical force measurement diagram of SiC sample and operated in air. The diagram described the probe position at each point from the starting position where the probe starts recording the data, approaching to contact point where the probe makes contact with the sample surface. The tip keeps pressing on until the tip stop at the pre-set displacement range labelled as tip stopping point. The tip will then retract from the surface, the surface adhesive force is keeping the tip on the surface and bending the cantilever, a hysteresis is formed during the tip is retracting. When the tip gained enough force that overcomes the surface force, the tip will snap out and retract to the starting position. 19

Figure2.3. Schematic diagram of force displacement curve. V_0 is the reference voltage when the tip is away from the surface and the sample is exerting no force on it. The optical lever sensitivity α is measured at the retract regime, note that the sensitivity is the inverse of the gradient at the retract curve. [29] 21

Figure 2.4 A schematic diagram demonstrating the reference cantilever method using a large-scale cantilever against the AFM cantilever. a) The AFM cantilever is pressed on a large-scale cantilever that has known property. b) When a force is applied by the AFM cantilever, both cantilevers will bend as different rate, since both cantilevers are exerting the same force, the spring constant is measured by the deflection of the cantilever. [33] 23

Figure 2.5 A schematic thermal measurement of SiC in air using a fabricated resistor probe in active mode. The arrows indicate the motion and position of the probe throughout the measurement. The position at which the probe snaps into the surface is marked as the contact point. 24

Figure 2.6 A typical thermal result of SiC measured in vacuum operated in active mode. The main characteristic is there is no heat loss before the tip reaches the contact point. 25

Figure 2.7 A force curve and a thermal curve to verify the interpretation of the thermal curve. The intersection of both curves at the contact point and the snap out point are used to verify the temperature change on the thermal curve. 26

Figure 2.8 The typical shape for the thermal calibration in air. The calibration curve includes the Peltier temperature and the probe voltage both plotted against time. 27

Figure 3.1 A photograph of SThM set up at the University of York. Including the data logger, probe power supply, Peltier power supply and detection circuit, the vacuum facility and the AFM. The AFM control PC is the main control for the AFM. 30

Figure 3.2 a) A comparison between the thermal probe holder (left) and the contact probe holder (right). b) A photograph of the thermal probe connector with a thermal probe attached. 31

Figure 3.3 A circuit diagram of the power supply of the probe. The probe is represented as a variable resistor as each probe will have a variation in resistance. The arrow showed the two variable resistors that controls the main voltage applying to the tip and the fine adjustment to the voltage, labelled in the diagram. [34] 32

Figure 3.4 The AFM feedback module panel showing the cable connection and the switch for feeding the thermal signal into the AFM. 33

Figure 3.5 An SEM image illustrating a) the width and the length measurements from top view, b) thickness measurements from the side view. 36

Figure 3.6 The estimation of the tip apex of a) the thermal probe and b) the contact probe. 37

Figure 3.7 The figure of the sample arrangement on the heater. 38

Figure 3.8 A schematic diagram showing the measurements made in a force curve. The difference of V_{min} and V_0 is the adhesive force dF being measured. The line of best fit for sensitivity measurements is noted. 45

Figure 3.9 A typical result from the data logger for thermal calibration. 48

Figure 3.10 Figure of thermal calibration in vacuum heated at 60℃, the temperature jump during cooling is marked. 49

Figure 3.11 A typical measurement of probe voltage against Peltier temperature, a line is fitted for estimating the conversion coefficient from voltage to temperature. .. 50

Figure 3.12 Illustration showing a close up of a thermal hysteresis with explanation of how to measure the change in temperature. 52

Figure 4.1 shows the SEM image for all probes used in this project. Figure a)-c) are the thermal probes A-C and d) is the contact probe D, the figures above were measured with the scale bar of 10 μm. 55

Figure 4.2 The impurities on the cantilever of probe A, the impurity is located towards the holder on the left-hand side of the picture. This could potentially affect the spring constant estimation. 57

Figure 4.3 The SEM image of probe B with layer of palladium resistor coating peeling off after measuring a set of thermal measurement. The scale bar of the figure is 100nm. 59

Figure 4.4 Silicon carbide topography measured with a) contact probe and b) measured with thermal probe C. The figures represent a similar area of the silicon carbide. ... 60

Figure 4.5. Roughness analysis of gold thin film. 63

Figure 4.6. Roughness analysis of mica. 63

Figure 4.7. Roughness analysis of PTFE. 64

Figure 4.8. Roughness analysis of silicon. 64

Figure 4.9. Roughness analysis of silicon carbide. 65

Figure 4.10 Force measurement results of silicon carbide measured in air with a) the contact probe D and b) the thermal probe C. 69

Figure 4.11 A diagram illustrating the force measurements that exceeded the AFM limit. Two gradients were drawn and the intercepts were used to determining the adhesive force. 70

Figure 4.12. A diagram showing the typical force measurement result of silicon after the offset of sensor limit. 71

Figure 4.13 Force result of PTFE in vacuum, measured in three different areas showing the variation. 74

Figure 5.1 a) A generic result of data logger recording in air. The diagram illustrates each part of the curve during the experiment. From the beginning there is a potential difference drop for approach until the tip is in contact with the surface. Then the potential difference remained during the topography scanning. b) Continue the same diagram with labels of the measurement spikes, noise spikes and indication of the data logger change in temperature. The measurement spikes are indicating the temperature changes during the force and thermal measurements. The noise spikes are caused by the 40-second periodic instrumental noise. The data logger change in temperature indicates the temperature difference between the tip in contact and out of contact of the sample. 79

Figure 5.2 Data logger results of mica with 0.8mA in the environment of a) in air and b) in vacuum. The results are comparing the measurement spikes height to the temperature when the tip is not in contact in both environments. 81

Figure 5.3 The data logger results of thermal calibration with the probe current of 0.8mA a) in air and b) in vacuum. 83

Figure 5.4 Results of thermal calibration, graph of probe voltage against Peltier temperature measured in a) air and b) vacuum. 84

Figure 5.5 A graph of thermal calibration peak with both heating and cooling. 85

Figure 5.6 a) The unprocessed thermal map of SiC in air b) the processed thermal map of SiC in air. For both figures the conversion 10.02pm/V. 87

Figure 5.7 Thermal curve of PTFE measured in vacuum. The thermal curve presented is an average of 9 curves. The step jump is caused by different responses at each area. 89

Figure 5.8 Thermal curve of PTFE at 3 different areas measured in vacuum. 90

Figure 5.9 The thermal curves of a) PTFE and b) SiC measured in air. 91

Figure 5.10 The results for gold thin film in air. 93

Figure 5.11 Thermal results of Mica in air. 93

Figure 5.12 Thermal results of PTFE in air. 94

Figure 5.13 Thermal results of Silicon in air. 94

Figure 5.14 The results of silicon carbide in air. 95

Figure 5.15 Thermal results of thin film gold in vacuum. 99

Figure 5.16 Thermal results of Mica in vacuum. 100

Figure 5.17 Thermal results of PTFE in vacuum. 100

Figure 5.18 Thermal results of silicon in vacuum. 101

Figure 5.19 Thermal results of silicon carbide in vacuum. 101

Figure 5.20 The data logger results of silicon in air showing the sample cooling during the experiment. 107

Figure 5.21 Result of PTFE illustrating the method of calculating deformation temperature changes. 110

Figure 5.22 The approach temperature change against the thermal conductivity. 112

Figure 5.23 The approach temperature change against the thermal conductivity for small thermal conductivity. The gold is shown as a horizontal line as the thermal conductivity is not known. 113

Figure 5.24 The approach temperature change against the thermal conductivity for small thermal conductivity. The silicon values have plotted with the silicon oxide thermal conductivity of 1.1 W/m·K. 114

Acknowledgement

I would like to take this chance to thank my supervisors, Prof. Sarah Thompson and Dr. Siew Wai Poon for the unlimited encouragement, patience and care in this project. Without their excellent guidance, I probably would never complete this research.

I want to thank my parents for looking after me throughout the time I have been writing, their constant support and belief has helped me to pass through difficult times.

I want to thank a couple of my friends, Gordon Kam, Lichi Sun and Winky Wong for the spiritual support.

Declaration

I declare that this thesis is a presentation of original work and I am the sole author. This work has not previously been presented for an award at this, or any other, University. All sources are acknowledged as References.

Chapter 1 Introduction

1.1 Motivation and introduction

Classical thermal measurements have been developed for understanding thermal physics for decades. The classical theories of thermal transportation have been developed for investigating the thermal properties of materials such as thermal conductivity and the applications have been widely applied across everyday life. There are many techniques for making thermal measurements, for example the absolute technique method determines the thermal conductivity by placing the sample between the heat sink and a heat source, calculating the length of the heat flow through the sample and obtaining the thermal conductivity by Fourier's law. [1] There are other temperature sensors that use different mechanisms such as thermocouples and resistance thermometers.

When quantum physics was developed the technology and theories advanced further. There was a better understanding that thermal transport is different on a smaller length scale, for example the concept of heat carriers was introduced. [2] When making thermal measurements at a nanoscale, typically less than 100 nanometres [2], a different mechanism of thermal transportation would be expected. With the advance of fabrication technology, the construction of materials and electronic components became much smaller. Although classical methods such as the 3ω method [1] have advanced for thin film materials, the classical methods still require a large contact area. Non- contact methods for thermal conductivity, such as transient thermoreflectance techniques measure the thermoreflectance response of the material as a function of time using a laser and beam splitter [1]. The thermoreflectance method can detect the thermal conductivity of thin film with a few nanometres thick, but the spatial resolution with this method can only measure down to 400 nanometres due to the optical limit of diffraction. [3] Thermal measurements at smaller scale require other techniques. The scanning

thermal microscope is capable of measuring the temperature at 10 nanometres [4], it is a modification to an atomic force microscope, which leads to the introduction to atomic force microscopy.

Binnig introduced Atomic Force Microscopy (AFM) in 1986 [5], it is a technique which allows high spatial resolution measurements at the material surface. Later the AFM was modified to measure various properties, particularly the scanning thermal microscopy that is used in this thesis. The original AFM modified the scanning tunnelling microscope tip by sticking pieces of diamond on the end of the cantilever [5], [6]. In modern AFM the tip is no longer diamond, instead it is usually made of silicon and silicon nitride. [7] The AFM detects the Van der Waals force on the tip [8], the key features of AFM will be discussed in Section 1.2. AFM can provide images with spatial resolution better than 0.1 nm, with the advantage of using non-conductive materials and can be operated in vacuum. AFM has been widely used in material science in order to study the topographic, tribological, roughness and adhesion characteristics of materials. [7]

Shortly after AFM was introduced, scientists made modifications for temperature measurements [9], the modification took the advantage of the high spatial resolution scanning ability of AFM. The first Scanning Thermal Microscopy (SThM) instrument was introduced by Williams and Wickramasinghe in 1986 [9]. The principle of their SThM was similar to AFM, modifying the tip into a thermocouple that allows thermal measurements. As the tip makes contact with the sample surface, thermal energy transfers either from the sample to the thermocouple or vice versa, which changes the temperature dependent voltage across the thermocouple. The voltage measurement could be converted into temperature, along with the topography, creating a thermal map. Various types of SThM tip have been developed since using different types of mechanisms, for instance the thermoelectric effect and thermal

resistance. The details of the different types of probes will be discussed in Section 1.3. SThM gives a high spatial resolution thermal image, which makes this technique unique in studying thermal physics.

SThM now acts as one of the main tools for developing near field thermal physics and in material science. This thesis will attempt to explore its potential for measuring the thermal properties of materials at the nanoscale. The thesis will focus on the initial steps of developing a quantitative method for making thermal and force measurements, the method is capable of operating the SThM in both air and vacuum environment. Thermal and force measurements were obtained with five different samples covering different thermal and mechanical properties. The topography analysis, interpretation of force and thermal curves will be discussed.

The thesis will start by introducing the concept of AFM, the principle of how to make measurements and what modes they can be operated in, then move onto SThM by describing the different types of probes and the literature review on the application. Chapter 2 discusses the physics of thermal transport and how the heat flows in SThM. This then leads to the discussion on how to interpret the force and thermal measurements. Chapter 3 describes in detail the instruments being used in this thesis, the experimental setup and process and the choice of samples. Chapter 4 concentrates on the analysis of the force measurements while Chapter 5 concentrates on the analysis of the thermal measurements. Chapter 6 is the conclusion and suggestions for future development.

1.2 Atomic Force Microscopy

AFM systems operate on a vibration isolated platform, as AFM is measuring in high spatial resolution, any form of vibration could result in a large error in measuring the topography. A generic AFM features the following main parts: probe, piezoelectric tube to scan the sample, laser detector to measure the flexing of the cantilever, feedback controls and the computer control. A generic structure of an AFM is shown in Figure 1.1.

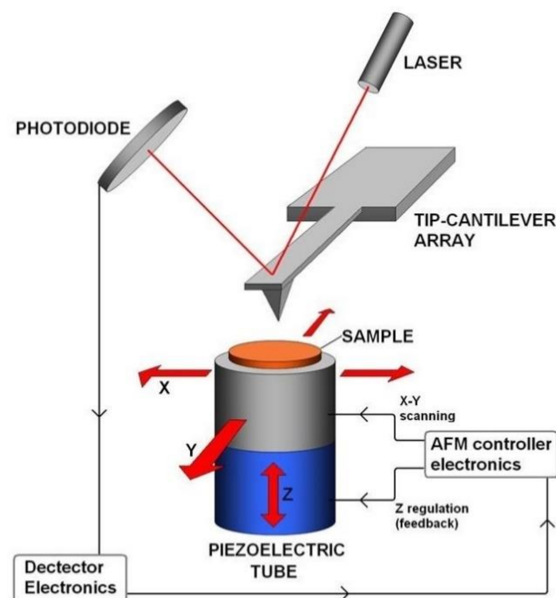

Figure 1.1 A generic diagram of the main parts of an atomic force microscope, it consists of a piezoelectric tube as the main driver of the specimen, a laser and a photodiode for feedback system a cantilever for scanning. [10]

In figure 1.1, the piezoelectric tube is placed beneath the sample. The piezoelectric materials, used as the main drivers in AFM are materials that expand or contract when an electrical potential is placed across them. They are usually ceramic materials with a typical expansion coefficient of 0.1nm per applied volt. [7] The piezotube is placed under the specimen stage to control the x-y direction of the sample. The piezotube to control the z direction is placed under the x-y piezotube that gives an independent control over z direction. The reason for that is the

z-piezotube is combined with a feedback circuit that requires an independent control. In some types of AFM, the z piezotube is placed on the cantilever holder.

A laser beam is set to reflect off the back of the cantilever to a photo diode that locates the tip in the z direction and the photodiode is connected to the feedback control circuit. When there is a force pulling the tip towards the surface it causes a bend in cantilever. The reflected laser beam position on the quadrant photodiode therefore changes, and this signal would be sent to the feedback circuit. The feedback circuit can then send a signal to the z piezotube to move the sample away from the tip so as to maintain the probe sample distance if desired. This mechanism works vice versa when there is a force pushing the tip away. The feedback mechanism can minimise the damage from an uneven surface, this is because the laser is reflecting the status of the cantilever when the tip feels a change in force. This method increased the sensitivity compare to a tradition stylus profiler. [7]

As the AFM detects the electrical signal from the photodiode to make changes and for force measurements, it is necessary to know the cantilever spring constant in order to convert the voltage signal back in units of nano-Newton if the force is needed to be known. AFM probes were then later developed to measure the magnetic properties in magnetic force microscopy, and to measure thermal properties in scanning thermal microscopy.

The AFM can be operated in two main modes, contact mode and non-contact mode. In contact scanning mode, the probe is in contact with the sample surface and a small force is applied from the cantilever to the surface to make it in contact. As the contact area of the probe is small, the force pressing on the sample must be small in order to prevent scratching of the sample surface or to the tip. [11] To measure the topography, the height of the probe is kept constant such that as the probe scans across the surface, the Van der Waals force will repel the tip according the height of the structure. This leads to a bend of the cantilever and changes the

laser reflection. The photodiode gives a signal to the computer for the z geometry measurement at each point. This method is often referred to as constant height scanning mode.

Constant force scanning mode is to maintain the force at a fixed value between the probe and the surface. This technique is similar to constant height scanning mode, except the deflection of the cantilever signal from the photodiode is sent to a feedback circuit. The feedback circuit controls the z piezotube to adjust the height of the probe such that the force between the probe and sample surface is maintained. Although both the contact scanning modes can provide topography images, there are some defects and limitations. For example, the force on the surface could cause friction and bend the probe, the probe could cause damage while moving on the surface. Due to these limitations, non-contact scanning mode was introduced.

Non-contact scanning mode is a technique which uses the resonance effect of the cantilever. Unlike the contact force mode, the tip does not constantly contact with the sample surface, instead the cantilever is oscillating using an additional piezoelectric element. The cantilever is oscillating at its resonant frequency, when the probe approach to the sample surface, the cantilever is no longer oscillating in free space. A phase shift is then detected in the resonant frequency of the cantilever because of the interaction force between the tip and the surface. [7] From this phase shift, we can determine whether the surface force is attractive or repulsive. The feedback circuit then sends a signal to adjust the z position in order to maintain the resonant frequency. [7] [8] While the tip moves across the x-y plane, along with the change in z position, the surface topography is then generated.

1.3 Scanning Thermal Microscopy

The general principle for SThM making thermal measurements is to use a tip with a physical property that is sensitive to temperature and can be monitored continuously. [12] This property is usually electrical potential. A constant electrical current is first passed through the fabricated material at the end of the tip, where the thermal sensor for detecting temperature is located. When the probe makes contact with the sample surface, the heat flow causes a change in temperature at the tip, this changes the electrical potential detected across the tip sensor. By monitoring the value of the voltage changes simultaneously with the topography, a thermal map is produced. SThM is usually carried out using the contact mode of AFM. The reason is the thermal measurements are related to the changes of voltage when the tip is in contact with the sample, a continuous contact with the sample is preferred for SThM.

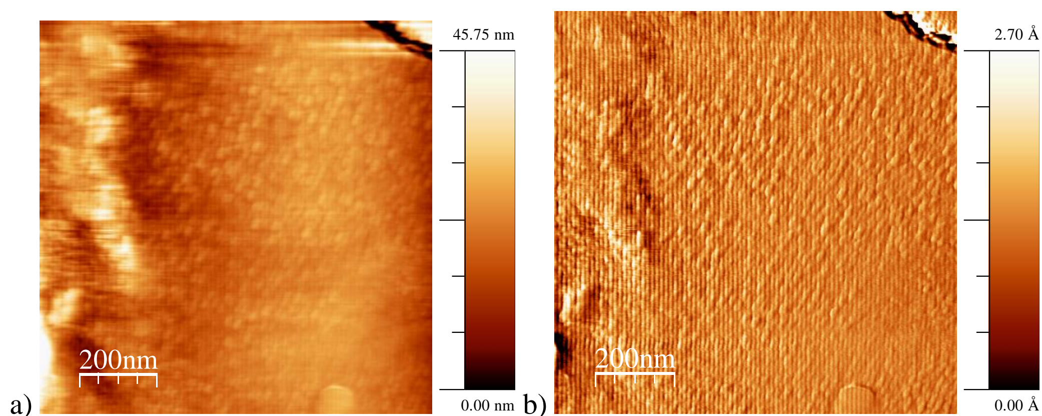

Figure 1.2 a) A conventional AFM topography image of a gold sample along with b) the associated thermal image. The conversion coefficient for the scale bar to voltage is 2.34Å/V.

Figure 1.2 shows a typical result from SThM, it is usually a topography map along with a thermal image. The pictures show that the thermal image provides some fine details to the topography, which could suggest the change in tip temperature could help in determining the surface structure. During the measurement, the tip and the sample could cause a misleading representation. This is because the contact area between the tip and the sample is dependent on

the physical properties of the sample surface and the thermal transport depends on the contact area, if the contact area changes, the thermal transport changes. [13]

There are several types of SThM probes that have been developed for measuring surface temperature, each can be classified using its temperature-dependent mechanism. [12] This thesis will mainly discuss the types of probe using the mechanisms of thermal voltage and change in electrical resistance; other thermal probes for example fluorescence and thermal expansion are not covered in this thesis.

A thermocouple profiler is one of the popular probes being used in SThM, where the temperature is measured by the change in electrical potential at the thermal junction. The thermocouple profiler was first developed by fabricating two types of materials to form a thermocouple at the end of an STM tip, the coating is typically about 100nm thick. [8] This type of probe uses the concept of thermoelectric effect, which offers a direct conversion between electrical voltage and temperature. [14] Thermocouple probes measure the voltage at the junction that is in contact with the sample surface and give a spatially resolved temperature measurement.

A resistance thermometer is another type of probe which monitors the temperature changes using a voltage measurement. The change in temperature is monitored by applying a constant current through the sensor. When the temperature of the probe changes, this causes a change in the electrical resistance of the sensor, which in turn causes a change in electrical potential across the tip. There is only one type of material fabricated on the AFM tip, therefore the technology required for making resistance thermometer is less complex [15].

Wollaston wire tips are one of the probes that measured the temperature by the change in resistance, introduced in 1994 by Pylkki *et al.* [16] The tip is made by bending a Pt wire, 5 µm-

core, into a V-shape and the rest of the wire forms a cantilever. The cantilever is coated with thick Ag of about 75μm in diameter. A mirror is then stacked on the back of the cantilever across the wires to provide reflection for AFM signalling and the end of the cantilever is mounted on a ceramic insulator. The Wollaston wire is responsive to temperature changes through its temperature dependence of resistance and has a high temperature coefficient of 0.0017 K^{-1} [12], however its large contact area of about 1 μm [17] limits the thermal research ability at smaller scale.

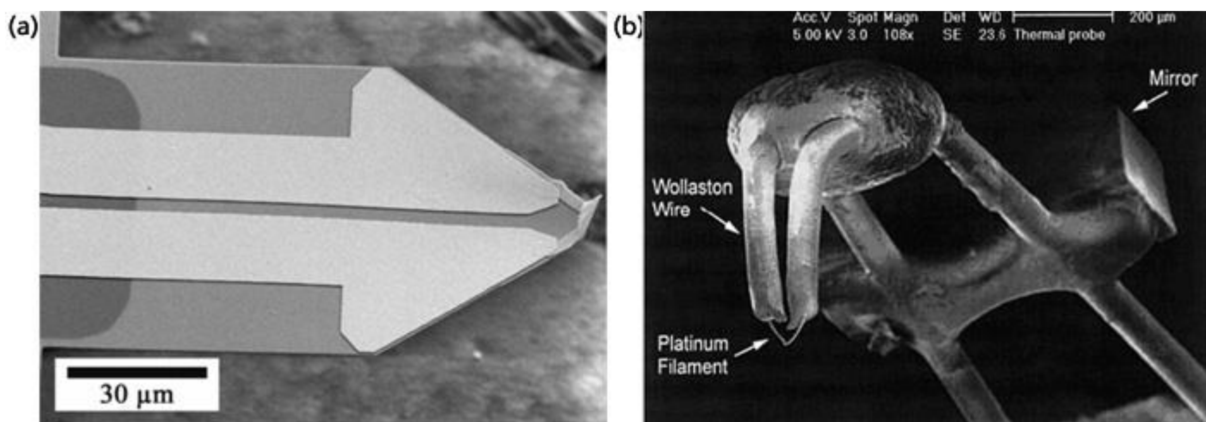

Figure 1.3 a) A typical shape of a fabricated probe. b) shows the structure of a Wollaston wire. [18]

A fabricated resistor probe is another type of probe that has improved the spatial resolution beyond that of a Wollaston wire. The cantilever is made of silicon nitride, with a thin palladium resistor fabricated at the end of the tip [14]. The fabricated resistor probes that will be used in this thesis are designed by Dobson *et al.* [15] in Glasgow, where the probes are produced by a batch fabrication process. The shape of the cantilever is formed through several processes of photolithography and micromachining, then the palladium resistor and the gold connectors are fabricated at the end of the tip. [15] The fabricated probe provides a contact area of radius about 50 nm, which is much smaller than the Wollaston wire. [12] Figure 1.3 shows the size difference between the Wollaston Wire and a fabricated probe.

SThM requires extra components to modify an AFM to measure the surface temperature of the sample, this is usually specific to the type of probes that the SThM is using and the capability of the AFM. In general, from the probes mentioned above, it is required to constantly monitor the small change in current through the probe by measuring the voltage across it. This means that the AFM probe holder must be modified for electrical connections. An additional power supply is required for providing the current through the probe. A signal recorder which can feed the signal back to the AFM for monitoring the voltage is also required. The details of the apparatus modification will be discussed in Chapter 3.

SThM can be operated in active and passive modes. Active mode is to pass a current through the probe to monitor the change in temperature, with no additional heating of the sample. The sample is heated up only by the tip, as the current in the probe causes Joule heating. This defines the direction of heat flowing from the tip towards the sample [19]. Passive mode is opposite to active mode, where the sample is heated independently by a heater. The current passing through the tip is smaller and only acts as thermometry, the sample heating being large enough to overcome the Joule heating by the probe. In this mode therefore, the heat flow is from the sample towards the probe. The advantage of active mode is that the mechanism of thermal transport is simpler than passive mode and the heat generation is localised to the tip area.

Research on nanothermal analysis using SThM has been actively developing in recent years. Majumdar and Shi [13] investigated the heat transfer mechanisms at SThM, which defined the main thermal transport paths at the tip-sample contact. Weaver *et al.* [20] developed methods of mass producing thermal resistive probes as well as designing different configurations. For example, they suggested there is a strong thermal coupling through air between the tips in dual cantilever probes. Gomes [17] studied the thermal exchange between probe and the sample, the result suggested that the environment where the SThM performs affects the heat transport.

Prater *et al.* [21] have reported using infrared AFM on nanoscale infrared spectroscopy, which could potentially open up nano thermal microscopy for biological use. Robinson *et al.* [22] reports the investigation of how shear force affects the contact area of heat transport on the nanoscale and proposed that the shear force at the thermal junction was dependent on the materials. Gorbunov *et al.* [11] measured the surface microthermal properties of low thermal conductivity materials and reported that local deformation contributes to the thermal measurements.

The SThM at the University of York has the unusual ability to undertake thermal measurements in vacuum. The advantage for vacuum is being able to eliminate the gas heating effect between the probe and the sample, the details of this will be discussed in chapter 2. High vacuum SThM is starting to get popular for nanothermal analysis. Menges *et al.* [23] built a high vacuum SThM at the IBM research laboratory for the research on thermometry at nanoscale. Kim *et al.* [24] reported using high vacuum SThM to quantify thermal fields in nanowires during electromigration.

1.4 Objectives of this project

The objective for this project is to explore the potential of using a scanning thermal microscope for quantitative thermal transport measurement. The scanning thermal microscope used in this project is based on the atomic force microscope at the University of York. The thesis will start by introducing the operation of the AFM, then move onto the development of the modification to SThM. The unusual property of the SThM at York is the ability to undertake thermal measurements in vacuum. As the SThM at York is still under development, this project aims to develop an experimental procedure for quantitative measurements in different environments.

Then the project will move onto exploring the topography and the surface features of the sample. The tip temperature changes will be measured using the SThM and compared within the set of five different samples that cover different thermal and mechanical properties: silicon, silicon carbide, mica and PTFE along with a thin film of gold for which the thermal conductivity would be determined. An attempt to explore the connection between the adhesive force and the temperature measurement will be presented as well as an attempt to obtain the thermal conductivity of a thin film sample, and compare this to the bulk value. The project will conclude with further suggestions on how to improve the experimental procedure and further possible research directions.

Chapter 2 Principle of force and temperature measurements using scanning probes

This chapter will include the basic theory of SThM. The chapter will start with discussing the heat transport in SThM followed by the theory behind force curves and methods for measuring the spring constant of the cantilever. The chapter will conclude with explaining the thermal measurements, from the heat transport point of view, the complementarity with force measurements and the thermal calibration.

2.1 Heat Transport in SThM

In SThM, the thermal properties are investigated by mapping the thermal properties to the topography of a sample. It is important to understand how the thermal energy flows in the system and what factors could limit the heat flow. There are four main mechanisms of thermal transport in SThM, Figure 2.1 illustrates the heat flow from a hot tip into a cold sample.

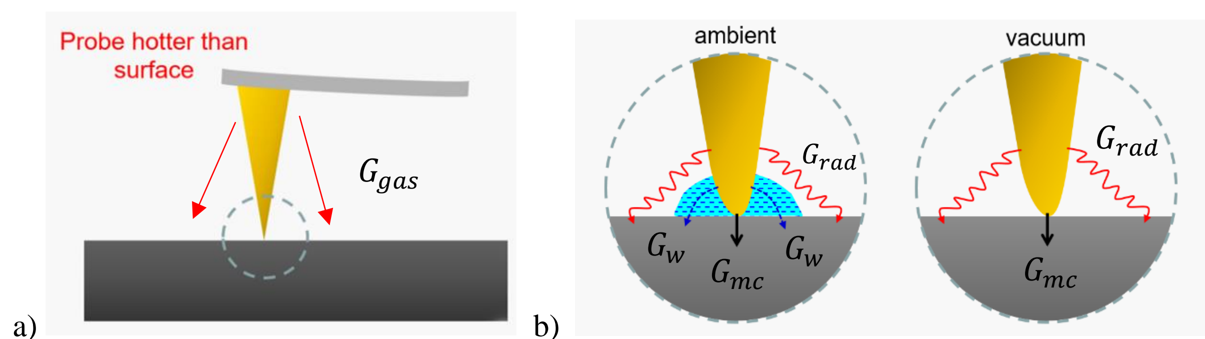

Figure 2.1 A schematic diagram showing the thermal pathways of a probe in contact with a sample. a) This diagram shows the SThM operating in ambient environment. The setup is the probe when operating in active mode. The heat flow is directed from the probe to the sample. The heat transport by air, G_{gas} is also shown in the diagram. Note that G_{gas} does not exist when the setup is operating in vacuum. b) A detailed diagram of the dotted circle area in figure 2.1a), showing the heat flow paths from the tip to the sample. In both the environments, the heat transported by the radiation G_{rad} and by mechanical contact G_{mc} exist. The blue area in the ambient environment represents the water droplets formed by condensation. The heat transport via water is represented by G_w. Note that G_w does not exist in vacuum. The diagrams are modified from Poon [25] presentation.

Figure 2.1a shows a setup of a probe contacting a sample surface, where the probe is heated to have a higher temperature than the sample. Figure 2.1b shows the thermal energy transfer in the environment of ambient and vacuum. The four main heat transport mechanisms are shown and represented by their thermal conductance. The G_{rad}, G_{gas}, G_{w}, G_{mc}, represent heat transport by radiation, gas conduction, solid-liquid conduction and mechanical conduction respectively. $G_{th,c}$ represents the effective thermal conductance of the overall system. The mathematical representation of $G_{th,c}$ is proposed by Shi and Majumdar [12] in equation (1)

$$R_{th,c} = \frac{1}{G_{th,c}} = \frac{1}{G_{rad}+G_{gas}+G_{w}+G_{mc}} \quad (1)$$

Equation (1) shows that the effective thermal resistance $R_{th,c}$, the reciprocal of effective thermal conductance, $G_{th,c}$, which is the sum of the thermal conductance of all mechanisms. Mechanical, or solid-solid conduction, is a direct energy exchange between the probe and the sample [8]. The conduction happens when both the probe and the sample are in contact, therefore during the thermal measurements the direct conduction must be taken into account. The solid-solid conduction is restricted by the contact area between the tip and the sample, this can be demonstrated by Fourier's law of heat in equation (2).

$$\dot{Q} = -kA\frac{dT}{dx} \quad (2)$$

Where $\dot{Q}$ is the local heat flux, k is the thermal conductivity of the material, A is the area of conduction, dT is the change in the temperature of two points and dx is the distance between the point of measurements. When applying equation (2) in SThM, A is the contact area between the probe and the sample surface. Fourier's law shows that $\dot{Q}$ is directly proportional to A,

therefore if the contact area of the tip gets infinitely small, the heat transport via conduction will be infinitely small.

Fourier's law described the thermal transport system on a macroscopic scale, the properties of the materials such as the surface structure were not taken into account. In the microscopic viewpoint, thermal transport is described using the concept of heat carriers. [2] Heat carriers are carriers that transport energy, resulting in the change in temperature, for example, photons are the main heat carriers of thermal radiation. [2] Heat carriers can be determined by quantum mechanics with different possible energy states. In a solid, energy transfer can also be described using phonon vibration.

Gas conduction happens when the heat transport is via gas molecules in the surrounding air. Classical treatment of the kinetic theory of gases shows the thermal conductivity of the gas is. [8]

$$k_g = \frac{1}{3} C v l \tag{3}$$

Where k_g represents thermal conductivity of the gas, C is the heat capacity per unit volume, l is the mean free path for intermolecular collision and v is the root mean speed of the molecules. When the tip heats up far away from the sample, thermal energy will disperse into the air and heat up the surrounding gas molecules. The hot air molecules move away and convection occurs. When the tip reaches the sample, the tip-sample distance gets smaller than the mean free path of the air, the air would then transport heat energy directly and act as a conductor [26], [27].

Thermal radiation happens when SThM is operating in both ambient conditions and in vacuum. It is possible to model the far field radiation from a classical point of view using the Stefan-Boltzmann law by assuming the system acts as a black body.

$$\dot{Q}_{rad} = \sigma A({T_{hot}}^4 - {T_{cold}}^4) \tag{4}$$

Where $\dot{Q}_{rad}$ is the power emitted by the black body radiation, T_{hot} and T_{cold} represent the temperature at the heated end and the cold end, A is the emitting area and σ is the Stefan-Boltzmann constant, 5.67×10^{-8} kg s^{-3} K^{-4}. Assuming the emitting area is the end of the tip, A is very small. As there is a direct relationship between A and $\dot{Q}_{rad}$, the power emitted will also be very small due to the geometry of the probe. Wien's displacement law models the peak wavelength of the black body by the following equation.

$$\lambda_{max} = \frac{b}{T} \tag{5}$$

Where λ_{max} is the peak wavelength, T is the absolute temperature and b is the Wien's displacement constant, 2.898×10^{-3} m · K. Assuming the typical room temperature is about 300K, when applying to equation (5), the λ_{max} is approximated to 10 µm. The typical size of a thermal probe is less than 10 µm, therefore the classical theory could not be valid on measuring thermal transport smaller than this scale. The above classical theory shows that near field radiation theory is necessary to model heat loss via radiation. It is experimentally challenging to measure the heat loss due to radiation, this is because the thermal radiation does not play the main role in nano-thermal transport. [8] In an example of the thermal experiment done in vacuum, the main transportation methods are solid-solid conduction and thermal radiation. When the tip is not in contact with the sample, the signal is almost unchanged as the tip was moved further away.

Solid-liquid conduction occurs when the ambient humidity is not zero and a water meniscus forms on the tip due to condensation. The water meniscus increases the contact area between the tip and the sample as illustrated in Figure 2.1 shown earlier. The heat energy takes the path through the water then to the sample. Since the water is acting as a conductor, it is possible to model the thermal energy with Fourier's law. Luo *et al.* [26] suggested a model based on the Kelvin equation. It is possible to eliminate solid-liquid conduction by performing SThM measurements in vacuum.

2.2 Characteristics of a force curve measured by AFM

Material properties such as hardness and roughness of a surface have effects on thermal transfer between a thermal probe and surface. For example, for a given contact force, a softer surface is expected to have a larger contact area with the thermal probe which will contribute to the solid-solid heat transfer. Fortunately, these properties can be studied using force curve measurements provided by AFM. This section will provide a detail analysis for measuring the adhesive force of the sample using the AFM force curves.

In imaging mode, AFM system provides a feedback circuit to maintain a constant contact force between the tip and the sample. In a force curve measurement, which is done on a fixed surface position, the contact force is varied by systematic movement of the AFM piezoelectric towards and away from the sample position. The deflection of the probe cantilever due to this force variation is recorded simultaneously. An analogous thermal curve can also be recorded on this sample position when the AFM records the probe thermal voltage instead of cantilever deflection. Descriptions on thermal curves will be provided in the next section.

A topography scan is required for the SThM to make a force measurement. It should be done on a smooth area of the sample to avoid any impurities that could affect the adhesive force. The smoothness of the sample is analysed by measuring the local roughness. A point on the surface will then be selected by the user to take the force curve measurement. Usually several points will be selected. The importance of roughness for thermal measurements will be discussed later.

In a force curve measurement, the tip will first be retracted vertically away from the surface to a selected start position shown in Figure 2.2. The laser position on the photodiode reflected from this interaction-free cantilever at rest is taken as the reference voltage, V_0. The AFM piezoelectric will then start moving the tip towards the surface (known as tip approach) until a

contact is made. This position is labelled as 'contact point' position in Fig. 2.2. At this position, the adhesive and capillary forces of the surface prematurely pull the tip towards the surface and cause the cantilever to bend. The bending causes the laser reflected from the cantilever to move to a position different from V_0. The tip would carry on pressing into the sample which makes the cantilever bends further in the opposite direction until a pre-set displacement range is reached.

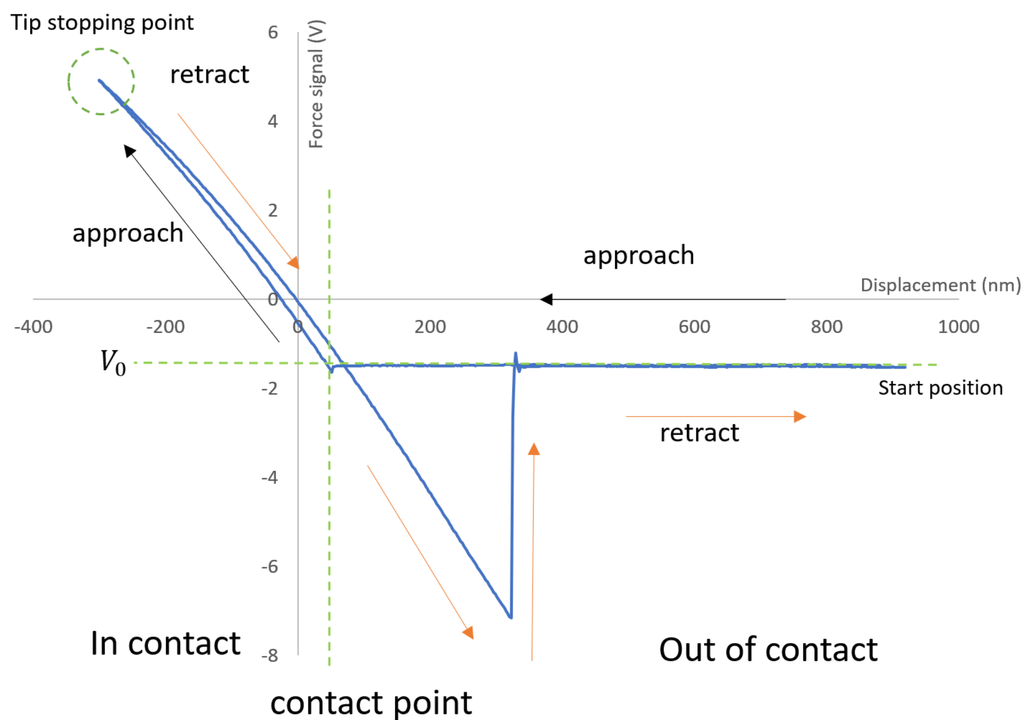

Figure 2.2. A typical force measurement diagram of SiC sample and operated in air. The diagram describes the probe position at each point from the starting position where the probe starts recording the data, approaching to contact point where the probe makes contact with the sample surface. The tip keeps pressing on until the tip stop at the pre-set displacement range labelled as tip stopping point. The tip will then retract from the surface, the surface adhesive force is keeping the tip on the surface and bending the cantilever, a hysteresis is formed during the tip is retracting. When the tip gained enough force that overcomes the surface force, the tip will snap out and retract to the starting position.

After the tip stopped, the piezoelectric will move in the opposite direction and the probe starts its retraction from the surface. It is noted that the deflection path of retraction does not exactly follow the approach path. The reason is the voltage and displacement of the piezoelectric are nonlinearly related. [28] This results a curved path of deflection, which would affect the

sensitivity measurement shows in figure 2.3. When the tip reaches the contact point again, the adhesive force from the sample keeps the tip in contact with the surface, i.e. the tip "sticks" on the surface. This causes the cantilever to bend until it reaches a point where there is enough force to overcome the adhesive force. The tip will then snap out of the surface and returns to the reference point at V_0.

In the retract direction, the extra adhesive force provided by the cantilever-tip interaction causes a hysteresis, this extra force in retraction is where the adhesive force is measured. The point taken for this force is the difference between minimum point before snapping out and at V_0.

The figure 2.2 shows the force curve with a single layer of bulk material, the force curve is expected to be different when there is an extra surface layer on the surface for example water or oxidized material.

The AFM system collects the force signals in voltage. Therefore, the raw signal needs to be converted to force in Newton units. In order to convert this voltage into a force in nano-Newtons, the spring constant of the probe needs to be known. The conversion can then be done using Hooke's Law as follows:

$$F = \kappa\alpha(V - V_0) \qquad (6)$$

$$\alpha = \frac{|d_2| - |d_1|}{V_2 - V_1} \qquad (7)$$

Where F is the force measured in nN, κ is the spring constant of the cantilever, measured in N/m. V is the potential measured at each point on the force-displacement curve, V_0 is the reference potential, both the potentials are measured in volt. α is the optical lever sensitivity, which is a measure of the change in displacement d divided by the change in potential V during retraction. This is represented in equation (7), where d_1, d_2 are the distance of the vertical

direction of the tip moving, measured in nanometres, and V_1, V_2 are the electrical potential that is recorded in AFM, measured in V. Figure 2.3 illustrates where the measurements should be taken on a generic force curve.

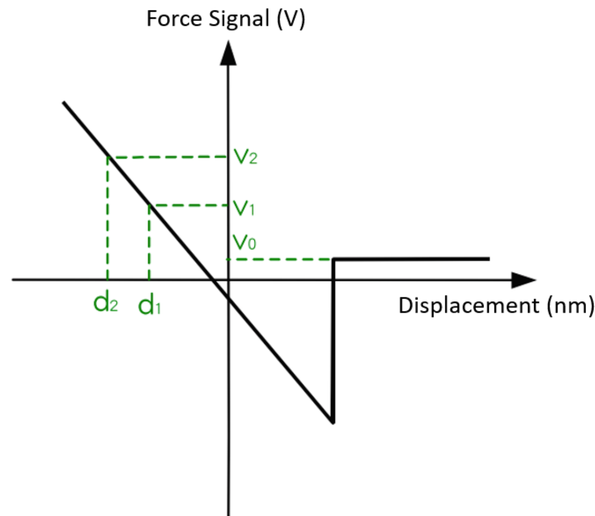

Figure2.3. Schematic diagram of force displacement curve. V_0 is the reference voltage when the tip is away from the surface and the sample is exerting no force on it. The optical lever sensitivity α is measured at the retract regime, note that the sensitivity is the inverse of the gradient at the retract curve. [29]

Recalling the figure 2.2, the deflection path during retraction has shown to be a curve due to the nonlinear piezoelectric, which is different from figure 2.3. The measurements described in figure 2.3 should use the linear range of the retract deflection when analysing the sensitivity. There are a few methods for cantilever spring constant measurement. The most common way to measure the spring constant is the dimensional method. This method is developed using the material properties combined with Hooke's Law, assuming the cantilever to be rectangular.

$$F = -\kappa x \tag{8}$$

$$E = \frac{Fx_0}{A_0 x} \tag{9}$$

In the spring case, the Hooke's Law in equation (8) is used to describe the relationship of spring constant and the force, where F is the applied force, κ is the spring constant, x is the displacement of a spring. Equation (9) shows the method for obtaining Young's modulus, E.

A_0 is the cross-sectional area of the spring and x_0 is the original length of the spring. The cantilever spring constant was reported by Poggi *et al.* [30] using the following equation.

$$\kappa = \frac{Ewt^3}{4L^3} \quad (10)$$

The notations for equation (10) are the same as in equation (8) - (9), where κ is the spring constant, E is the Young's modulus, w is the width of the cantilever, t is the thickness and L is the length of the cantilever.

In 1993, Cleveland [31] proposed a method of measuring the spring constant of the AFM cantilever by adding a known mass at the end of cantilever. The principle relies on measuring the natural frequency of the cantilever before and after adding the known mass, from the difference of the frequency to obtain the spring constant. As the natural frequency measurement is independent of the shape of the probe, this method can measure the spring constant with a more complex cantilever design.

However, as the probe structures are getting more complex with more than one material involved, it is difficult to measure the Young's modulus. Sader *et al*. [32] published a method to measure the spring constant with an arbitrary shaped probe based on his previous method, which opened up more possibilities for probe designs and choice of materials. The Sader method is based on Cleveland method, but instead of adding a physical known mass to the cantilever, Sader measured the resonance frequency of the AFM cantilever in air and in vacuum. This method has an advantage that it is not restricted to shape or the material of the cantilever.

$$\kappa = M_e \rho_c twL\omega_{vac}^2 \quad (11)$$

Where κ is the spring constant, ω_{vac} is the fundamental radial resonant frequency of the cantilever in vacuum; t, w and L are thickness, width and length of the cantilever respectively,

$\rho_c$is the density of cantilever and M_e is the normalized effective mass. The advantage of this method is that the shape of the cantilever is not restricted, this is because the spring constant is heavily relying on the quality factor when measuring resonant frequency in vacuum. However, this method requires the density of the cantilever, as the structure of SThM tip becomes more complicated with more materials, it is challenging to estimate the density of the cantilever.

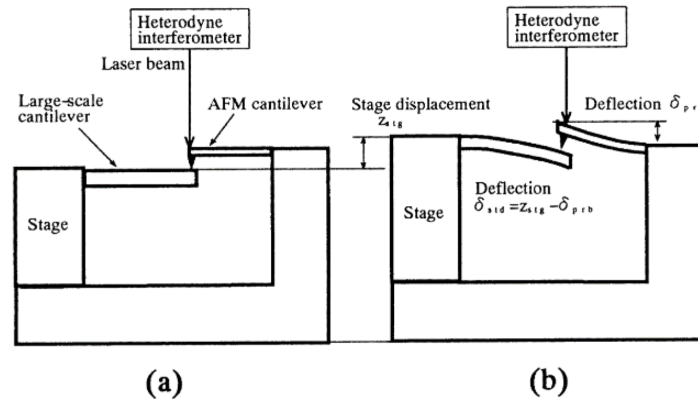

Figure 2.4 A schematic diagram demonstrating the reference cantilever method using a large-scale cantilever against the AFM cantilever. a) The AFM cantilever is pressed on a large-scale cantilever that has known property. b) When a force is applied by the AFM cantilever, both cantilevers will bend as different rate, since both cantilevers are exerting the same force, the spring constant is measured by the deflection of the cantilever. [33]

The referencing cantilever method is a more recently developed method, the principle is uses a larger scale cantilever with known spring constant to calibrate the spring constant. Figure 2.4 demonstrates the reference cantilever method. The AFM probe is pressed against a larger scale cantilever, both cantilever would then bend at different rates. Since the force applied to each other are balanced, with the known large-scale cantilever spring constant, we can then work out the spring constant using Hooke's law. [33]

The dimensional method to estimate the spring constant will be used in this project. The reason is due to the simplicity of the procedure as this project is aiming to develop a method for exploring the thermal properties of the material. For this project, a scanning electron microscope will be used for measuring the dimension of the probe.

2.3 Characteristic of a thermal measurement and thermal calibration

In section 2.2, the cantilever bending was described along with the force measurement. The thermal curve follows a similar principle; however, the input channel is used to measure the voltage corresponding to the temperature. Figure 2.5 shows a generic thermal measurement measured in air.

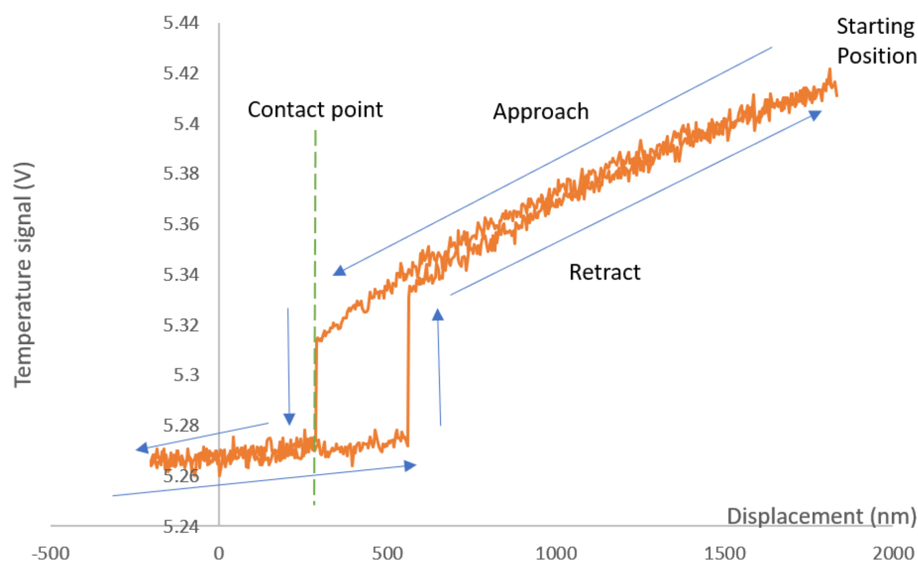

Figure 2.5 A schematic thermal measurement of SiC in air using a fabricated resistor probe in active mode. The arrows indicate the motion and position of the probe throughout the measurement. The position at which the probe snaps into the surface is marked as the contact point.

The tip is first retracted from the sample surface to the pre-set displacement position, labelled starting position in figure 2.5, and then starts to approach the surface. The temperature will start dropping due to air conduction increasing as the tip-sample distance gets smaller. When the tip gets closer to the sample surface, the tip snaps into the sample surface at the contact point, this is the same as described in the force measurements. The temperature signal will have a sudden sharp drop, this is because the solid-solid conduction and solid-liquid conduction happens and there is suddenly more heat flowing through the interface.

The tip will then continue pressing into the surface as the z-motion continues. The sample surface will deform if the sample is soft or the tip will deform if the sampler is harder than the

tip. If either of these happen, then this will increase the contact area between the probe and the sample surface and increase the amount of solid-solid conduction therefore cooling the probe further. The tip will stop at the pre-set displacement and start retracting from the surface. When the cantilever retracts, from the force measurements we know that the tip will remain in contact until the cantilever has enough force to overcome the adhesive force, the tip temperature remains largely the same during this process. Then when the tip snaps out, the temperature of the probe increases back to the temperature before it approached.

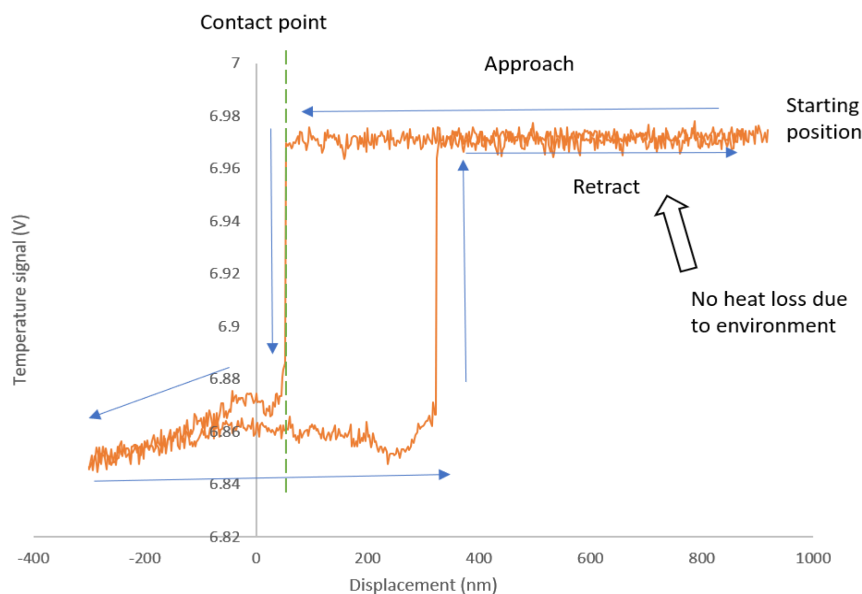

Figure 2.6 A typical thermal result of SiC measured in vacuum operated in active mode. The main characteristic is there is no heat loss before the tip reaches the contact point.

Figure 2.6 shows a thermal curve measured in vacuum. Here, the temperature at the starting position is similar to the temperature at the contact point, until the tip snaps into the sample, unlike in figure 2.5 where there is a temperature drop from the starting position to the contact point. This is because in vacuum the air conduction and solid-liquid effects are eliminated, there were no air or water molecules disposing heat from the tip. [13] The thermal transport paths in vacuum have reduced to only solid-solid conduction and thermal radiation, the temperature drop in vacuum will be reduced by this smaller contact area with no meniscus.

The force measurement is also used in verifying where the temperature drops. When putting the force curve and the thermal curve together, the intersection of the curves shows the geometric point where the probe is in contact and out of contact with the sample. This is shown in Figure 2.7.

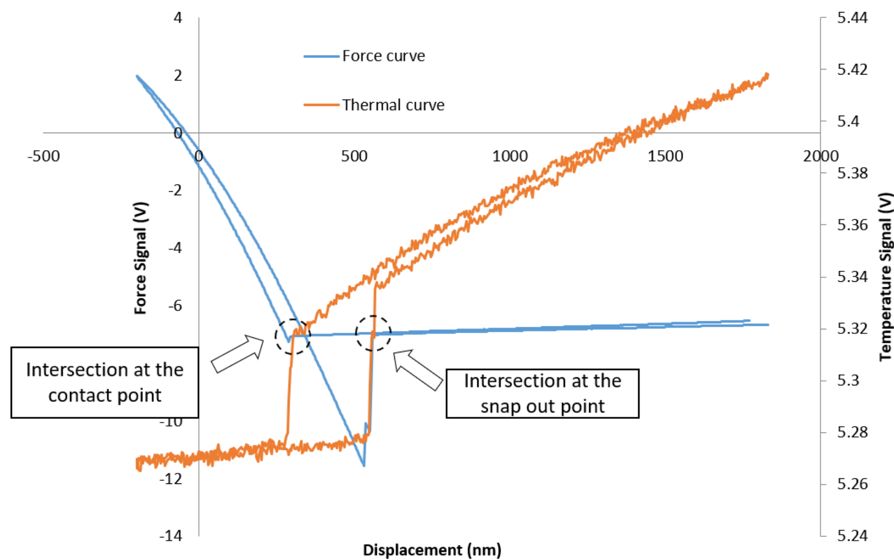

Figure 2.7 A force curve and a thermal curve to verify the interpretation of the thermal curve. The intersection of both curves at the contact point and the snap out point are used to verify the temperature change on the thermal curve.

Figure 2.7 shows the direct comparison of both force and thermal curves placed on the same axis. Recalling the figures 2.2 and 2.5, the probe position at each point was described individually from the force and thermal result. However, both force and thermal measurements are measured through the same instrument at the same point, the probe movement should be identical between figure 2.2 and figure 2.5.

The change in temperature would require a conversion for the voltage signal back into °C for comparison. The calibration process involves heating up the tip with a heater to a known temperature. When the tip reaches the preset temperature, the heater is turned off and the tip left to cool naturally. This results in a graph of temperature against time for the heater and a

graph of voltage against time for the tip. Figure 2.8 demonstrates the temperature recorded for the Peltier heater and the probe.

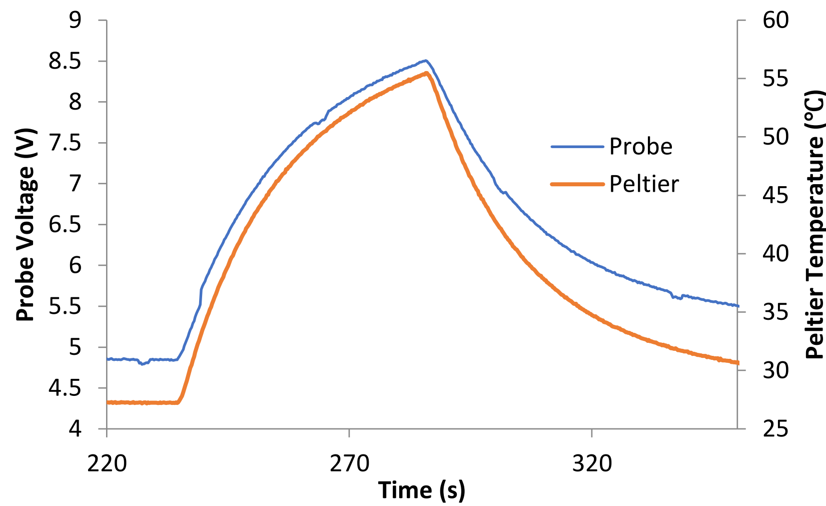

Figure 2.8 The typical shape for the thermal calibration in air. The calibration curve includes the Peltier temperature and the probe voltage both plotted against time.

Although in chapter 2.1 the different heat transport mechanisms were described, for the calibration, the tip and the heater are in contact during heating. After a certain amount of time the tip and the heater are in thermal equilibrium. The temperature of the heater should therefore be proportional to the total temperature detected by the tip. This is shown in equations (12) - (13)

$$T_{peltier} \propto V_{tip} \tag{12}$$

$$T_{peltier} = B\, V_{tip} \tag{13}$$

The $T_{peltier}$ is the temperature of Peltier, V_{tip} is the recorded voltage of the tip, B is the conversion factor for converting temperature and the voltage. The conversion should use the values that were recorded when the probe is cooling. The conversion coefficient B would be obtained by first plotting the temperature of the Peltier against the voltage of the tip, then the line of best fit of the graph represents the conversion coefficient B.

The conversion could only provide the change in temperature in ℃, it does not give the information for the absolute temperature of the thermal map. The reason is the detection circuit is a balanced bridge circuit, making knowing the actual voltage difficult.

Chapter 3 Experimental method

This chapter is separated into two parts. Part I starts with describing the SThM instrument and how the AFM is modified into an SThM. Then the selection of the samples will be discussed. Part II describes the procedures of the experiment, it will start with the preparation of the sample, the tip and the SThM; then move onto the procedure of force measurements and thermal measurements.

Part I: Instrumentation and the preparation

3.1 SThM instrumentation and integration to AFM.

In chapter 1 the principles of AFM and SThM were described, the fabricated resistor probes require a power supply and a voltage detector for monitoring the temperature changes. The AFM probe holder needs to be modified to provide electrical contacts for the current to pass through. The sample holder needs to be modified to provide the ability to heat up the sample for the calibration of the probe or SThM operating in passive mode. The SThM instrument at the University of York is used in this thesis, the modifications to the AFM are shown in Figure 3.1.

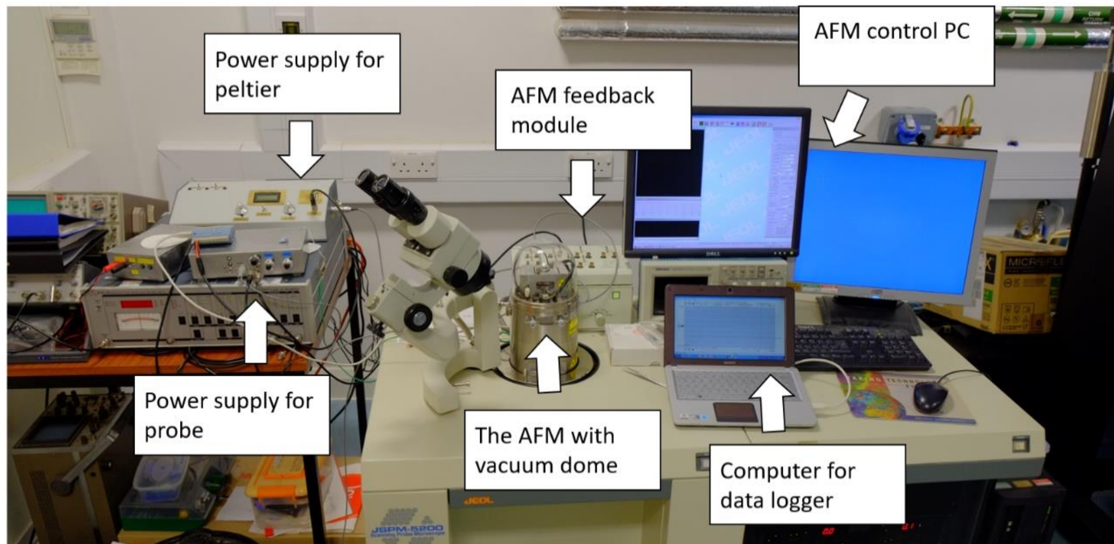

Figure 3.1 A photograph of SThM set up at the University of York. Including the data logger, probe power supply, Peltier power supply and detection circuit, the vacuum facility and the AFM. The AFM control PC is the main control for the AFM.

The AFM used in this project is a JEOL 5200 atomic force microscope, the vacuum facility is from the original AFM which has not been modified. The vacuum dome is used for providing high vacuum environment by connecting to a pump. The probe power supply is designed to have a small current to protect the probe. The AFM sample holder is modified to have a Peltier heater, a device making use of the Peltier effect to generate heating or cooling at the electrical junction. The power supply for the Peltier controls the temperature heating of the sample holder. The Peltier power supply is connected to a 4-pin connector to the sample specimen inside the AFM. The reading on the Peltier power supply is used for thermal calibration to convert voltage into temperature. The feedback AFM module is used to switch between the thermal and force feedback, the data logger computer is used to monitor the probe current. The detail of calibration process will be discussed later in this chapter.

The thermal probe holder was specially designed and produced by Mr John Emery in the Electronics Workshop at the University of York. The comparison between the thermal probe holder and the contact probe holder is shown in Figure 3.2.

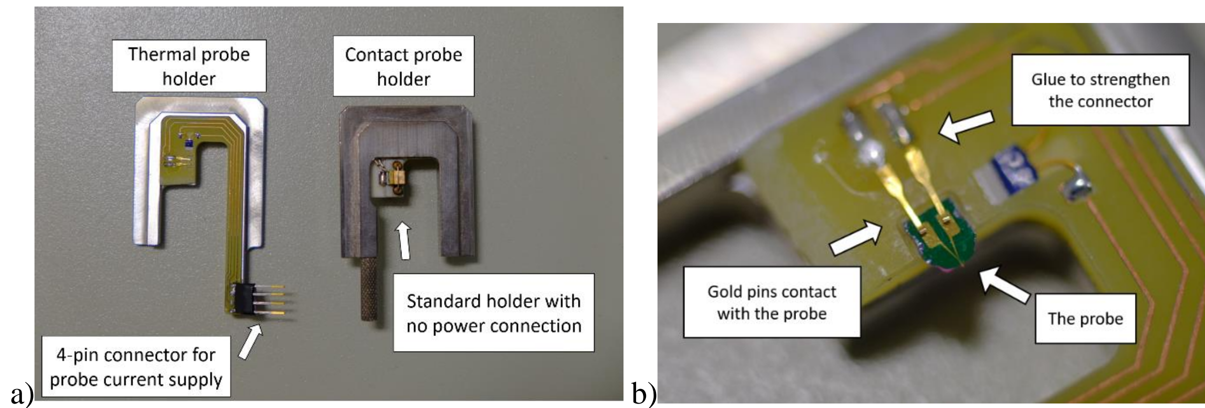

Figure 3.2 a) A comparison between the thermal probe holder (left) and the contact probe holder (right). b) A photograph of the thermal probe connector with a thermal probe attached.

From figure 3.2a, the design of the thermal probe holder is based on the shape of the contact probe holder, this is to ensure it fits in the JEOL AFM. On the holder, there is a printed circuit board with a 4-pin connector to power the probe and a Peltier heater, this is shown in figure 3.2b as well as the two thin gold pins that connect the probe with the power supply. The design was improved later by having glue placed at the gold pins to increase the strength, the glue position is labelled in figure 3.2b). Since the data for this project has collected with the new design, the effect of the probe holder design to the measurements could not be measured.

The power supply for the probe is connected via the thermal probe holder, the probe voltage signal is connected to the data logger and to the feedback module for recording the change in probe temperature. The power supply/detection circuit is a balanced bridge circuit, designed by Prof. Weaver from the University of Glasgow [32]. The circuit is designed to prevent the probe breaking as well as increasing the signal to noise ratio.

There are several causes that might break the probe, for example static electricity from the skin or any small shock from inside the circuit. The reason for this is the thermal junction of the

probe is small, when there is a high voltage applied across the resistor, the heat generated due to Joule heating would melt the resistor and break the circuit. Before the experiment, the detection circuit of the probe has to be balanced by the power supply fine adjustment, so that the change in voltage due to temperature are more easily measured. The circuit diagram is shown in figure 3.3.

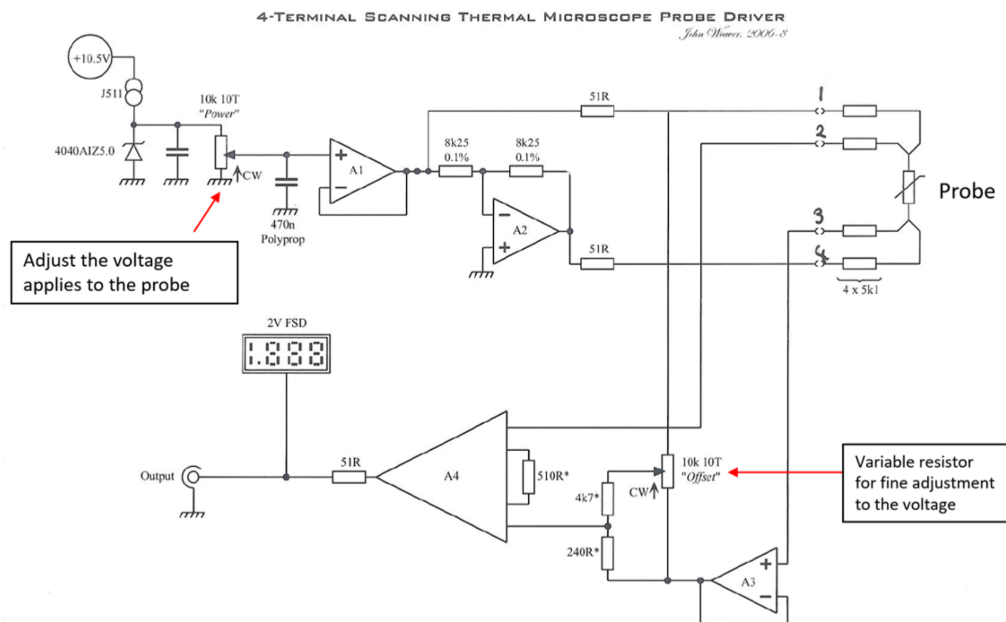

Figure 3.3 A circuit diagram of the power supply of the probe. The probe is represented as a variable resistor as each probe will have a variation in resistance. The arrow showed the two variable resistors that controls the main voltage applying to the tip and the fine adjustment to the voltage, labelled in the diagram. [34]

The power supplies for both Peltier specimen heater and the probe were connected to a data logger that is connected to a separate laptop. The reason is a separate computer system could reduce the noise picked up from the AFM system. The detection signal for the probe would also feed into the AFM feedback circuit. This is because the AFM has the ability to record the change in temperature while measuring the topography. The connection for this setup is showed in Figure 3.4.

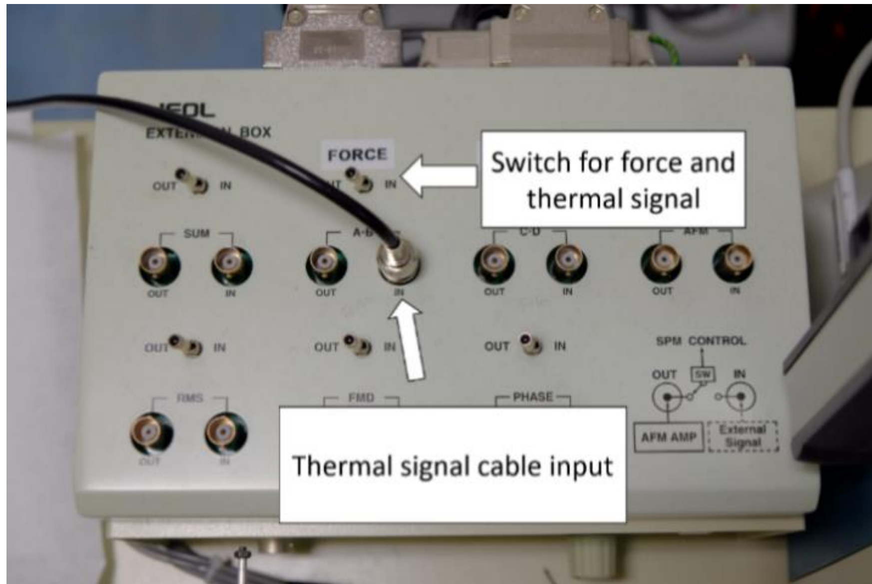

Figure 3.4 The AFM feedback module panel showing the cable connection and the switch for feeding the thermal signal into the AFM.

The probe voltage signal was connected to the force channel. It controls whether the AFM was making measurements in normal AFM mode or in thermal mode. The force and thermal signal is controlled by the switch indicated in figure 3.4. The switch enables the thermal signal to be fed into the AFM for measuring the topography along with the thermal signal.

3.2 Sample selection.

The choice of samples was decided to cover a wide range of thermal conductivity and mechanical properties. In the force measurement, it is particularly important to have different material hardness. It is also interesting to study the effects of roughness and hydrophobicity.

The materials were sourced internally through different research groups at the University of York Physics department, the properties varied from different methods of manufacturing and different structure of the material. The table 3.1 displays the typical values of the samples, the actual values vary from the manufacturing of the materials. If any calculations are required, measurements should be made for the specific sample.

Material	**Thermal Conductivity (W/m·K)**	**Hardness (Mohs)**	**Elasticity Modulus (GPa)**
Doped 6H Silicon Carbide (0001)	420.00	9	302
Gold (bulk)	314.00	2.5	79
Silicon	124.00	7	179
Mica	0.53	2.5	170
PTFE	0.20	N/A	0.4

Table 3.1 A table summarising the properties of the materials chosen for this thesis. The table includes the thermal conductivity, hardness and the elastic modulus of the samples. [35], [36], [37], [38]

Teflon (PTFE) has the softest surface and the lowest thermal conductivity. The softness makes it challenging for making measurements for both topography and temperature. As the surface is soft, the deformation of the surface is expected from the tip. Mica is a good material for AFM and SThM due to its layered structure and smooth surface. It has low thermal conductivity and a relatively hard surface, this covers the lower range of thermal conductivity.

Silicon is a substrate with a 300nm silicon oxide layer, the thin film gold sample used in this project is fabricated on the silicon sample. [39] Silicon is a semiconductor with a hard surface and high thermal conductivity. The hardness of the surface makes it more difficult to deform,

therefore the temperature changes would be less dependent on the increase of contact area in contact.

Silicon carbide is the hardest material from the set. It has the highest thermal conductivity to cover the 400 W/m·K range. It is used in calibrating the sensitivity of the cantilever. The hardest surface would cause least deformation for thermal measurements. However, it could potentially damage the probe as the Pd coating is soft.

Thin film gold is the sample for testing the technique, it is a thin film conductor fabricated on silicon. The thin film of gold is 150nm thick grown on a silicon substrate and patterned by e-beam lithography. Between the gold and silicon, there is 8nm thick layer of chromium at the interface to improve the adhesion of gold on the silicon. The sample was grown by Dr Vick at the University of York and patterned at the University of Leeds. [39] The measurements for this project will be using the electrical contact pads around the outside, which is an area that does not have dedicated fabrication pattern.

The challenge is to find the thermal conductivity of this sample, as it is not a bulk material, the conventional gold thermal conductivity will not be valid. The thin film gold is expected to have a harder surface than PTFE, this is because metal should be harder than polymers. However, because the gold is a thin film sample, the surface hardness and thermal conductivity are also expected to be different from the bulk materials.

Part II: Experimental procedures

3.3 Preparation for the force and thermal measurements

The Scanning Electron Microscope (SEM) is used in this project to serve two purposes, the first is to measure the dimension of the probe for calculating the spring constant, second is to verify the tip status. Figures 3.4 shows the result from a typical SEM experiment of a thermal probe.

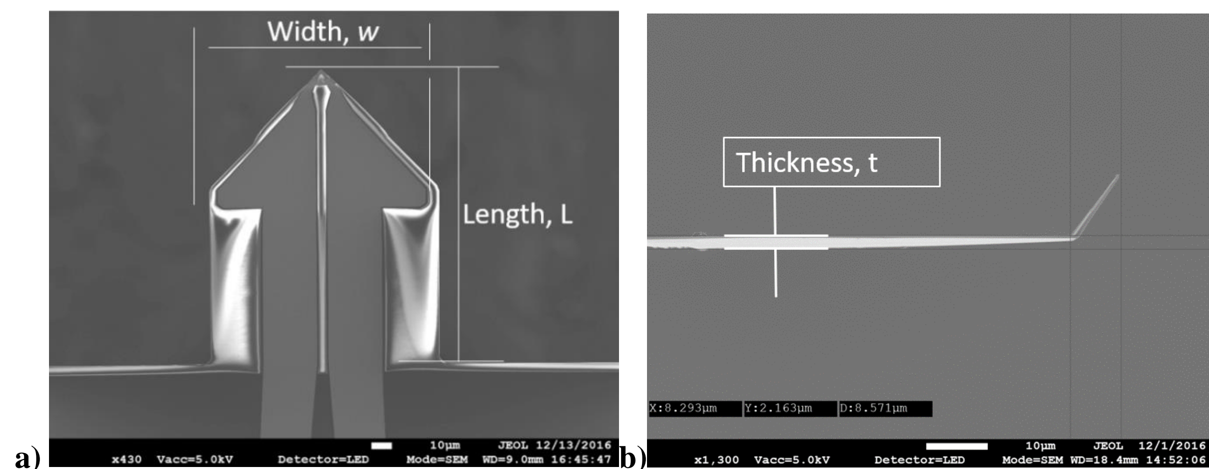

Figure 3.5 An SEM image illustrating a) the width and the length measurements from top view, b) thickness measurements from the side view.

The dimensions of the probe required for the spring constant calculation is described in equation (9), where the width, length and thickness measurements are required, as shown in Figure 3.5a and b). Different specimen holders were required to measure each of the dimensions where a flat specimen holder was used for measuring the width and length of the probe and an angled specimen holder was used for measuring the thickness.

The dimensions were obtained by measuring directly using the SEM software. The SEM provides a low instrumental error when measuring the dimensions. However, the shape of the probe is not ideally uniform, for example, the thickness of the cantilever at the tip end is usually thinner than the mounting end and the shape of the cantilever is not perfectly rectangular. When

estimating the spring constant with the dimensional method, the thickness and the length contribute most in equation (10) because of the power factor.

The cantilever spring constant was calculated using the values estimated from the SEM for each probe. The thermal probe cantilevers were assumed to be made of pure silicon nitride and the contact probe made of silicon. The Young's modulus of silicon nitride and silicon were looked up [36] and the values for calculation was taken at the midpoint of the range given. The error of Young's modulus is determined by this range. The cantilever is combined with other substances for instance the gold connection pad and the Pd resistor, however the effect on the Young modulus is negligible. The total error was worked out for each variable in equation (9) with multiplication and addition of the quantity, the error will be presented as a percentage error.

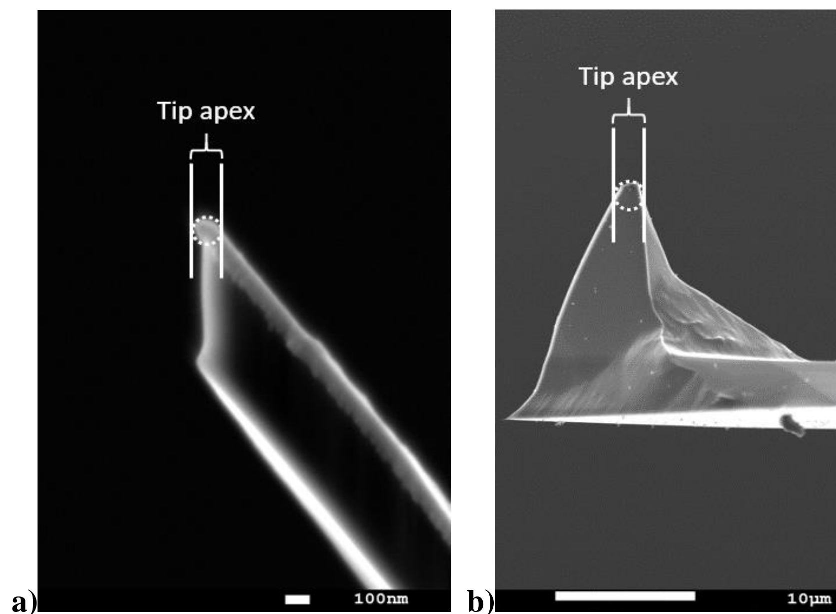

Figure 3.6 The estimation of the tip apex of a) the thermal probe and b) the contact probe.

The tip apex radius is estimated while measuring the thickness of the tip, this is illustrated in figure 3.6. The purpose for this is to compare the tip size between the contact and thermal probe, in order to compare the quality for the topography and roughness for the samples. The thermal

probes were too fragile to be cleaned and should be kept and operated carefully under a clean environment. The SEM was also used to verify the condition of the tips before a measurement.

The samples were small enough to fit on the AFM Peltier holder, typically the size is about 3mm on the side for a squared shape sample. The samples were first cleaned by placing in isopropanol inside an ultrasonic bath for 10 minutes, then dried with an air blower. This procedure was performed every time before any measurements were taken, this is to ensure there were no obstacles on the sample surface. The mica sample did not require any ultrasonic bath, this is because mica had a layered structure and can be cleaned, the cleaving process for mica was simply to peel off the top layer with tape.

The samples had different thickness and the layout for the samples on the sample holder required careful planning. When the AFM was measuring the thinner samples, the thicker samples needed not to obstruct the cantilever. This configuration of the samples is shown in Figure 3.7.

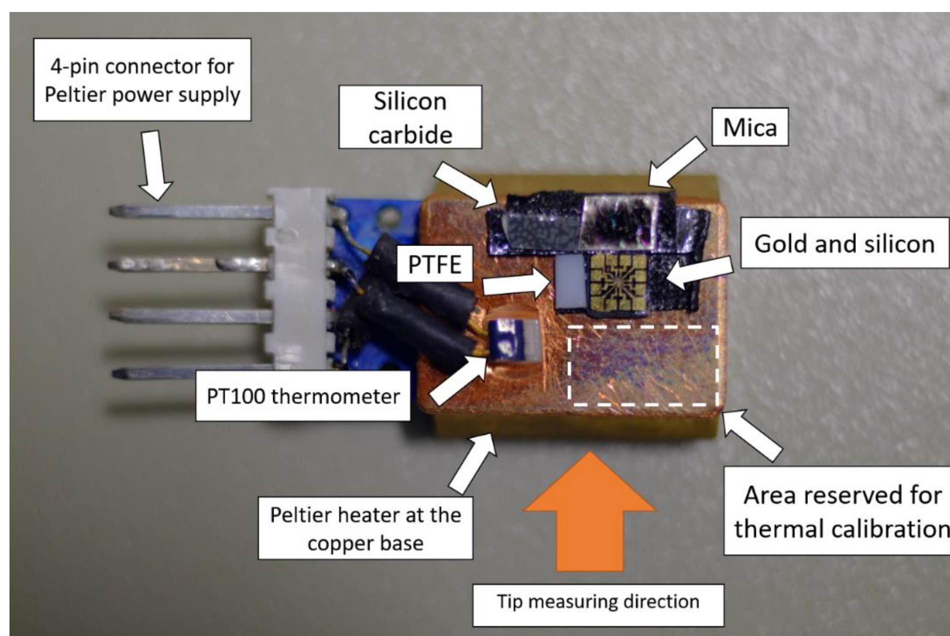

Figure 3.7 The figure of the sample arrangement on the heater.

The tip measuring direction labelled in Figure 3.7 indicates the direction of the tip after the sample specimen was inserted inside the SThM. The PTFE and gold on silicon samples were

thicker than silicon carbide and mica, in principle the thicker samples should be further away for scanning to prevent obstruction when scanning. In the earlier stage of the experiment, the samples were placed on the original AFM specimen holder with no Peltier heater integrated. It was then discovered that the AFM could not scan the thinner samples surfaces. The reason for that is the probe holder was modified for the thermal probe, which offsets the z direction limit.

The silicon carbide and mica were then lifted up by placing a silicon bar underneath. With the silicon bar in place, both samples were thicker than PTFE and gold on silicon, hence the arrangement in figure 3.7. At the later stage of the experiment, the AFM specimen holder was modified to have a Peltier heater integrated for the ability to do thermal calibration in vacuum, but the layout of the samples was kept. The samples were shifted to one side of the specimen holder, the purpose for this was to leave an area for performing thermal calibration with the probe. The calibration procedure will be discussed later in this chapter. The sample specimen would then be inserted into the AFM and connected to the power supply.

3.4 Methods of topography measurements

The electrical resistance of the thermal tip should be measured before and after inserting into the probe holder. Although the SEM image of the tip should verify whether the tip is damaged or having any impurities, the electronic connection is verified by the resistance measurements. The power supply box was connected to the probe holder while inserting it into the AFM. The power supply for the probe is a balanced circuit; the procedure for balancing the circuit is to apply a small current less than 0.1mA, when the voltage of the probe is increased as shown on the data logger, the voltage is then set back to near 0V by adjusting the offset dial on the power box. After the power box is balanced, then the current was slowly increased to 0.6mA and 0.8mA. The current was chosen to improve the signal to noise ratio while preventing damage to the tip. The reason for slowly increasing the current is to avoid the sudden electrical shock that can damage the resistor at the tip. The data logger monitored the voltage in case of overheating and circuit damaging. The instrumental error is 0.05mA since the current reading relies on the precision of the engraving on the knob, the only error estimation is half of the smallest division on the knob. The error is more significant when comparing the thermal results.

The laser adjustment was done once there was a current passing through the probe. This is because when a current passed through the probe, the Joule heating would bend the cantilever and the laser spot will need re-adjustment, hence the probe current balancing was done before the laser adjustment. The laser spot was set to reflect from near the edge of the probe, the laser signal represents the cantilever deflection caused by the sample surface structure, therefore having the laser spot closer to the tip provides a more accurate topographic image. The photodiode also required adjustment for the largest signal of the probe, for thermal probe, the typical signal is about 3V and the signal for contact probe is larger. The reason is that the contact probes have a larger reflective surface than the thermal probes and hence the more laser beam is reflected.

The laser signal could be different every time performing the experiment even if the same probe is used each time. This is because when the probe is inserted to the holder, the positioning of the probe will be different each time and the laser will not be reflected at the same area of the tip and hence the variation in the laser signal. The laser signal is adjusted to collect as a high voltage as possible to improve the signal to noise ratio. If it is at lower voltage signal, the signal-noise ratio for the cantilever deflection will be lower and reduce the precision of the force measurements. Note that there is a significant amount of laser signal heating observed during the setup of the tip. This could contribute to the temperature difference during the experiment, which should be taken into account as a possible source of error if the laser position moves during the experiment.

For experiments performed in vacuum, the vacuum dome should be placed after the laser adjustment and be pumped down overnight. The vacuum is pumped overnight so that the pump and the pressure is stable before performing any measurements. During the pump down, the laser and the probe power were advised to be off after the laser adjustment. The laser could not be adjusted after the vacuum dome is placed, therefore it should be done in advance. The vacuum should reach 10^{-4} to 10^{-5}mbar after one night. The specimen was then manually approached so that it was close to the probe. The process is observed by an optical microscope and it is important that the sample does not hit the probe. The approach process is then continued using the JEOL WinSPM software to control the z-piezo tube for the remaining distance. During the experiment, the laser spot could move on the photodiode. A magnet is attached on the control knob of the photodiode, the knob could be turned by using this magnet, while the whole instrument is inside the vacuum dome.

The vacuum is created by placing the vacuum dome on top of the SThM for pumping down. When preparing the vacuum dome, vacuum grease is used for sealing the gap between the dome and the SThM, the quality of vacuum grease could directly affect whether the vacuum is

sealed entirely. The vacuum pressure was left overnight for stabilisation, however the vacuum pressure should be monitored during the experiment. The reason is the vacuum reduced the heat path for cooling the tip. A change in pressure was observed from 10^{-5}mbar to 10^{-4}mbar and this change did not cause a significant effect on the thermal result.

The quality of the topography was determined by the scan size and the clock rate, while the filter setting was set at 50kHz by default for both force and thermal measurements. The scan size is the dimension of one side of a square and the clock rate is the speed for the probe moving across the area. [29]

The topography scan was chosen to a scan size of 500nm for roughness analysis. The scan size of the topography should be enough to present the overall sample surface while retaining spatial resolution for making thermal measurements. The clock time should be optimised for a balance between scanning time and quality. A slow clock rate can result in a scanning duration of 30 minutes per topography scan. In this project, the scanning duration is optimised to approximately 10 minutes per scan. The probe requires a minimum time window to respond to the surface. Such minimum requirement can be found by scanning the sample surface at different rate and thus determine at which the quality of the scan does not improve significantly further by inspection.

The thermal probe was expected to have a larger contact area than the contact probe, the scanning size and the clock rate were optimized for both probes to have the same setting for comparison. The scanning size and the clock rate in this project was optimised to 500μm with 500μs scanning time for both contact probe and thermal probe. Thermal measurements were measured by enabling the probe power signal input to the AFM feedback hub.

After setting up WinSPM, the scan was commenced to collect the topography. In addition, after each scan, the laser signal must be checked. Particularly after scanning on a hard sample with

a soft tip, it is possible to cause deformation to the tip after a scan therefore a check on laser signal would ensure the result is representative. The topography image often required processing before analysing. This is to improve the contrast of the image to enhance the details on the topography. The appropriate height scale should be chosen to extract enough detail for roughness analysis.

3.5 Force measurement and roughness procedure.

The force measurements were used to measure the adhesive force of the sample. The roughness of the sample surface would affect the measurements, therefore when performing the force measurements, a clean smooth area of the topography should be chosen. The displacement for the specimen is the distance range for how far away the stage should move and the clock rate determines the approaching velocity of the sample. These variables needed to be set in the WinSPM software before measuring the surface force. The displacement value was done by trials and errors because it was different for each sample. The optimum displacement should show a continuous curve with the following elements: the starting position, the snap in point and the snap out point, which were indicated in figure 2.2. The author started by moving the tip away from the sample for 1000 nm, then decreasing the distance by 100nm to get the optimum displacement. The clock rate was set to 1ms.

In section 3.3, the spring constant of the cantilever was calculated from the SEM measurements. The force conversion that was described in equation (6) requires the measurements of sensitivity, α, as defined in equation (7). The sensitivity measures the displacement per deflection signal. If the sample surface deforms when the tip is in contact, it would misrepresent the deflection signal of the cantilever. The sensitivity is chosen to measure from the force curve of silicon carbide and then apply the same sensitivity to all other samples. Silicon carbide has the highest surface hardness from the sample set that gives the least surface deformation.

The sensitivity was taken as the line of best fit of the retract section on the force curve in the linear range of data as shown in figure 3.8. The reason is due to the nonlinear piezoelectric as shown in figure 2.2. The measurements were repeated at all points take for each area and the standard deviation used as an error.

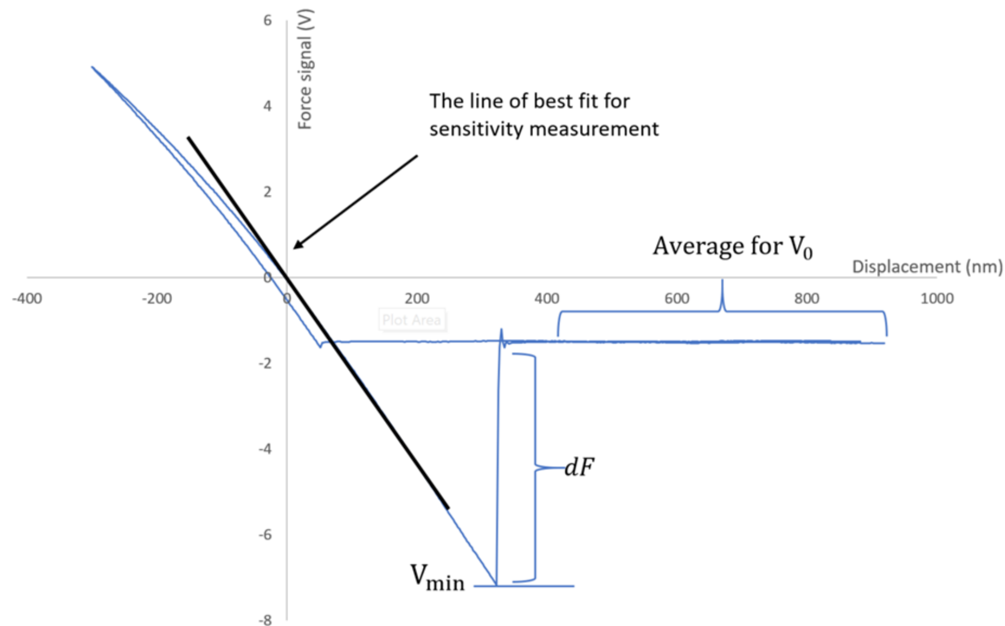

Figure 3.8 A schematic diagram showing the measurements made in a force curve. The difference of V_{min} and V_0 is the adhesive force dF being measured. The line of best fit for sensitivity measurements is noted.

The V_0 from equation (6) was measured individually for each sample and each curve. The V_0 was measured by averaging the V at the retract region after the zero point, this is shown in figure 3.8. The region is chosen to avoid the vibration caused by the snap out of the cantilever. Each force curve was converted individually as the V_0 could be different each time. The adhesive force measurements were made by measuring the force of the cantilever when the tip snapped out during retraction. The force measurement, dF, was taken as the difference between the minimum point, V_{min}, and the reference potential, V_0, after the force curve is converted into Newton units. The principle is the same as shown in figure 3.8.

The force curves were repeated at 3 different areas for each sample. Each area was repeated 3 times and averaged for presentation. All 3 areas were compared and found to be the same therefore the author was able to average the total 9 points of measurements for reducing the random error. When the areas are different, the areas were not averaged and this will be noted. The force measurements are localised measurements, when repeating the experiment, different parts of the sample surface were chosen to give a fuller representation. For each sample, the dF at each area was averaged and the error is worked out through the standard deviation. Then the dF of the sample was obtained by averaging the dF from the three areas. The total error for the force would be weighted from the errors measured in each area. When comparing the adhesive force, the error caused by the spring constant was not counted, this is because the measurements for each sample were performed with the same tip. The spring constant error should be accounted for when comparing the results using different tips, and the adhesive force should be normalized accordingly. There are other factors that would affect the adhesive force measurements. The topography was analyzed before picking the areas for force measurements to make sure the areas were representative of the surface structure.

3.6 Calibration of thermal probe and measurements procedure

As noted in Chapter 3.3, the purpose for thermal calibration is to measure the thermal sensitivity of the probe, converting voltage to ℃ for analysis. This is because the probes are not identical and their electrical resistance varies. This resistance variation causes the difference in thermal sensitivity, therefore the calibration process is required for each new probe used. The probe resistance was measured by the multimeter before it was inserted into the probe holder.

The calibration coefficient is measured before starting the force and thermal experiments. When there is a change of probe, it will require another calibration because each probe will have different thermal sensitivity. In addition, the tip is observed to have a change of the sensor shape, therefore when the tip has been used for many experiments, the calibration should be remeasured. A Peltier heater was used for the thermal calibration with a Pt100 thermometer for monitoring the heater plate temperature. The Pt100 thermometer, shown in figure 3.7, is a resistance thermometer which uses the linearity of resistance with temperature for thermometry. The error of the probe temperature and the voltage are the instrumental errors from the data logger. Since both variables are collected in the same device, the instrumental errors are the same.

In figure 3.7 the reserved space on the specimen was prepared for this calibration process. First a current in the range of 0.6mA to 0.8mA was passed through the probe. The probe would then approach to the sample, the scan size was set at 0nm with a slow clock time, this would activate the force feedback on the AFM. The probe would remain in contact with the sample surface during the calibration so that the vibration effects due to thermal transport were reduced. The clock time was dependent on how long the calibration was taken, in air the clock time was set

to 500μs and for vacuum it was set to 1ms. A longer time is required in vacuum as the signal to noise ratio is lower.

The Peltier heater was set to be 60 °C for heating. When the Peltier reached about 60 °C, it was switched off for the cooling process. This procedure is to verify there is a consistent calibration for both heating and cooling. The temperature range was chosen to give a wide range for the probe to cool down. The thermal calibrations for both environments were repeated 3 times for each probe or change of environment. The data logger collected the probe voltage and the Peltier temperature against time in seconds. Figure 3.9 shows a typical thermal calibration result from the data logger.

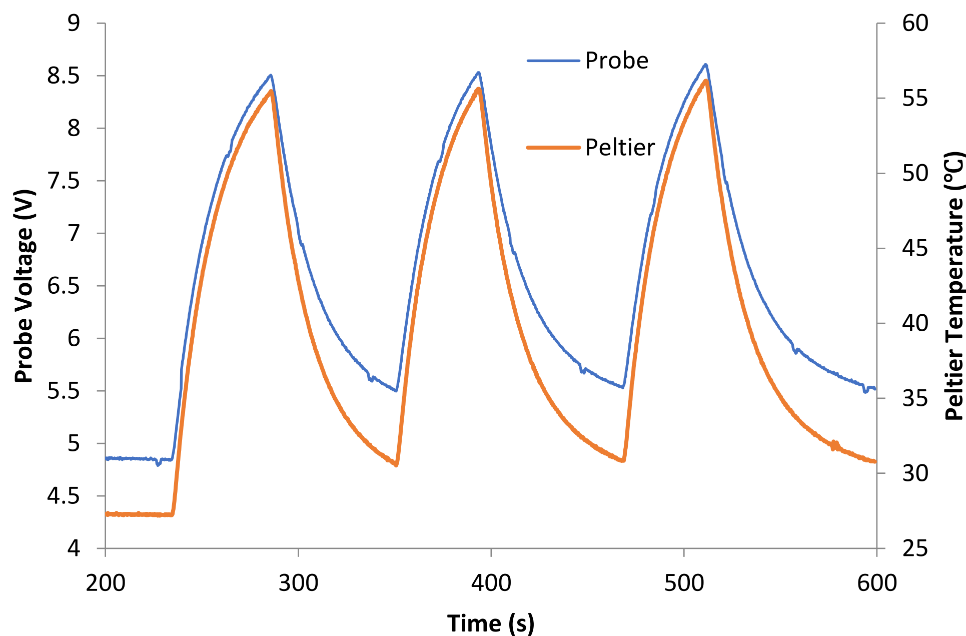

Figure 3.9 A typical result from the data logger for thermal calibration.

In vacuum, three different methods were used to optimise the setting. The first method was to heat up the Peltier to 60 °C and allow it to cool down by the environment. A temperature jump was observed during cooling with this method, indicated in figure 3.10. The cause of the temperature jump could be an instrumental error, however it was not identified. The second attempt was to heat up the probe by manually turning up the Peltier temperature to 60°C, and

then control the cooling down process by manually reducing the power of the Peltier. The third attempt was an optimised version of the first attempt by heating the probe to 40 °C to avoid the instability. Although this same method was attempted in vacuum, the thermal calibration coefficient gave a false impression of the temperature conversion which will be discussed in chapter 5.

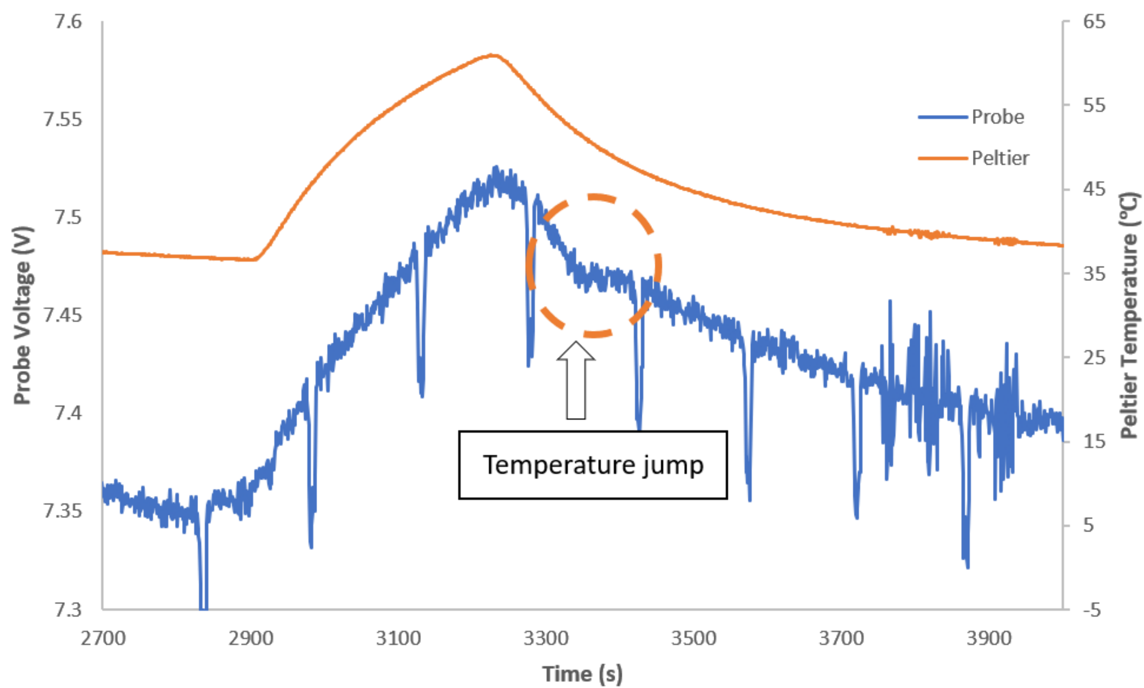

Figure 3.10 Figure of thermal calibration in vacuum heated at 60℃, the temperature jump during cooling is marked.

The cooling range was chosen by inspection for plotting the probe voltage against the Peltier temperature. Three graphs of the probe voltage against the Peltier temperature were plotted for each repeated measurement and a gradient was obtained by the line of best fit. The gradient is the probe voltage to temperature conversion for the experiment. The error for the gradient will be calculated from the standard deviation of the repeated values. Figure 3.11 demonstrates the method for obtaining the conversion coefficient.

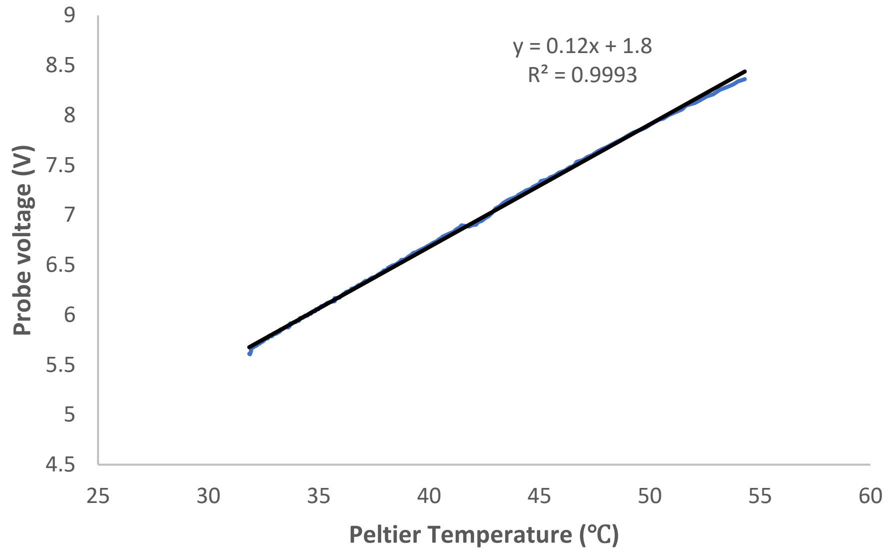

Figure 3.11 A typical measurement of probe voltage against Peltier temperature, a line is fitted for estimating the conversion coefficient from voltage to temperature.

A thermal hysteresis loop was observed during the analysis of the calibration, which will be discussed in chapter 5. The 0.6mA current was chosen to avoid overheating the tip. However, periodic noise was observed during the thermal measurements in vacuum so a 0.8mA current was used later to improve the signal to noise ratio. The source of the noise was not found during the thesis. This calibration method is only valid for calculating the change in temperature, because of the balanced bridge circuit the absolute temperature is not measured.

The thermal calibration was undertaken before thermal measurements in both air and vacuum and, as it was shown in figure 3.7, the samples are on the same specimen as the Peltier. During the calibration process, the sample was heated, which causes a problem for the thermal measurements. If the sample temperature is higher than the tip, the thermal experiment will not be valid therefore, the sample must be cooled down to a stable temperature before making any thermal measurements. The sample cooling was monitored by the Peltier signal through the data logger. The samples will take longer to cool down to a stable temperature in vacuum, this is because cooling is only via radiation.

The thermal measurements procedure is similar to the force measurement described in the chapter 3.5. Once the topography of the samples has been measured and the area is chosen, the thermal measurements were made by feeding the thermal information into the AFM feedback module. The data logger was used to monitor the probe voltage during the thermal measurements. This is to record the change in temperature when the tip is far away from the sample and to monitor the probe in case of short circuit. The clock setting and the tip displacement for thermal measurement should be the same as force measurements, this is to ensure both the force and thermal measurements are comparable.

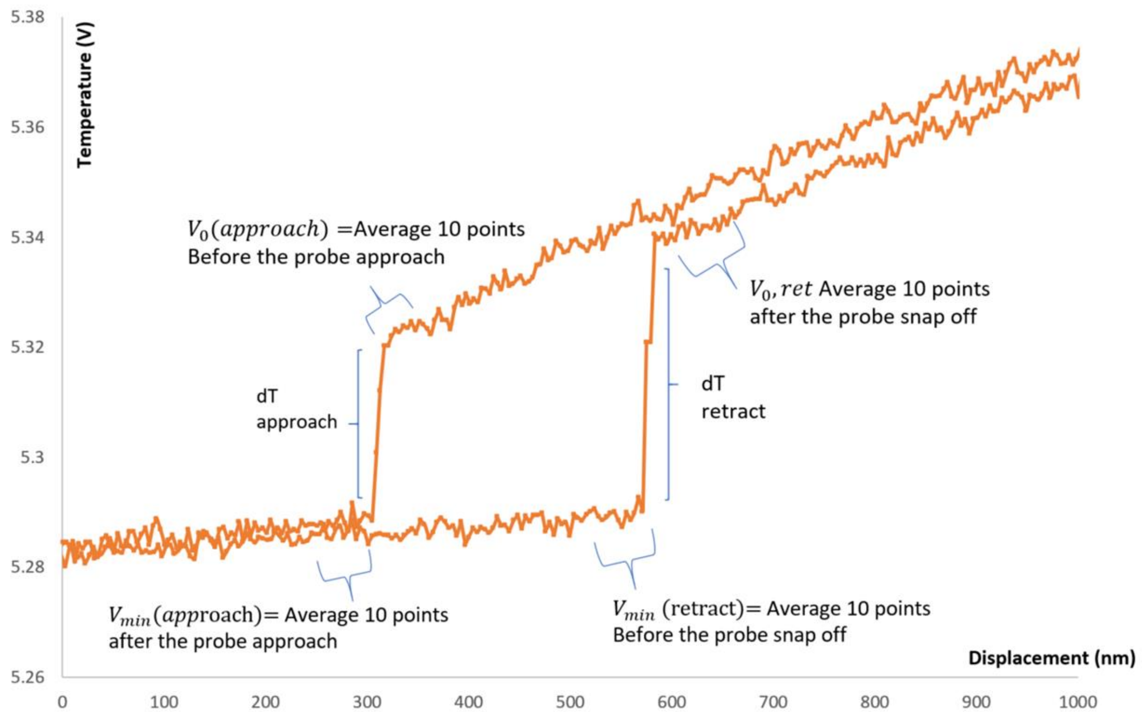

Figure 3.12 Illustration showing a close up of a thermal hysteresis with explanation of how to measure the change in temperature.

A generic shape of the thermal curve result in air is showed in figure 3.12. The thermal curve forms a hysteresis loop, showing the displacement on the x axis and the temperature on the y axis. Figure 3.12 shows a measurement taken in air where the temperature drops suddenly as it gets in contact with the sample. Figure 3.12 also shows how the change in temperature is measured.

When the tip retracts, the adhesive force on the sample surface will keep the tip in contact. Since the tip is constantly retracting this causes a bending of the cantilever, until the retract force is sufficient to overcome the adhesive force at which prompt the tip will then snap out. After the tip has snapped out, the distance between the tip and sample will depend on where the stage has got to in the retract cycle. On the data logger, the snap-out change in temperature will be larger than the snap-in change in temperature. The snap-in change in temperature is more representative of the thermal conductivity. This is because the snap-out change in

temperature is affected by the adhesive force varies between samples. The snap-in change in temperature is less affected by the mechanical properties of the samples, hence it is more representative of the thermal properties. Since the snap-in change in temperature happened during the approach process, we will call this the 'approach temperature' and it is marked as 'dT approach' in figure 3.12.

The approach temperature measurement is marked in figure 3.12. It is made by measuring the average temperature of 10 points before and after the tip made contact with the sample surface, then the difference of these values is the approach temperature. Ten points were chosen as a balance between averaging over as many points as possible to reduce noise, but making sure that the value is not affected by real temperature gradient due to the cooling of the tip.

The range of points for measuring the change in temperature is showed in figure 3.12. When analysing the data, the force curve will be plotted on the same axis with the thermal curve. The intersection of both curves shows the snap in and snap out point of the tip. The range of points is then chosen at this intersection by inspection and the range of points will be used for calculations. The error is estimated by the standard deviation of the measured dT through the repeated values. There are some parameters to be aware of for the temperature measurements, for example, the laser signal and the electrical current through the tip will contribute to the temperature reading. A significant amount of laser signal heating the tip was observed during the setup of the thermal calibration. This effect is neglected when analysing the change in temperature in this project, however it should be taken into account when working out the absolute temperature in the system.

Chapter 4 Topography and force curves measured using contact mode and thermal probes

This chapter presents the results for the mechanical measurements made by the SThM. The aim of these mechanical measurements is to investigate the relationship between the adhesive force and the hardness and elastic modulus. Understanding the topography of the sample and the material properties should provide an aid to interpreting the thermal measurements. For example, the surface hardness can affect the contact area of the tip and cause a change in thermal conduction. The force measurements are also used to verify the contact point of the tip in the thermal measurements, hence the study of the mechanical properties is important for analysing the thermal measurements too.

This chapter presents the force measurements results including the probe dimensions, the calculations of the probe spring constant and the force measurements of different sample using thermal probe. This chapter will conclude by comparing the roughness analysis with the samples and comparing the force measurements.

4.1 Physical dimensions from SEM and spring constant results

The dimensions of the probes were measured using the SEM, there were four different probes used in this study: three thermal probes and one contact mode AFM probe, an SEM picture for all the probes are labelled and shown in Figures 4.1. The measurements from the contact probe were used as a reference for comparison.

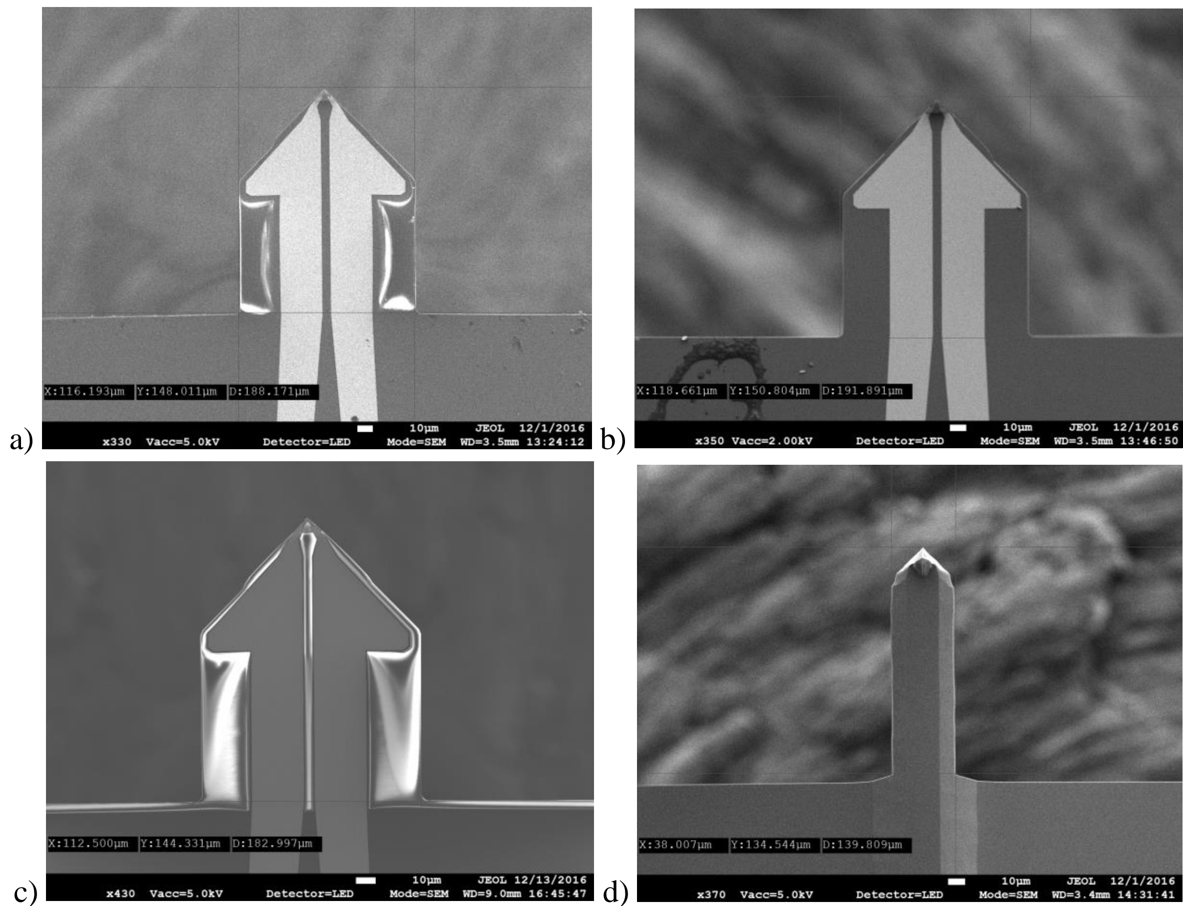

Figure 4.1 shows the SEM image for all probes used in this project. Figure a)-c) are the thermal probes A-C and d) is the contact probe D, the figures above were measured with the scale bar of 10 µm.

The figure 4.1 shows the SEM image of the four tips that were used in the experiment. The SEM images were measured with the scale bar of 10µm. The thermal probes A – C all have a similar shape and dimension since they are same type of probes. The contact probe D is showing to be narrower compared to the thermal probes. This is because there are no electronic contacts required on the contact probe.

Table 4.1 presents the SEM measurements for each probe. The table is presented in two parts, the top table gives the results of the dimensions of the probes measured by SEM. The bottom part is the calculated spring constant from the dimensional method discussed in chapter 3 along with the current applied during the thermal experiments.

	Unit	Symbol	Probe A	Probe B	Probe C	Probe D
Young's Modulus	GPa	E	290±30	290±30	290±30	150±20
Width	μm	w	116±1	118±2	113±1	38±1
thickness	μm	t	1.0±0.1	0.9±0.1	0.56±0.01	3.4±0.1
Length	μm	L	148±1	151±1	144±1	134±1
spring constant	N/m	κ	2.6±0.3	1.6±0.4	0.5±0.1	23.1±0.2
Current used	mA	I	0.6±0.05	0.6±0.05	0.8±0.05	N/A
Resistance	Ohm	R	336±0.5	331±0.5	340±0.5	N/A
Tip apex radius	nm		N/A	N/A	59±20	47±20

Table 4.1 Dimension measurements and spring constant calculation for all the probes. [35], [36], [38]

Table 4.1 shows the measured dimensions and the calculated spring constant for each probe. The contact probe D is the contact probe that is used for reference, its dimensions, Young's modulus and the spring constant are expected to be different from the thermal probes. There are several direct comparisons that can be noted in table 4.1. The Young's modulus values were looked up from the material data reference [36], [38]: the thermal probes were approximated to 290 GPa and the contact probe to 150 GPa. The dimensions of the contact probe D are smaller than thermal probes, except the thickness which is approximately 3 times thicker than the thermal probe A.

When comparing the spring constant between probes A – C, the results show a variation from probe C with 0.5 N/m to probe A with 2.6N/m. It is noted that there is an increasing trend of thickness with the spring constant, this can be shown in the calculation of spring constant in

equation (10). The spring constant is directly proportional to the Young's modulus, width of the cantilever and the thickness; the power factor in equation (10) makes the thickness more important to the spring constant calculation.

The spring constant assumed all the probes are rectangular shape therefore the calculated value is only an approximation as a guide for comparison. The Young's modulus for thermal probes is approximated as silicon nitride, note that the fabricated gold connections could affect the effective Young's modulus of the cantilever. Since the spring constant was used as an approximation, the effects of the gold were neglected. The Young's modulus for the spring constant was looked up from the material tables and was provided as a range of values. [35] The median value of the Young's modulus was used in estimating the spring constant and the range was used as an error, this gives approximately a 10% error for the thermal probes and a 13% error for the contact probe on the Young's modulus.

There was a challenge when measuring the thickness of the thermal probes thickness, probes A and B were found to have an impurity on the cantilever as this is shown in figure 4.2.

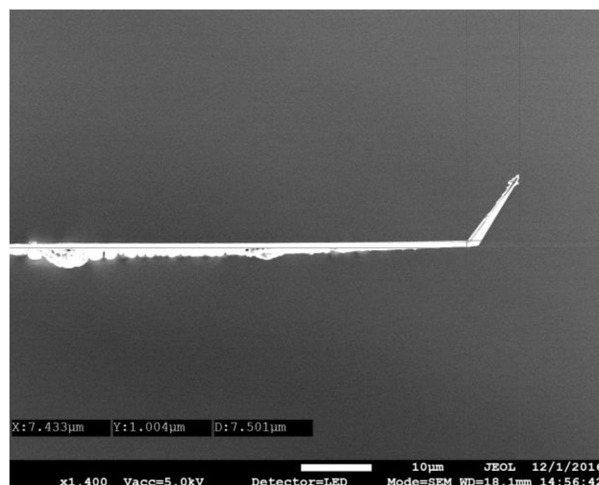

Figure 4.2 The impurities on the cantilever of probe A, the impurity is located towards the holder on the left-hand side of the picture. This could potentially affect the spring constant estimation.

The thickness of the cantilever quoted in table 4.1 neglected the impurity shown in figure 4.2. This is based on the presumption that the mass of the impurities relatively low such that it does not cause a significant impact on the calculation. The error on thickness accuracy was the same in all thermal probes, this is because the magnification was set to be the same. During the SEM measurements, a thermal drift was discovered when the scale bar reaches less than 100nm, this drift only affects measurements in fine scanning mode. A fast scanning mode was used in measuring the tip apex, this gives a lower resolution image but the results are more representative of the probe shape and dimensions.

The tip apex radius is an attempt to estimate the tip contact area, this will only be used in comparison between contact and thermal probes and was not required in any calculations. The tip apex was only measured for the contact probe D and the thermal probe C, this is because thermal probes A and B were damaged during the experiments. The apex radius of the thermal probe C is 58.9nm and for contact probe D is 47nm. The contact probe apex was expected to be significantly smaller than the thermal probe, however the apex sizes are similar in the measurements. From this comparison, the results suggest that the topography spatial resolution between both probes C and D will be similar since it is dependent on the tip apex size. The image of the tip also shows that there is a soft edge of the end of the tip, this is because of the diffraction on the SEM. The error was estimated between the diffraction area shown on the image and compared to the scale bar of the image.

The thermal probes resistance was measured before the experiment to ensure the probe was not damaged. The electrical resistance was also measured after the probe was inserted to the probe holder, this is to ensure the connection between the probe and the holder is secure. There was some instrumental failure during the experiment, the electrical signal for probe A was lost during the experiment in vacuum and the probe was replaced with probe B. The

resistor on probe B was found peeling off from the tip in SEM scan after a set of force and thermal experiment. This is shown in Figure 4.3. The probe C was used in repeating the experiment. The contact probe D was used as a reference for comparing the effects with thermal probe.

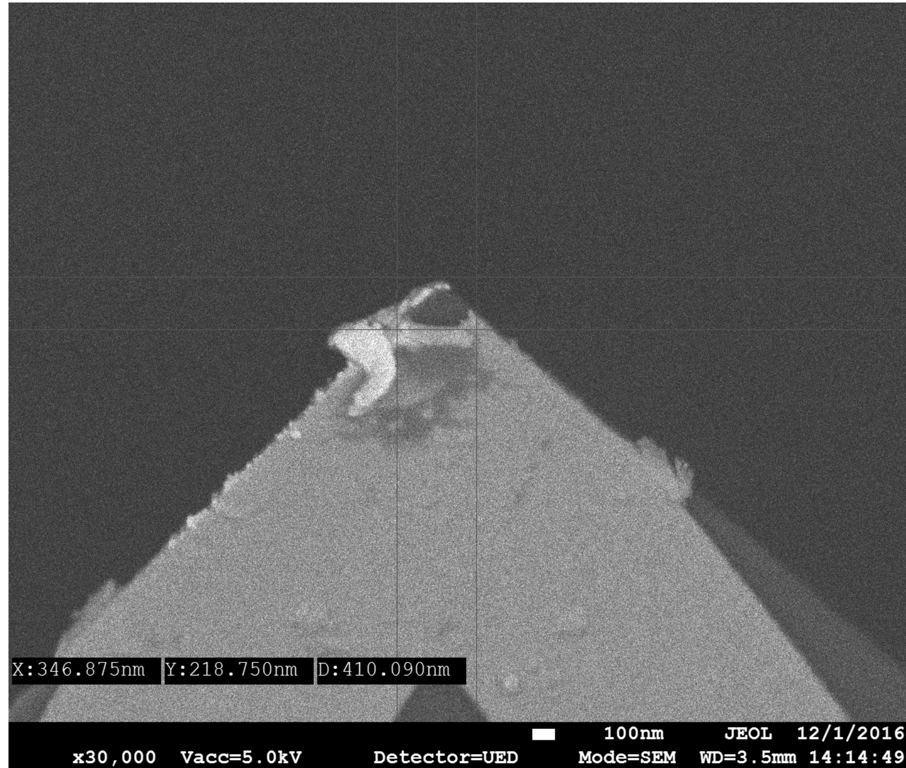

Figure 4.3 The SEM image of probe B with layer of palladium resistor coating peeling off after measuring a set of thermal measurement. The scale bar of the figure is 100nm.

In summary for this section, the spring constant of all four probes are presented and the error was discussed. The measurements also showed that the thickness of the cantilever dominates the spring constant calculation. The tip apex was only measured for two probes, the difficulties and the error were also discussed.

4.2 Topography and roughness analysis

The topography is required to complement the force and thermal measurements, a topography scan with high resolution can improve the overall inspection of the sample surface. In section 4.1, the results showed that the contact probe and the thermal probe have different spring constants and different tip dimensions. The first result is to compare the topography measured by the different tips. Figure 4.4 shows the different topography measurements between contact probe and the thermal probe.

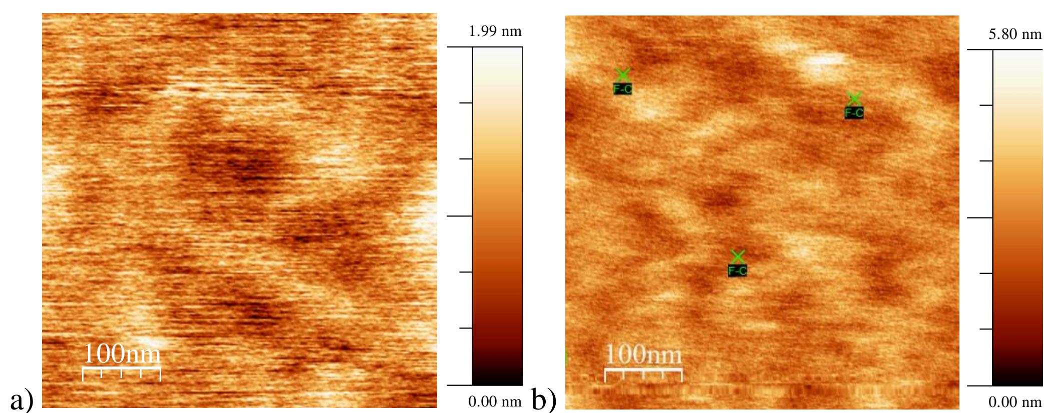

Figure 4.4 Silicon carbide topography measured with a) contact probe and b) measured with thermal probe C. The figures represent a similar area of the silicon carbide.

Both the contact and thermal probes were operated in air when producing the topography in figure 4.4. The marks on figure 4.4b) are the locations where the adhesive force and the thermal measurements were taken. The contact probe should give a more detailed image of topography if it has a smaller tip apex size. However, in section 4.1 the tip apex radius was showed to be similar between the contact probe and the thermal probe, hence the topography in figures 4.4 does not have a significant difference. In addition, the thermal tip is more capable in detecting smaller features with the thermal image, hence the roughness analysis will also be using the thermal probe.

The topography procedure in figure 4.4 should ideally measure the same area on the sample, however to measure with two different probes, a change of the probe holder is required and

this resulted in a change of measured area on the sample. The only attempt to return to the same area is, during the change of probe holder, the sample specimen is fixed in place to try and maintain a similar measuring area when a new probe is inserted. However, with the scanning size of 500nm, it is impossible to mark out the exact area for repeated scanning using the optical microscope, therefore the result above can only be compared within the sample. The tip apex radii were estimated after both force and thermal experiments.

In figure 4.4, the observation of the wavy pattern is visible on both diagrams. This suggests that the interference is not caused by the type of tip is used, since it is also observed in most topography and thermal map results. It is suspected there is an interference caused by the laser signal, however no investigation was attempted to resolve this phenomenon as the single point measurements of force and temperature were not affected.

The average height across the scan area is used to compare the flatness of the surface. The SThM measures the height of the sample from a reference point and marked as 0nm. The RMS roughness is the standard deviation of the height at a point from the average height, this gives a measure of how much variation of height there is across the surface which is also a measure of roughness. The other parameter measured is an estimate of the typical width of the surface features taken from the line scans.

The average height of the silicon carbide measured with the contact probe (Figure 4.4a) is 1.02nm with an RMS roughness of 0.35nm. The average height measured with the thermal probe is 1.66nm with the RMS roughness of 0.37nm. By converting the RMS value to percentage of average height, the contact probe gives a surface variation of 34% while the thermal probe gives 22%. This study was an attempt to investigate the difference in contact probe and thermal probe, however since the scanning areas are different, the result would require repeated measurements for further deduction. As the contact probes are not providing

much additional information, the thermal probes are used for the topography analysis of the samples so that they match the thermal scans.

The topography result for each sample will be presented in the following section. The results will be presented with the topography and with a profile for roughness analysis. The topography was measured using the thermal probe, for the convenience of obtaining the force and thermal measurements later. The presentation will include a list of numerical results, this includes the average height of the topography scan area, the RMS roughness of the average height and an estimation of the dimensions of the surface features. The line scan positions were chosen to be representative of the area and two of these were measured to estimate the feature size for each sample. The force curves are presented at the bottom of the figures, it is the average of all 9 curves taken from three different areas. The left force curve is measured in air and the force curve on the right is in vacuum. The analysis of the force curve will be discussed in the next section.

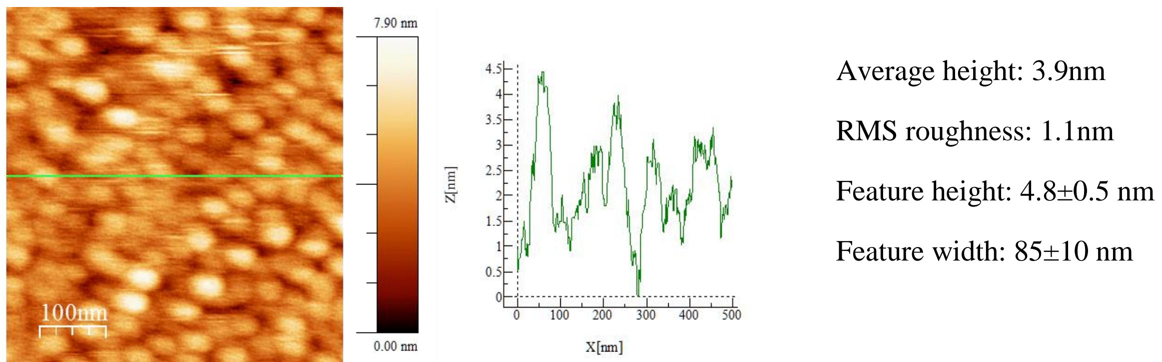

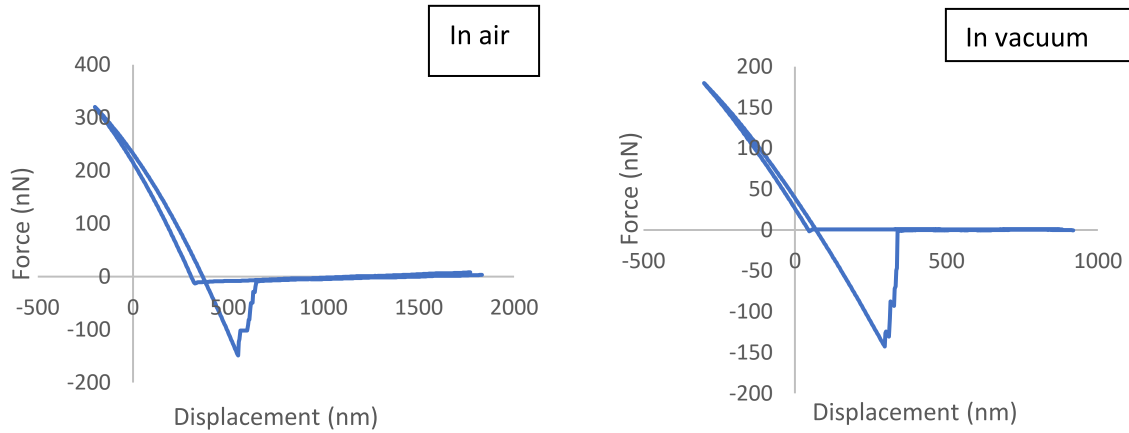

Figure 4.5. Roughness analysis of gold thin film.

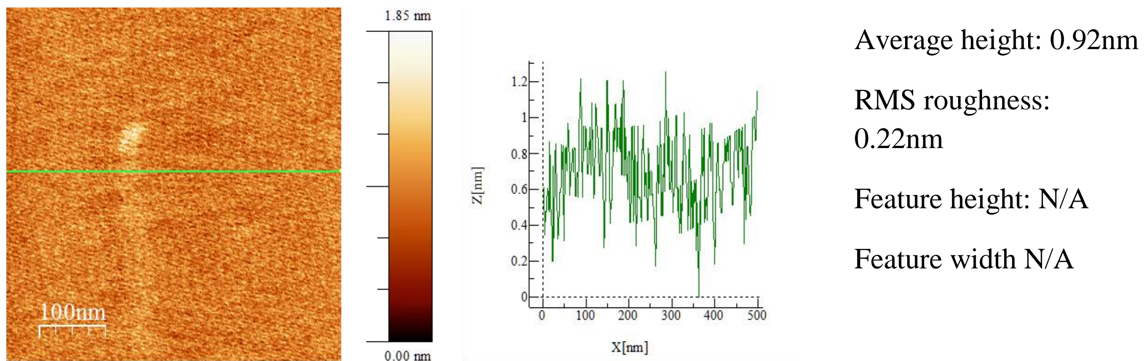

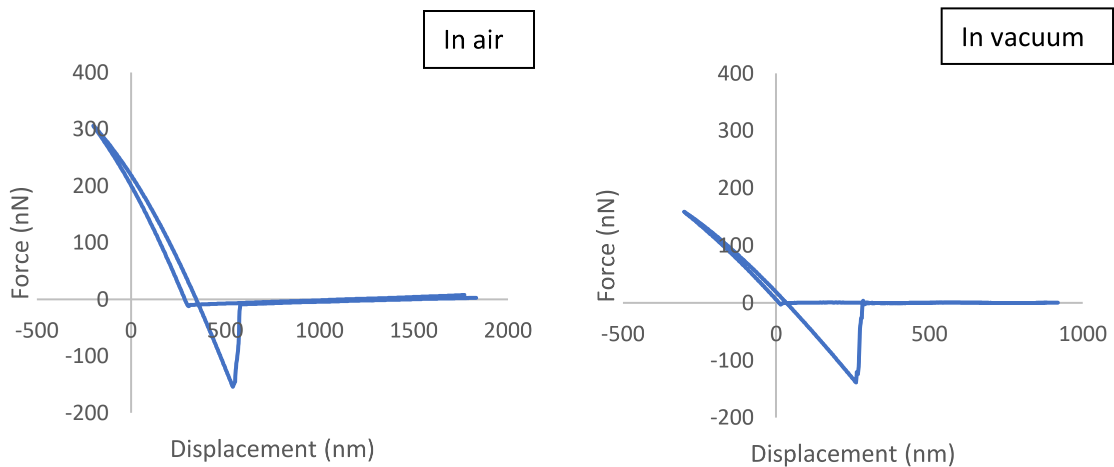

Figure 4.6. Roughness analysis of mica.

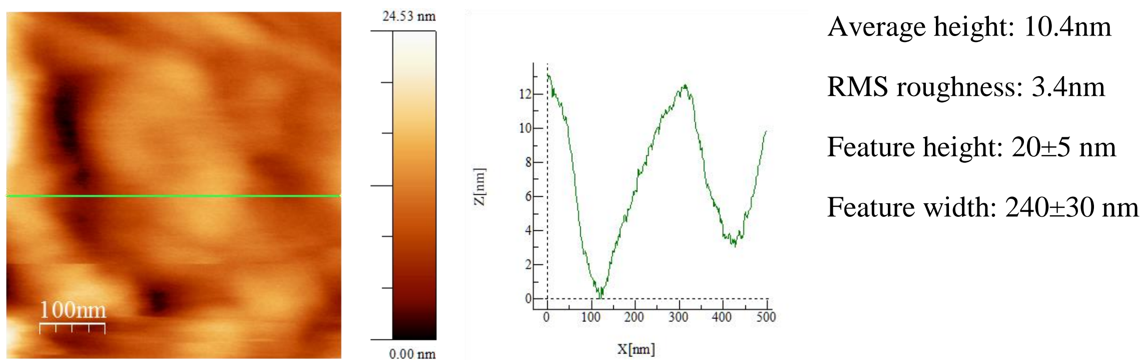

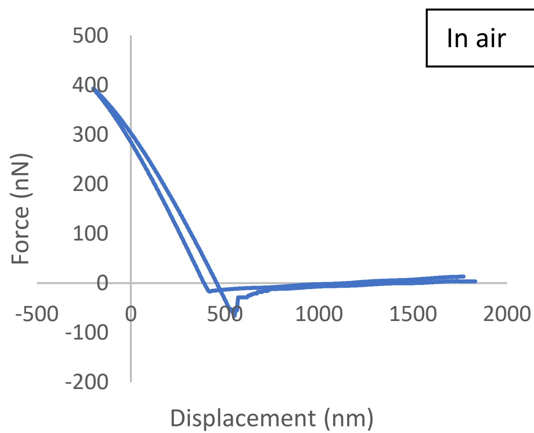

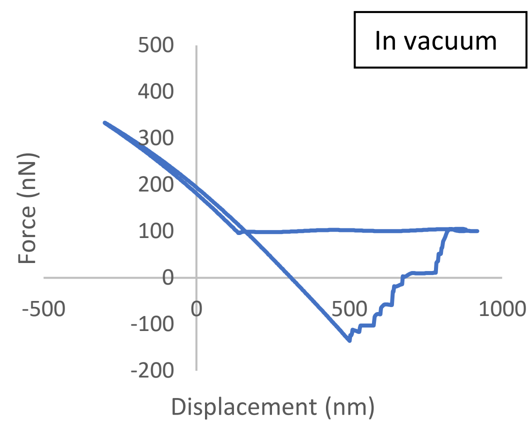

Figure 4.7. Roughness analysis of PTFE.

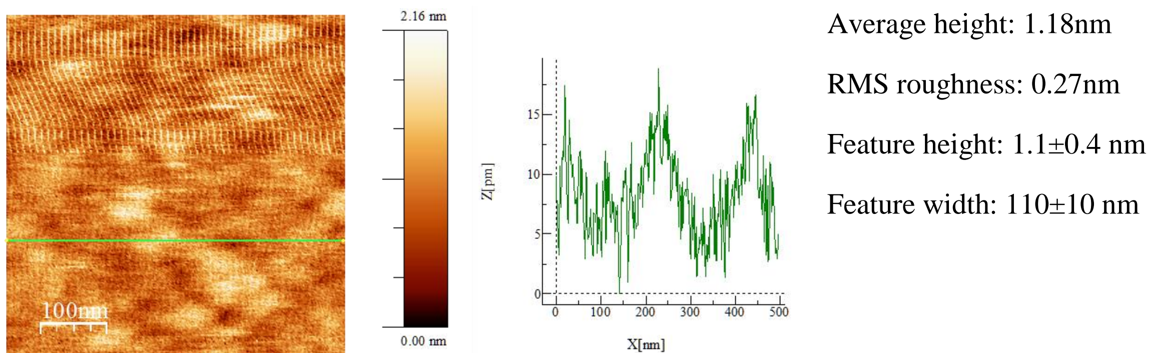

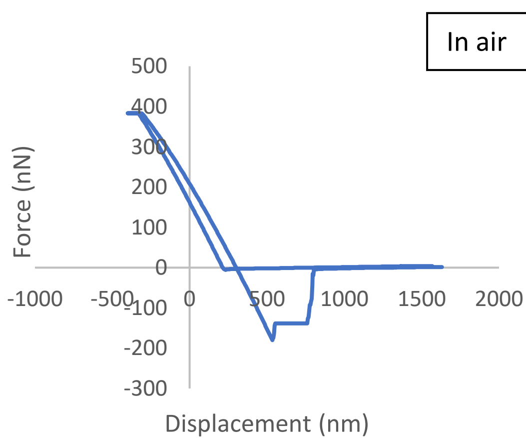

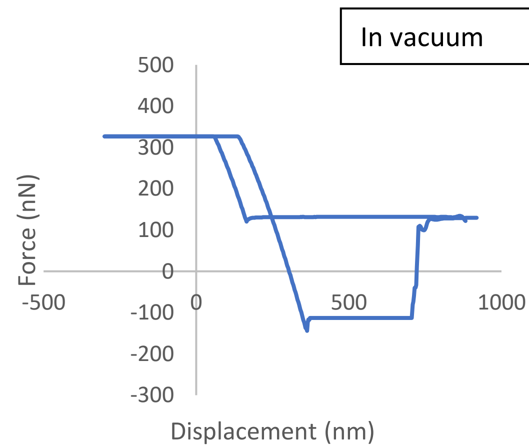

Figure 4.8. Roughness analysis of silicon.

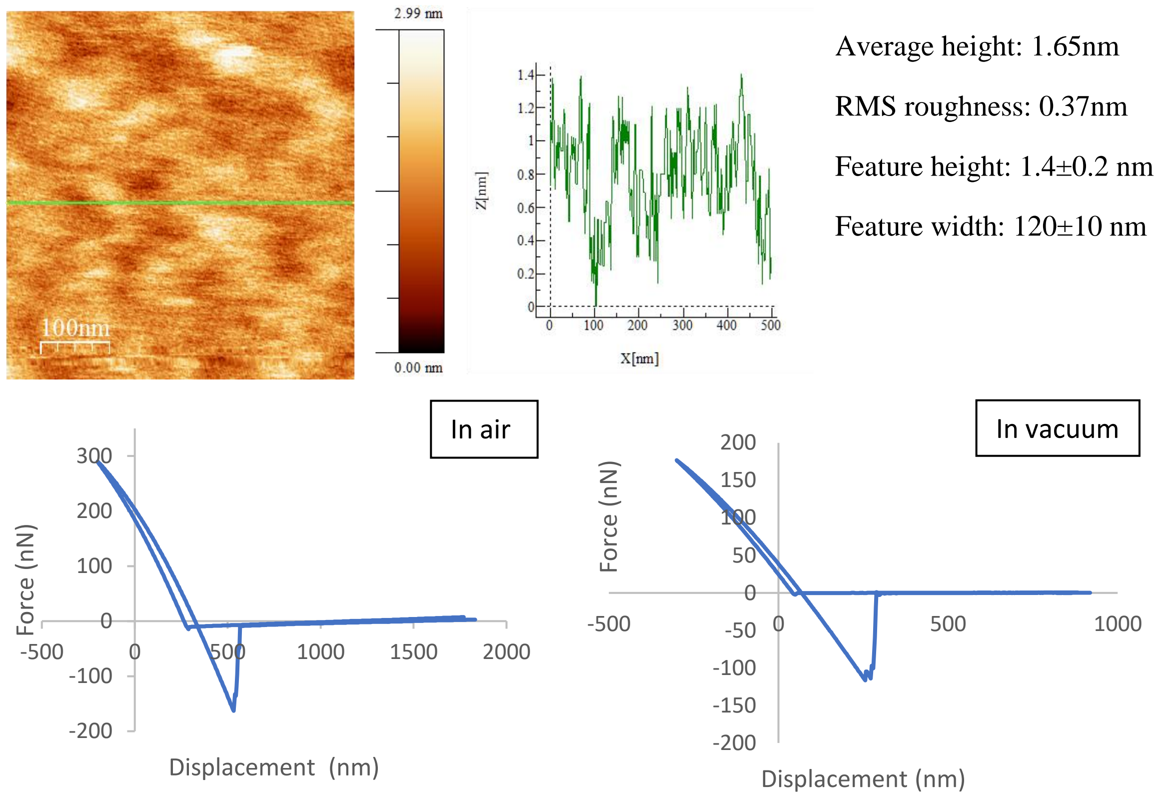

Figure 4.9. Roughness analysis of silicon carbide.

Figures 4.5 to 4.9 show an overview of the topography of the samples and the values are summarised below in table 4.2. The first result presented was the gold thin film, it has distinctive surface island features visible in figure 4.5. The gold feature width is comparable to the tip apex radius of about 50nm, the tip radius will limit the lateral size which can be detected.

The PTFE showed some features from the topography that are measurable, the features have the largest width from the set of samples measured. The PTFE has the highest average height of 10.4nm, this indicates that the surface variation is large in comparison to other samples.

Mica picked up some interference noise in the topography, the surface feature cannot be shown on the topography, this could be that the features are smaller than the interference signal. The average height is the smallest of all the samples, it indicates that the mica surface is the smoothest of all the samples.

The result of silicon shows some interference at the top part of the topography, the features can be seen and measured. The line profile of silicon was measured towards the lower end of the topography, this is to avoid the interference pattern.

Silicon carbide topography was presented, the result is similar to silicon, where the sample features were shown. The line profile also shows the noise picked up from the interference.

The next part will be presenting a summary of the numerical results measured from the topography. Table 4.2 presents a summary of the measurements including the hardness and the elastic modulus recalled from chapter 3.2.

Material	average height (nm)	RMS roughness (nm)	RMS roughness %	Feature width (nm)	Feature height (nm)	Elastic Modulus (GPa)	Hardness (Mohs)
SiC	1.7	0.4	22%	120±10	1.4±0.2	302	9
Si	1.2	0.3	23%	110±10	1.1±0.4	179	7
Mica	0.9	0.2	24%	NA	NA	170	2.5
Au	3.9	1.0	28%	85±10	4.8±0.5	79 (bulk)	2.5(bulk)
PTFE	10.0	3.4	33%	240±30	20±5	0.40	-

Table 4.2 Summary of the topography of each material.

Table 4.2 presents the data in order of descending elastic modulus for the convenience of comparing the values between the samples. The samples can be categorised into three different types. The first type is the soft material, PTFE, it has the lowest elastic modulus and hardness. The hard-bulk materials of silicon, silicon carbide and mica, all with high values of elastic modulus. Finally, the unknown deposited material thin film gold, the elastic modulus and the hardness given are the bulk values, the actual property of the gold thin film is not known.

The average surface height of the hard-bulk materials was found to be similar, this is indicating that the silicon, silicon carbide and the mica are sharing a similar roughness. From the topography, all of the materials in this category showed the interference however, only mica

does not show any surface features. The reason is the mica features are smaller than the interference signal.

The average height of PTFE is the highest at 10nm, this indicates that the PTFE has the roughest surface. The features showing on PTFE also have the biggest width of 240nm. The PTFE and thin film gold did not show any interference from the topography. The thin film gold showed some distinctive island features with 85nm in width and 4.8nm high. The feature width is comparable to the tip apex radius of about 50nm, the tip radius can affect the lateral size that gives a lower resolution in width. After converting the RMS roughness into the percentage of the average height, the percentage shows a weak directly proportional relationship with the elastic modulus.

4.3 Force measurements comparison between samples

The force measurements of the samples will be presented in this section. The force measurements were recorded in voltage, a conversion from V to nN is required for comparison and analysis, the conversion method is described in equation (6) and discussed in chapter 3.5. The spring constant was obtained in the chapter 4.2 by inverting the gradient of the retract region from the force displacement curve. The results are shown in table 4.3.

Probe	Sensitivity, α (nm/V)	%error	Spring constant, κ (N/m)
A	16.94±0.03	0.17	2.62±0.32
B	16.62±0.01	0.06	1.62±0.36
C (in air)	67.1±0.13	0.2	0.50±0.09
C (in vacuum)	56.6±0.1	0.13	0.50±0.09
D	27.5±0.1	0.19	23.10±0.16

Table 4.3 Table presenting the sensitivity a from inverting the overall average slope of silicon carbide.

The sensitivity measures the change in distance against the change in voltage defined in equation (7), but the force curve measures the voltage against the displacement. Therefore, the gradient measured on the force curve needs to be inverted for the correct sensitivity. The force conversion for all samples is done using the sensitivity measured on silicon carbide. The reason is the thermal probe is made of silicon nitride, if the sample surface is soft, the cantilever will push into the sample without bending the cantilever significantly, this leads to a false presentation of the sensitivity. Silicon carbide is therefore chosen for measuring the sensitivity since it is the hardest material from the sample set, there is less likelihood of the silicon carbide surface to deform, however, it is possible that the hard surface of silicon carbide will damage the thermal contact of the tip.

The force results in Figure 4.10 illustrate the difference between a thermal probe and a contact probe. The figure shows the measurements of silicon carbide in air, the force is measured in voltage and has not been converted.

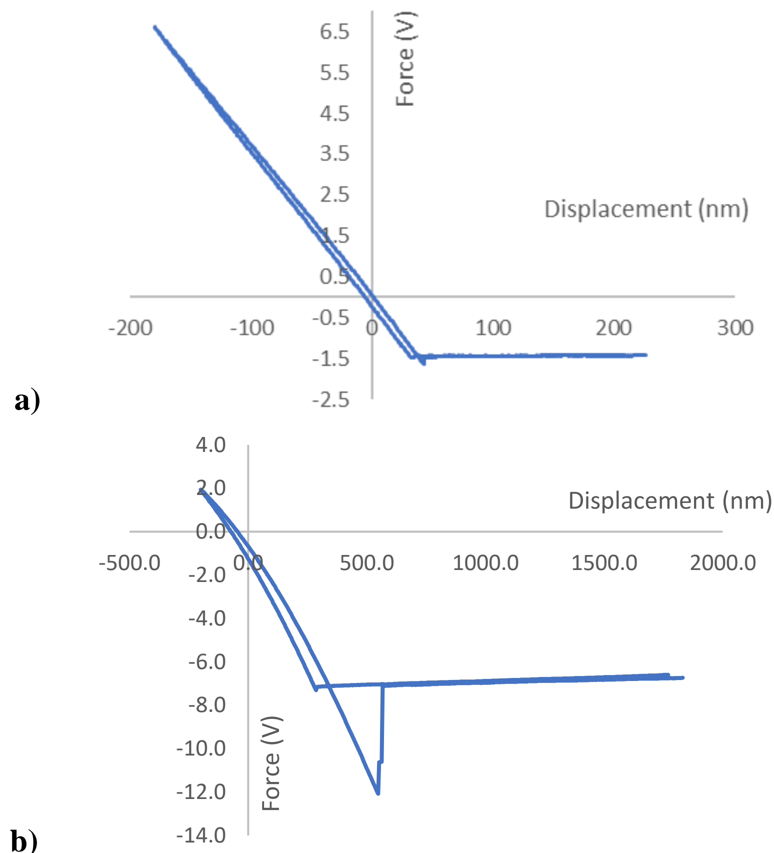

Figure 4.10 Force measurement results of silicon carbide measured in air with a) the contact probe D and b) the thermal probe C.

Figure 4.10 a) is a result from the contact probe, the first observation is that the adhesive region is significantly smaller than that from the thermal probe in figure 4.10b). The contact probe has much higher spring constant than the thermal probe, the higher spring constant of the cantilever provides an extra force to overcome the surface adhesive force, resulting in the small adhesive region for contact probe. In contrast, the thermal probe has a smaller spring constant compare to the contact probe, hence the surface adhesive force is able to hold the tip in contact. When the cantilever provides enough force to overcome the surface adhesive force, the tip snaps out of the surface. As the z piezo tube is moving out during this period the tip is contact with the

surface, this makes the tip returns to a position that is further away than the contact point from the sample surface when the tip is released.

In figure 4.10 b), the gradient from where the tip is in contact and before the tip snaps out does not show a linear relationship. This bending of the curve affects the sensitivity measurement required in equation (7). The sensitivity approximation is estimated using the linear part of the retract area to avoid the bending. The reason for this observation was not investigated. Sometimes the limit of the force range was reached, as illustrated in Figure 4.11.

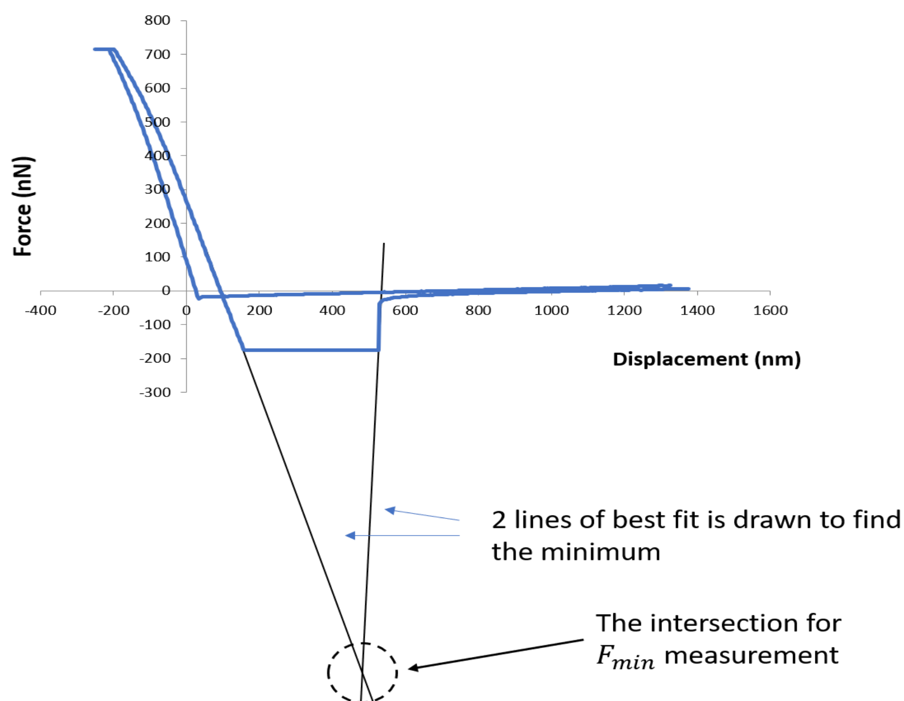

Figure 4.11 A diagram illustrating the force measurements that exceeded the AFM limit. Two gradients were drawn and the intercepts were used to determining the adhesive force.

In these cases, two lines of best fit were drawn along with the trend of the retract curve for finding V_{min}. The first line is fitted through the retract curve before the AFM reaches the limit. The second line is fitted at the snap out gradient, this gradient is often fitted for two points only, this is because the snap out process is too fast for the scan rate. However, this method relies

heavily on the data selection for plotting the gradient. The results were inconsistent and have a large error. The author tried to offset the force range of AFM to avoid this limit, the result was different and the typical results are shown in Figure 4.12.

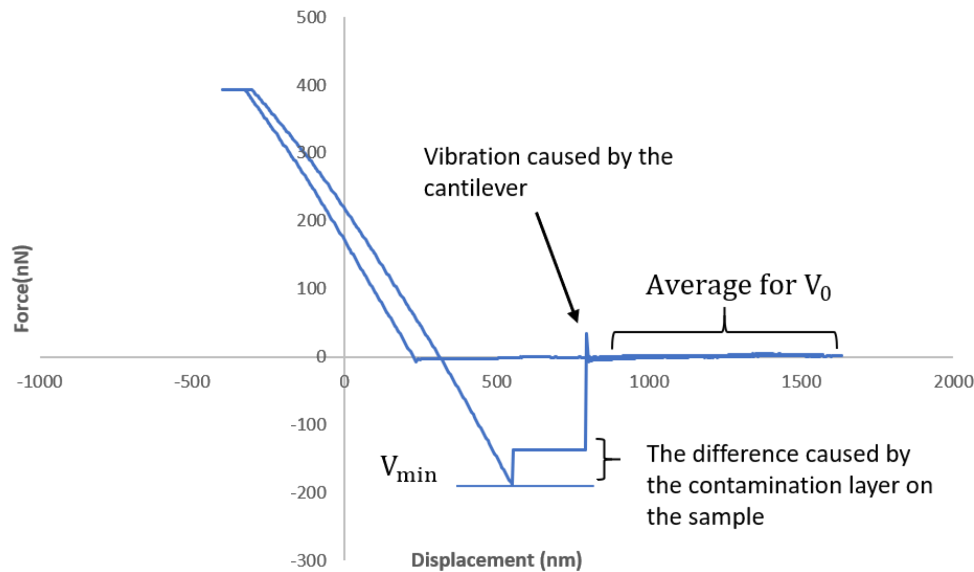

Figure 4.12. A diagram showing the typical force measurement result of silicon after the offset of sensor limit.

Figure 4.12 demonstrates the shape of the force curve from the result of silicon measured in air. There is an observation of cantilever vibration after snapping out, this is labelled in figure 4.12. The V_0 is chosen to avoid this vibration for the value used in conversion. During the experiment, an unusual shape of the force curve was sometimes observed.

The shape of the curve in figure 4.12 was different to figure 4.11, at the retract area, the flat region showed a sharp change below the limit, then returned to the flat limit before snapping out of the surface. This unusual shape of force curve is observed consistently in silicon and PTFE for both environments, it was also observed for to the thin film gold sample in air, but not for silicon carbide or mica.

A possible cause for this shape is the tip leaving the sample and then arriving at a contamination layer of material, before finally snapping out of the surface [40] or it could be an instrumental effect that has not been identified yet. Although the sample set materials were expected not to

have a contamination layer, it is possible to have an extra layer of moisture on the sample surface. It is also expected that there will be a layer of silicon oxide on the silicon surface and possibly even some residual resist from the patterning process. The V_{min} used in the calculations will use the furthest point of the tip before it jumped to the flat region, this is marked in figure 4.12. With the V_0 described earlier, the retract force was measured.

Table 4.4 presents the retract force results measured using the thermal probe. The result of thermal probe C only is presented. The table presents force measurements measured in air and in vacuum. The results are presented in the order of the descending order of elastic modulus.

Results of thermal probe C in air					Results of thermal probe C in vacuum			
Material	dF(retract) (nN)	% error	Elastic Modulus (GPa)		Material	dF(retract) (nN)	% error	Elastic Modulus (GPa)
SiC	175±2	1.11	302		SiC	133±5	3.9	302
Si	179±2	0.9	179		Si	153±6	3.8	179
Mica	165±0.3	0.2	170		Mica	144±3	2.2	170
Au	144±0.5	0.37	79(bulk)		Au	160±4	2.4	79(bulk)
PTFE	77±1	1.38	0.4		PTFE	145±10	6.7	0.4

Table 4.4 Retract force measurements using thermal probes.

The first comparison is the result between the environments. The retract force is generally larger in air than in vacuum except for gold and PTFE, which were also inconsistent from previous result using probes A and B. The reason for air to have a larger retract force is in air, water forms a layer on the sample surface, which has a high surface force and attracts the tip to the surface. [40] The gold and the PTFE are the least uniform samples, they have a large variation across the surface, therefore it is challenging for comparing in air and vacuum because the tip is at different position.

When comparing the results between the samples, a general trend emerged that the silicon, silicon carbide and mica have similar results. The silicon consistently has a larger adhesive

force than silicon carbide. For one set of data, the force curve of silicon carbide exceeded the limit of AFM, which gave the shape described in figure 4.11. In this case the silicon carbide adhesive force was larger than silicon, but the extrapolation method is not as reliable. We are therefore left with the observation that either the silicon carbide has a smaller value than expected or the silicon has a higher value than expected. As the silicon value is close to that of mica it looks more likely that it is the silicon carbide that is lower than expected.

The comparison then moved onto comparing the force value of mica. The force results for these samples are in general similar. The mica force value is observed to be consistently lower than silicon carbide in air, but vice versa in vacuum. When comparing the mica force values with silicon, the force value of silicon is consistently larger than mica in all environments. The values of silicon and mica are comparable in all environments, this is indicating the silicon carbide is showing a lower value than expected.

The mica usually returns a higher value than gold, from the table the gold shows a higher value in vacuum than in mica. The thin film of gold has unknown properties including hardness and thermal conductivity. Although the gold shows a consistent retract force, it was expected to have different properties from the bulk material and the island features may affect the variation across the surface.

The PTFE retract force is observed to be larger in vacuum than in air. The PTFE has a percentage error of 1.38% in air and 6.7% in vacuum for the retract force, it is significantly larger than other samples in both environments. Since PTFE has the softest surface, the surface deformation caused by the tip would introduce variation across the surface that leads to inconsistent results. The force curves of PTFE measured across the 3 different areas on the same topography showed a significant variation of the retract force. The retract force error for one area can be up to 6.2% in vacuum. This variation could be the main cause of error and is

showing in both air and vacuum. This is illustrated in figure 4.13, a force result of PTFE measured in vacuum. Since the both vacuum and air experiment were completed separately, it was not possible to mark out the exact same area for measurement, and the variation is therefore greater.

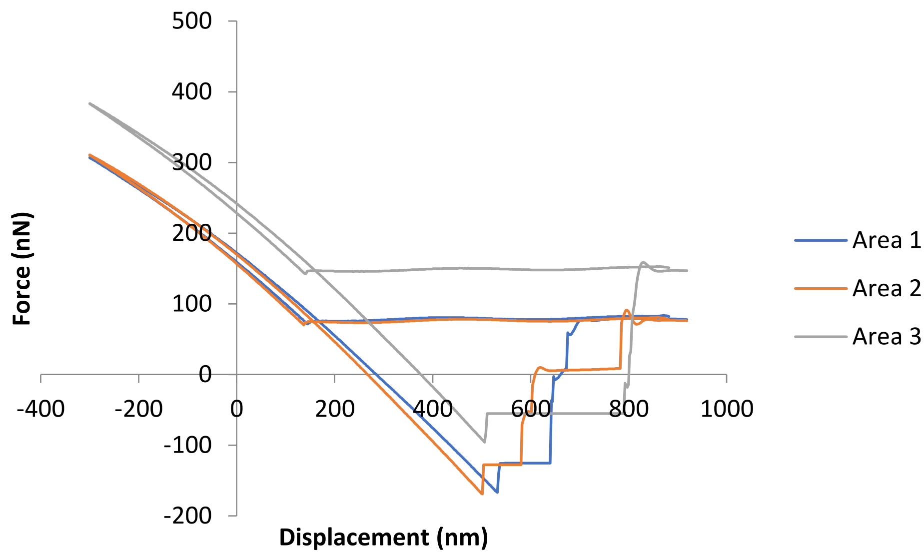

Figure 4.13 Force result of PTFE in vacuum, measured in three different areas showing the variation.

The retract force is the force of how adhesive the sample surface is when the tip retracts, the explanation of the curve is explained in chapter 2. The next discussion will be comparing the results to the roughness of the samples. There is not a clear correlation between the retract force and the roughness analysis. However, when comparing the retract force with elastic modulus, samples with higher elastic modulus were observed to have a larger retract force, except for the gold thin film. The gold thin film was quoted as 79GPa for the elastic modulus, however this is quoted from the bulk value, whereas the thin film value is not known.

4.4 Discussion of the results

This section discusses the challenges of making force measurements and summarises the achievements with the aims at the beginning of this chapter. The aim for the force measurements was to investigate the relationship between the mechanical properties, the adhesive force and the hardness. The topography improved the understanding of the surface features including the roughness.

The SEM results for measuring the dimension were first presented, the result showed the difference in characteristic for both contact and thermal probes. The contact probe has a higher spring constant when compared to the thermal probes. The contact probe cantilever is approximately 3 times larger than the contact probe, however, the contact probe is about 3-5 times thicker than thermal probes. The spring constant for each probe was then presented. Probe C was used for the main result presented in this thesis, the spring constant for probe C is 0.5±0.1 N/m. The contact probe did not show a clear adhesive region in the force curve due to its high spring constant of 23.1±0.2 N/m.

The challenges such as measuring the thickness due to the impurities and the focusing of the SEM was discussed. The theory for obtaining the spring constant was an estimation, this could directly cause a false presentation for the absolute value of force. Other methods of measuring the spring constant described in chapter 2 could be further investigated. For example, the possibility for using the reference cantilever method to obtain the spring constant could be investigated.

The SEM was used to measure the tip dimension for obtaining the spring constant, during this measurement, the tips condition was found to be unstable after being used for thermal and force measurements. For example, the palladium resistor coating was found to be peeled off after the thermal experiment, as shown in figure 4.3. This raised a question about the reproducibility of

measurements as the tip changes. The durability of the tip will directly affect the cost for the experiment and the performance of the tip will affect the accuracy of the measurements. Therefore, the SEM process was added to check the tip before use.

The next discussion is comments on the roughness analysis. The thin film gold is the only sample which showed surface features such as islands, resulting from the thin film deposition. The mica was showed to be a flat surface, the reason could be the features are smaller than the interference signal. From the average height, mica was shown to be the flattest surface. Further investigation on the source of interference is more important, particularly for the harder materials. When comparing the force measurements with roughness, it would also be possible to set up an experiment of the same type of material with different roughness. The PTFE showed the greatest variation in average height due to the very soft surface. The consequences for the surface roughness will be considered for their impact on the thermal properties in the next chapter.

The results in chapter 4.3 summarised the adhesive force measurements. The change in force was described as adhesive force in this thesis because it is the amount of force on the surface that attracts the tip. The difficulties of measuring the adhesive force when it reaches the limit of the AFM was discussed. The method suggested in this thesis was to estimate the force by fitting the intersection of two lines. However, this method has given an error on the estimated force which is not usable, therefore the author attempted to adjust the range of force on the AFM to avoid the situation and an unusual curve was observed showed in figure 4.12. The unusual force curve shape was discussed and suggests that there may be a contamination layer on the sample surface. This contamination layer was consistently detected on silicon, which an extra layer of silicon oxide was expected on the silicon surface. A contamination layer also consistently detected on PTFE while the PTFE consistently exhibited to the lowest adhesive force.

To summarise, the force measurements in air are generally larger than in vacuum, this is due to the layer of water formed on the surface which increases the adhesion. The adhesion can vary across the surface, in the PTFE result the force curves were observed to have a step variation across the area, which caused a large average height of 10 nm in roughness analysis. The adhesion is particularly strong with silicon, but this was not always consistent. The silicon showed an unusual shape of the force curve, which may be a result of an extra layer of different material on the silicon surface i.e. silicon oxide. The adhesive force can be investigated from the chemistry point of view, where the surface bonding and structure should be investigated for a more comprehensive conclusion.

The samples in this experiment were chosen for their range of thermal conductivity. If further mechanical analysis is required, the sample choice should add comparable samples, for example the bulk gold and the thin film gold for direct comparison.

Chapter 5 SThM for thermal conductivity measurements

The aim for the thermal measurements is to first compare the thermal effects between air and vacuum, since the environment can affect the heat path in SThM. The thermal measurements will also be used to investigate how the mechanical properties affect the thermal results. The thermal curves of the different samples will be compared and assessed for the feasibility of making quantitative thermal transport measurements.

This chapter will present the following thermal measurements result. The signal from the data logger and the thermal calibration will be presented, with a discussion on signal conversion from voltage to temperature. The topography of each sample will be presented along with the thermal map and the thermal curve in both vacuum and air. The comparison of the thermal conductivity and the change in temperature for the different samples will be discussed and the implications summarised.

5.1 Thermal calibration and probe signal from the data logger

Throughout the thermal experiment, the data logger is constantly monitoring the voltage across the tip. The data logger is a useful part of the thermal measurements, it collects the temperature information from the Peltier for thermal calibration. It is also used to alert the situation when the probe circuit is being damaged during the experiment. The discussion starts with the explanation of the data logger data. Figure 5.1 shows a typical result from the data logger for thermal measurements.

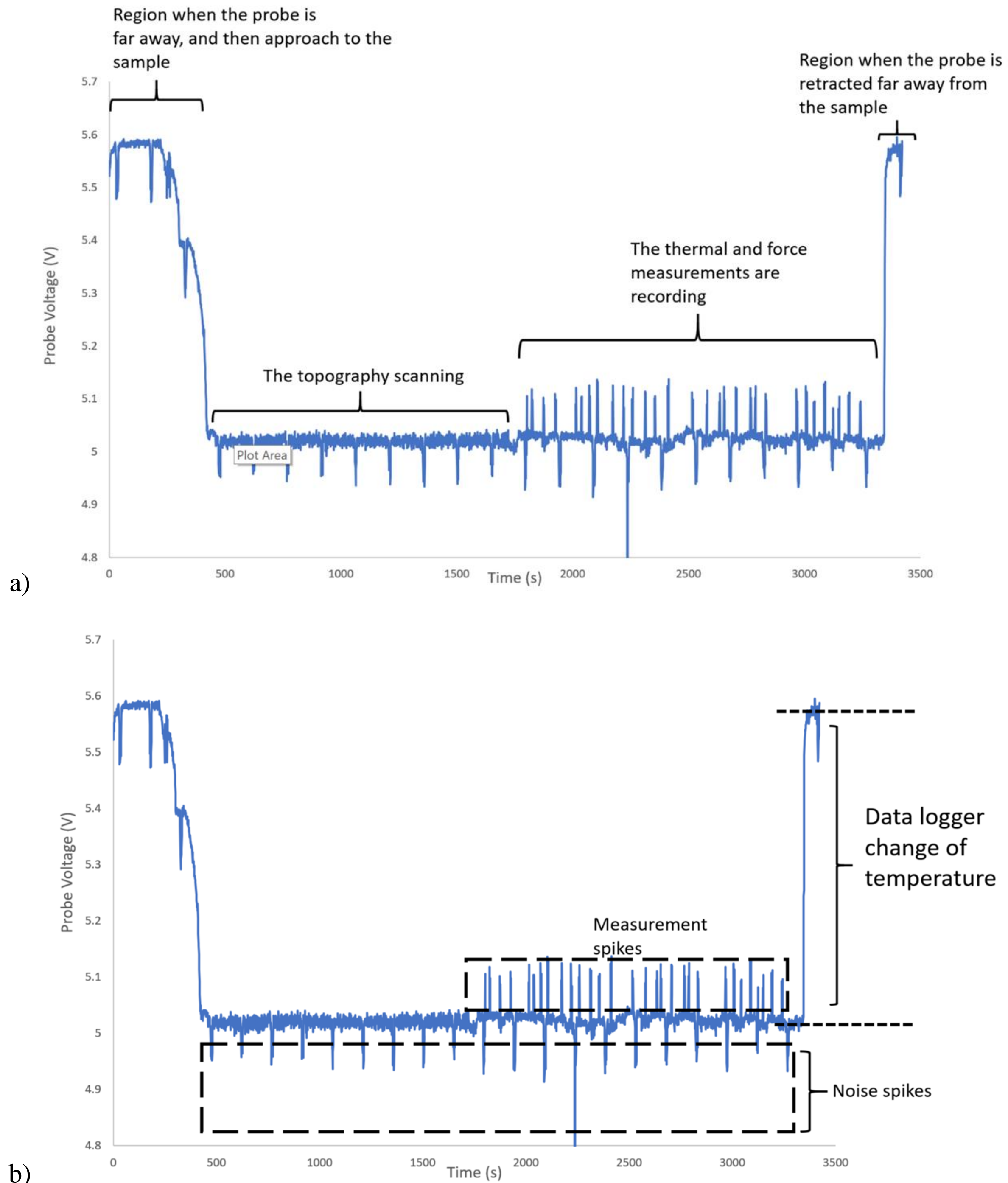

Figure 5.1 a) A generic result of data logger recording in air. The diagram illustrates each part of the curve during the experiment. From the beginning there is a potential difference drop for approach until the tip is in contact with the surface. Then the potential difference remained during the topography scanning. b) Continue the same diagram with labels of the measurement spikes, noise spikes and indication of the data logger change in temperature. The measurement spikes are indicating the temperature changes during the force and thermal measurements. The noise spikes are caused by the 40-second periodic instrumental noise. The data logger change in temperature indicates the temperature difference between the tip in contact and out of contact of the sample.

At the beginning of the data logger recording, the tip is far away from the sample, then the temperature drops during the approach process. It is noted in figure 5.1a that there is a steep drop of the temperature during the approach process, this is because the specimen was approached through a manual process. The distance of the probe and the specimen was monitored by an optical microscope. Once the specimen is close enough that it cannot be identified whether it is in contact, the AFM takes over for the fine approach.

When the temperature stops dropping, the tip is in contact with the sample. The tip would then start scanning the topography of sample. Then the next step of the data logger curve shows the probe temperature when the tip is measuring the force and thermal measurement. The force and thermal results were repeated at 3 different points on the sample.

During the force or thermal single point measurements, the tip is programmed to approach and retract to a pre-defined starting position, and reprogrammed to repeat. This is the procedure that is programmed inside the AFM. It is obvious that when the tip is not in contact with the sample, the tip temperature rises as there are fewer heat paths for the tip to cool down, this causes the measurement spikes indicated in figure 5.1b. After all the measurements were made, the tip retracts back to the starting position. The temperature would increase back to the value when the tip is far away from the sample.

The data logger temperature measures the change in temperature between the tip in contact and out of contact. An average of approximately 20 points were taken before the tip snap out and after the tip snap out to the environment, the difference between the two values will be used as the data logger temperature. This is used a reference temperature of heat loss to the environment.

The next discussion is the comparison of the data logger results between in air and in vacuum. Figure 5.2 shows the data logger result of mica with 0.8mA current passing through the probe.

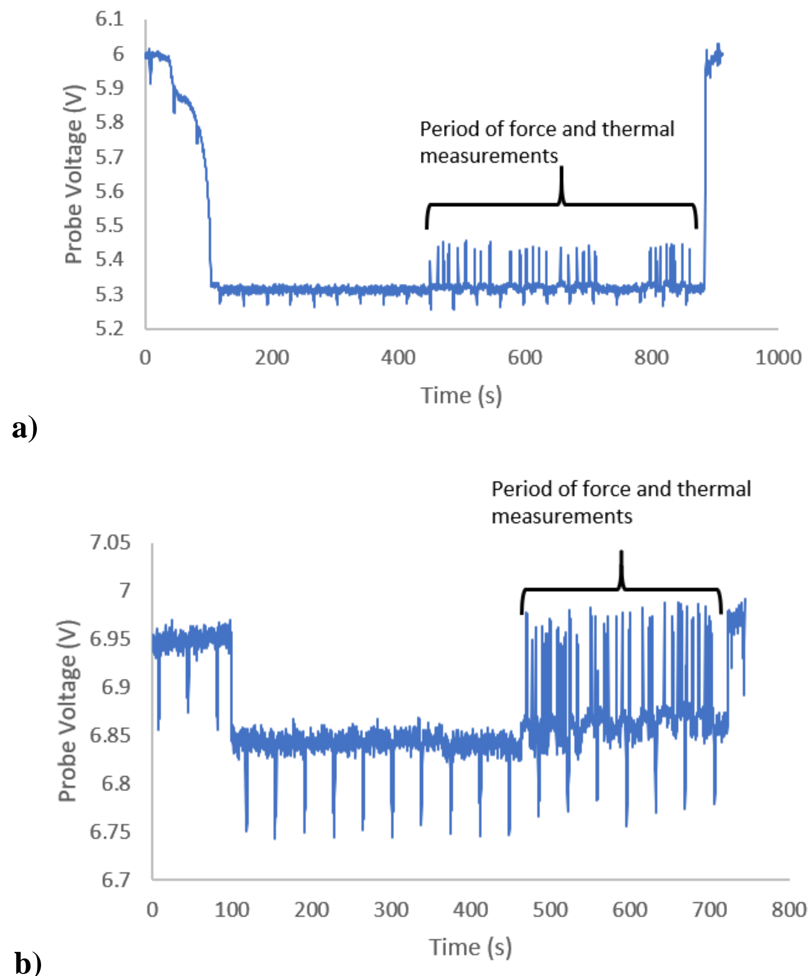

Figure 5.2 Data logger results of mica with 0.8mA in the environment of a) in air and b) in vacuum. The results are comparing the measurement spikes height to the temperature when the tip is not in contact in both environments.

The first characteristic is the change in temperature between the starting point and the contact point, where we see that the overall temperature change in air is much higher than in vacuum. By comparing the change in temperature measured in air and in vacuum, the temperature change in vacuum is only about 10-20% of the temperature change in air, which supports the theory discussed in chapter 2 where the air convection and solid-liquid conduction dominate the thermal transport. The air conduction effect is also observed at the beginning. In figure 5.2a there is a steep drop during manual approach, while in figure 5.2b the steep drop is not obvious.

This is because figure 5.2a the gas conduction is getting more effective when the tip gets closer towards the sample, while in vacuum this effect is eliminated.

From both the data logger results in figure 5.2, the noise spikes showed an approximate 40 second periodic noise, the strength of the noise is approximately at 0.02V in air and 0.1V in vacuum. This noise shows more obviously in vacuum than in air. From figure 5.2 the voltage drop is about 0.7V while it is about 0.1V for in vacuum. Assuming the strength of the noise is constant, the signal to noise ratio for air is larger than in vacuum, hence the noise is more obvious in vacuum as the signal is lower. The source of the noise was not found during the experiment, the possible reason is the internal electric interference caused by the computer. The effect of the noise in temperature measurement will be discussed in the next section. The thermal calibration is set up for measuring the change in temperature, it gives a conversion from the change in voltage to change in temperature, it does not measure the absolute temperature of the sample surface.

In air, the heights of the measurement spikes are significantly smaller compared to the data logger change in temperature due to the heat loss by air. However, in vacuum there are only radiation and solid-solid conduction for thermal transport, the heat loss due to air conduction does not exist. Therefore the temperature does not vary with the tip-sample distance when they are not in contact, hence the probe voltage retracts to its default value between each measurement.

The next discussion is the data logger result of the thermal calibration. The data logger collected the temperature of the Peltier and the tip current, the Peltier temperature was detected by a PT100 thermometer. The data logger result plots the probe current and the Peltier temperature against time. Figures 5.3 shows the data logger results during the calibration.

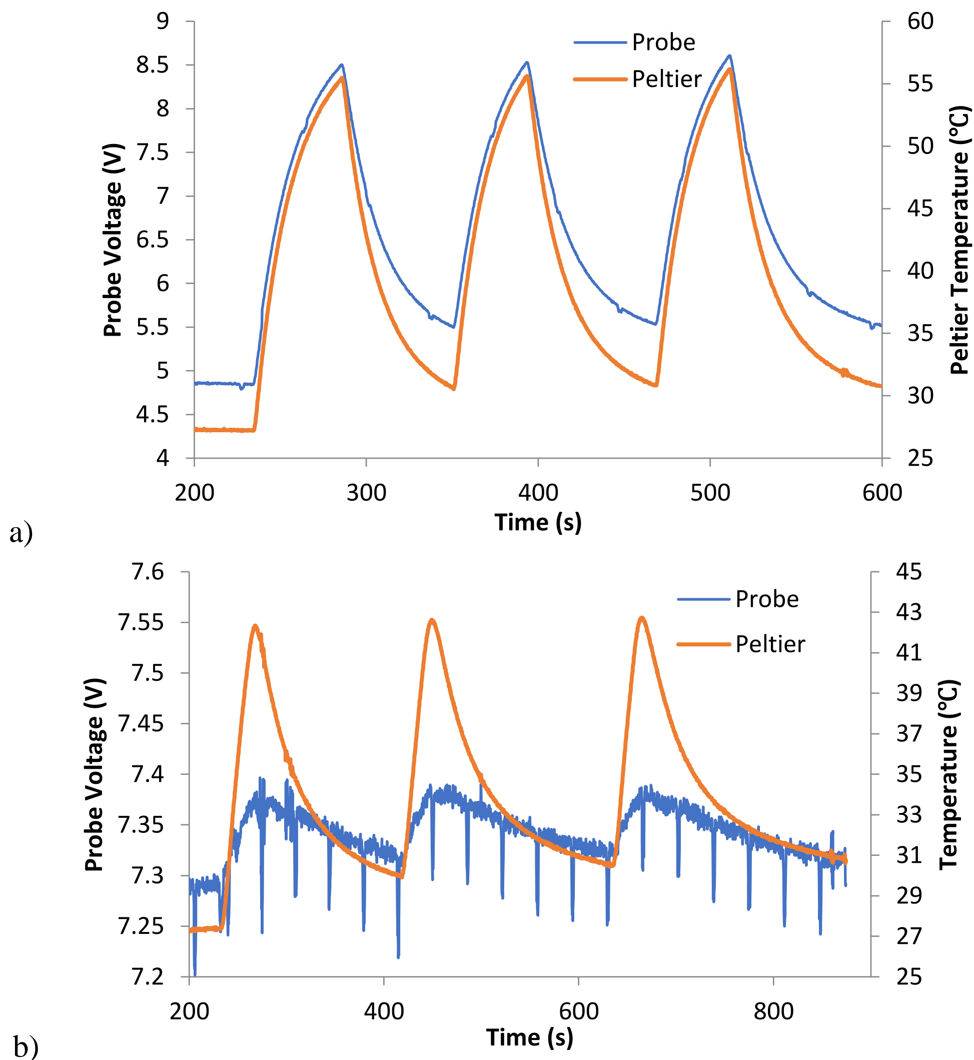

Figure 5.3 The data logger results of thermal calibration with the probe current of 0.8mA a) in air and b) in vacuum.

The graph shows the tip current and the Peltier temperature, both plotted against time. The calibration assumes the change in tip voltage and the change in Peltier temperature are linearly proportional. The probe current will be plotted against the Peltier temperature which will be used for converting voltage to temperature. Figure 5.4 illustrates the difference between the two currents in the calibration.

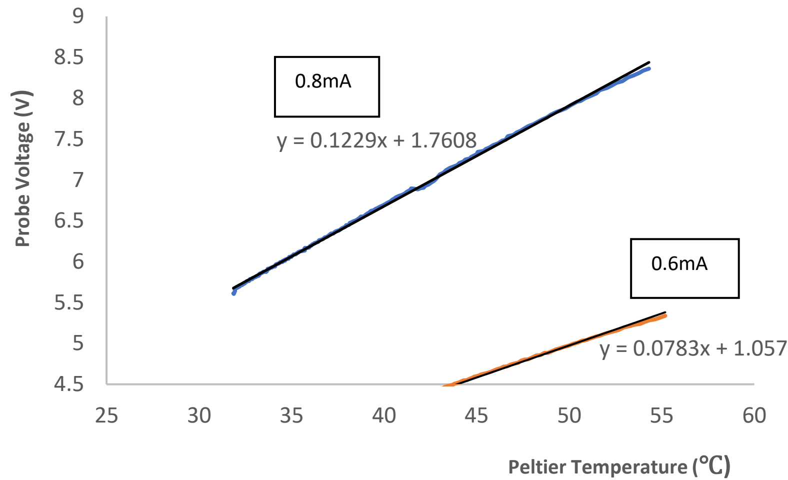

a)

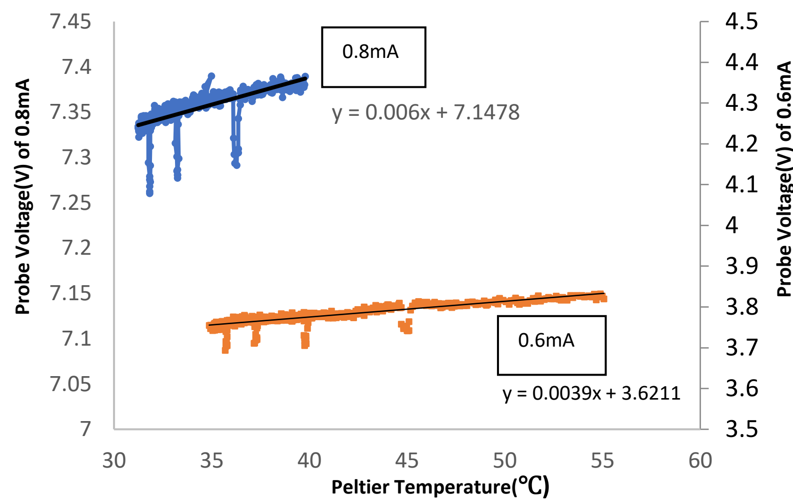

b)

Figure 5.4 Results of thermal calibration, graph of probe voltage against Peltier temperature measured in a) air and b) vacuum.

Figures 5.4 shows the graph of probe current against the Peltier temperature in air and vacuum, for each environment, two probe currents were used. The results that used 0.8mA were observed to provide a larger gradient comparing to results that used 0.6mA. There are more challenges in measuring the calibration in vacuum. The thermal transport in vacuum is limited to two paths, so it takes longer for the probe to cool down than in air. The signal to noise ratio is smaller in vacuum, and the temperature varies less than in air.

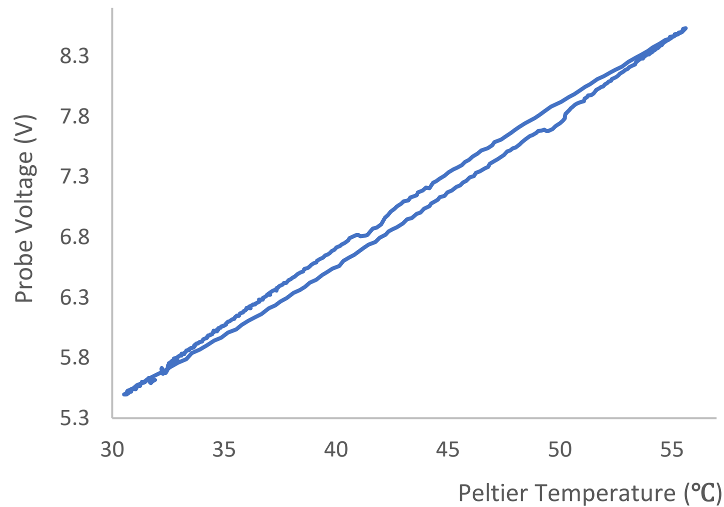

Figure 5.5 A graph of thermal calibration peak with both heating and cooling.

A hysteresis is observed in both air and vacuum environment, figure 5.5 shows this in air. The opening of the loop shows a lag in temperature between the tip and the Peltier heater, caused by the time delay on the temperature changes from the sample to the tip. Recalling figure 3.6 of the specimen photograph, the tip is measuring the calibration at the reserved space, which took about half of the specimen size. Since the tip head is at a much smaller scale, there is a significant distance on the specimen for the heat to transfer towards the thermometer, which causes the hysteresis in the calibration.

When estimating the conversion gradient, the line of best fit for both heating and cooling curves were fitted. In table 5.1 where the results are presented, only the cooling range was chosen for the conversion. During the thermal measurement, the tip will be cooled down when it is in contact with the sample, with this reason the cooling range of the calibration curve is better for the behaviour of the tip.

Probe	Coefficient of conversion (V/℃)	%error	Operating Current (mA)	Environment	Pressure
A	0.079±0.0004	0.24	0.6	In air	atmospheric
B	0.0038±0.0003	0.81	0.6	In vacuum	2.0×10^{-4}mbar
C	0.124±0.0003	0.30	0.8	In air	atmospheric
	0.0059±0.0002	0.92	0.8	In vacuum	1.7×10^{-4} mbar

Table 5.1 Table of the conversion coefficient of the thermal probes used in thermal measurements.

The calibration measurement is presented in table 5.1, including the thermal calibration of 3 thermal probes with different current passing through and in different environment. The coefficient of conversion is the average gradient of the 3 repeated peaks measured in the calibration and the error is estimated as the standard deviation of the repeated value. The pressure for when the calibration measured in vacuum is also noted in the table.

For thermal probe B, the probe was heated to 60 degrees and allowed to cool down naturally with the current at 0.6mA. There was a thermal jump observed in this measurements, the method was showed in chapter 3. The method used in thermal probe C was optimised based on the result of thermal probe B. The result for thermal probe C presented in Table 5.1 is using the 40-degree method, where the probe was heated to 40 ℃ and cooled down naturally.

The author used the air calibration coefficient for converting both vacuum and air thermal measurements. The tip temperature was assumed to be the same as the sample in air, however this assumption does not hold in vacuum. As a result, the calibration coefficient in vacuum is extremely low and the change in temperature signal in vacuum is smaller than in air. From table 5.1, the thermal calibration gradient measured for vacuum is significantly smaller than that measured in air. For example, for probe C, the air coefficient is 0.12 V/℃, this is about 20 times larger than the coefficient measured in vacuum. The vacuum change in temperature voltage signal is small because of the lack of heat paths, when the extremely low calibration

coefficient is used to convert to temperature, it would result in an overestimation of the sample temperature change. Therefore, in the following chapters, the thermal measurement units are converted using only the air calibration respects to the probe.

5.2 Thermal map and the thermal measurements

This section will present the thermal measurement results for each sample measured in air and vacuum. The section will start with the discussion on the characteristics of the thermal maps and the thermal curve. The results will then be presented, starting with presenting the results in air, then move onto vacuum.

The thermal map was generated by feeding the thermal signal into the force section of the feedback module as shown in figure 3.4. The processing software WSxM registered the signal as a standard force signal and automatically programmed the conversion into picometer. The conversion from picometer to volts is noted and will be provided along with all the thermal maps in this project.

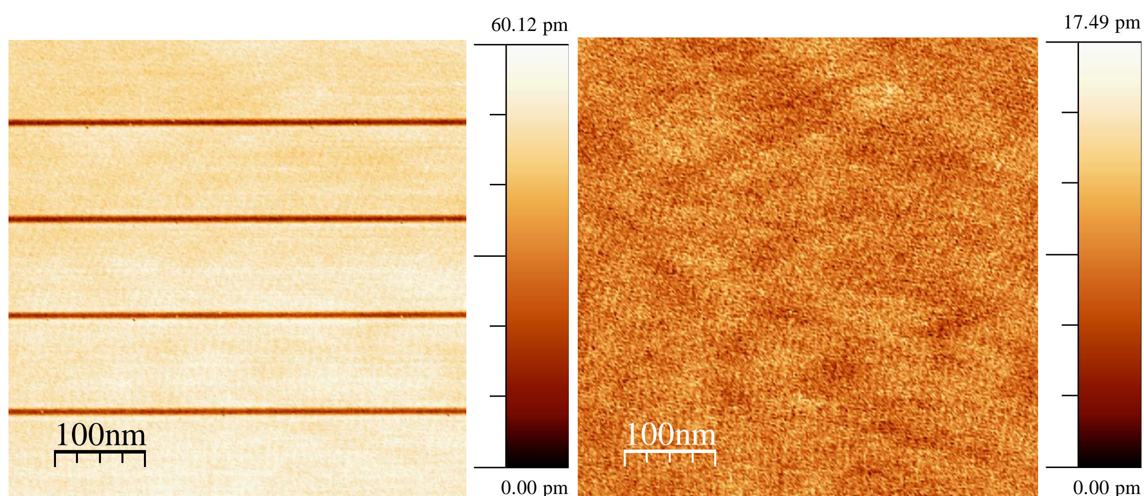

Figure 5.6 a) The unprocessed thermal map of SiC in air b) the processed thermal map of SiC in air. For both figures the conversion 10.02pm/V.

In the chapter 5.1, when introducing the 40 second noise from the data logger, it was shown that there were temperature spikes with a period of approximately 40 seconds. This noise affects the thermal map that is collected during the topography measurements. In figure 5.6a, the dark lines in the thermal map are the periodic noise from the instrument. Various possible origins of this noise were investigated including the tip and the connection between data logger and the SThM, however the source was not identified. After the change of tips, the noise still

appeared in all the results. The noise was removed in the WSxM software, the flatten process in the software was used to eliminate the line of noise and the contrast of the image was adjusted. The temperature measurements were made away from these areas.

In the following presentations, the thermal maps were processed in the WSxM software, figure 5.6b) shows an example of the thermal map after repairing in WSxM. The scale bar of the thermal maps will be presented in pm, along with a conversion from pm to V given by the WSxM software. The thermal measurements are designed to measure the change in temperature, the thermal calibration presented only allows the conversion of the change in tip voltage V to the change in temperature °C. The scale bar effectively shows the total change in temperature °C of the thermal map, however, this total change in temperature is different from the data logger temperature change. The reason is the probe current is calibrated before the experiment, the voltage across the tip is offset from the real voltage, therefore the temperature results of the thermal map and the data logger are not comparable.

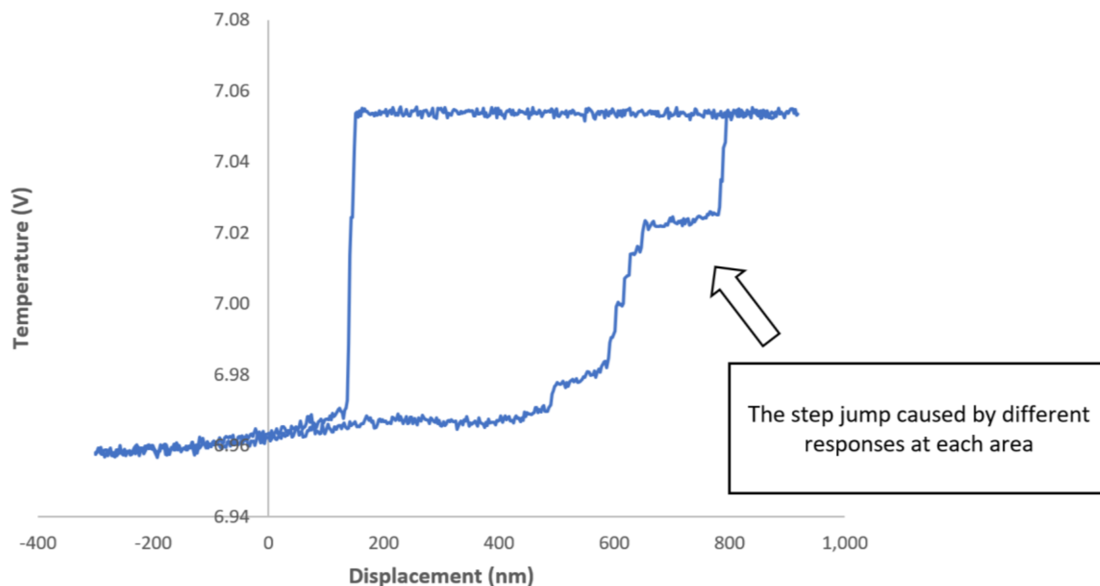

Figure 5.7 Thermal curve of PTFE measured in vacuum. The thermal curve presented is an average of 9 curves. The step jump is caused by different responses at each area.

The thermal curves presented are an average of all 9 curves measured on each sample. The step jump noted in figure 5.7 is caused by the different response between each area on the same sample. Figure 5.8 is showing the individual curve of each area.

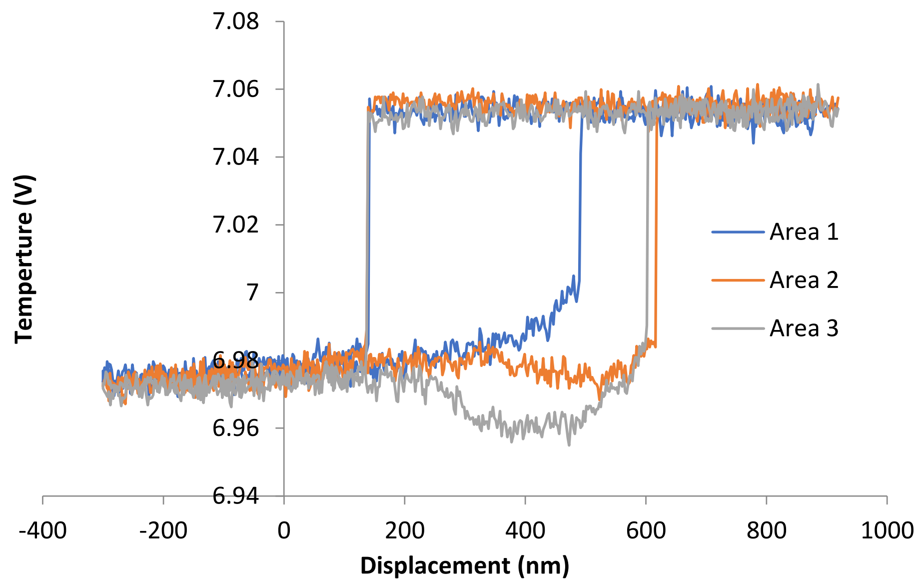

Figure 5.8 Thermal curve of PTFE at 3 different areas measured in vacuum.

The reason causing the step jump in figure 5.7 is the curve was averaging the 9 measurements made in all areas, when the tip doesn't snap out from the same point from the sample, this will generate a variation between the areas. This variation is demonstrated in figure 5.8 showing a comparison of the thermal curves measured in three different areas. This happens more often for a soft material such as PTFE, this is because the tip deforms the material surface and can affect the adhesive force. The approach temperature will be used to compare the samples in this section and with thermal conductivity in section 5.3.

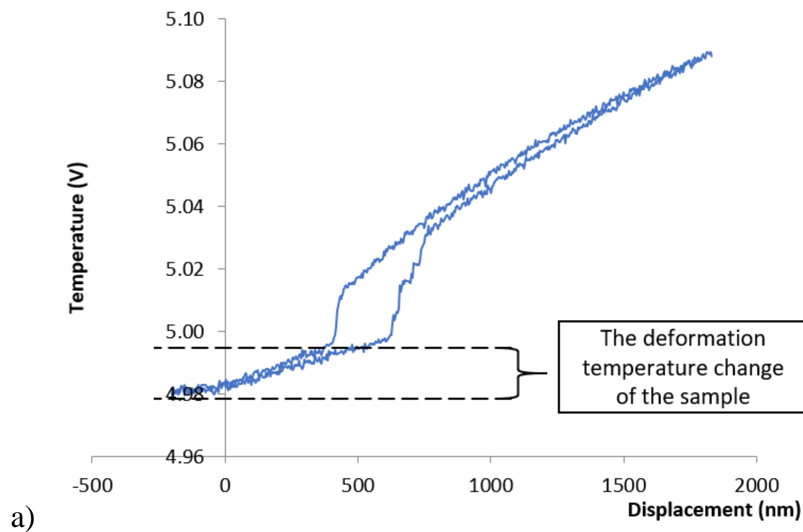

a)

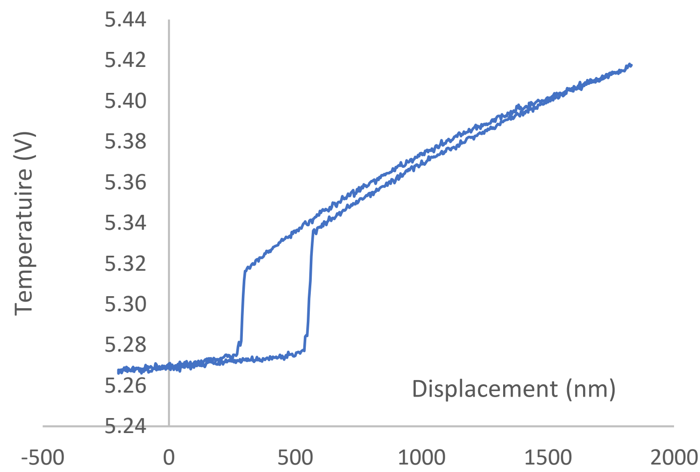

b)

Figure 5.9 The thermal curves of a) PTFE and b) SiC measured in air.

The comparison of the thermal curves between materials within the same environment will be discussed in this section. Figure 5.9 shows the comparison of the thermal curve shapes between the PTFE and SiC within the same environment. After the tip is in contact with the material, the soft material showed a further decrease in temperature compared to the harder material, this is marked in figure 5.9a. This is because after the tip is in contact, the SThM will keep approaching until it reaches the pre-set distance. Since the tip is harder than the PTFE, the tip will deform the PTFE surface and create more contact area for the heat to transport, hence the further drop with temperature.

The next section will present the thermal results measured with the probe current of 0.8mA as the tips were broken during the measurements using 0.6mA resulting in a change of tip. The results between the two probes cannot be directly compared without taking into account the difference of the tip. For example, the tip contact area could be different, which adds another systematic error. However, the 0.6mA results can still be compared within the set.

The order of presenting each material is the same as the topography results in the previous chapter. The presentation of figures 5.10 to 5.14 will come in the following sequence from the left: topography marked with the points where thermal measurements were made, the thermal image on the right that is along with the topography and then an average thermal curve of the thermal measurements at the bottom with the corresponding force curve. The thermal curve is obtained by averaging the curves measured at 3 areas, and at each area the curve is repeated 3 times. The resulting curve shows the average of total 9 curves from one sample. The conversion values are presented at the bottom of the figures.

At the end of the graphical presentation of the thermal maps, a table of the thermal measurement results will be presented for each environment. The table will include the approach, retract and the data logger change in temperatures.

A general discussion on the values within the environment will be discussed with the table. At the end of the chapter, both numerical results will be combined and compared with further discussion. The interpretation and further analysis of the data will be presented in chapter 5.4

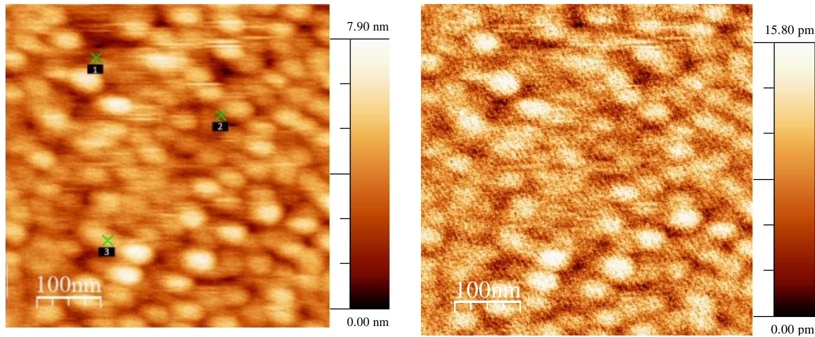

Thermal map scale bar conversions

pm to V: 38.3 pm/V

pm to °C: 4.73 pm/°C

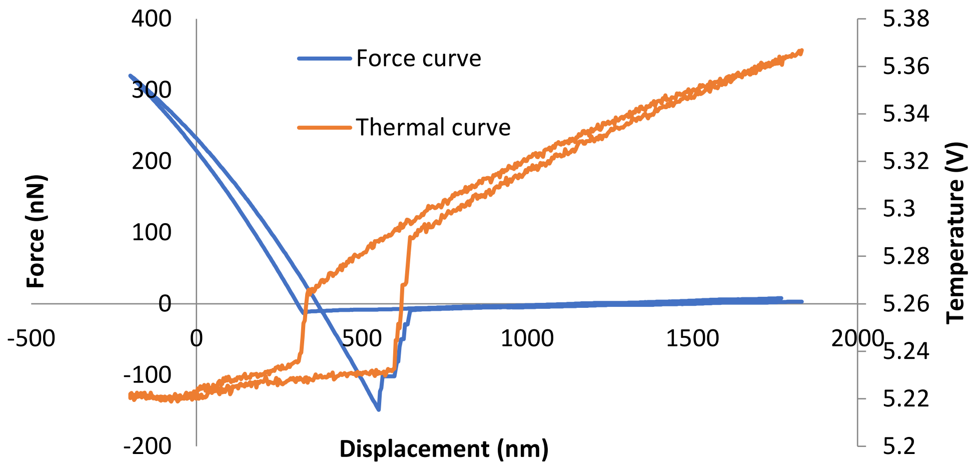

Figure 5.10 The results for gold thin film in air.

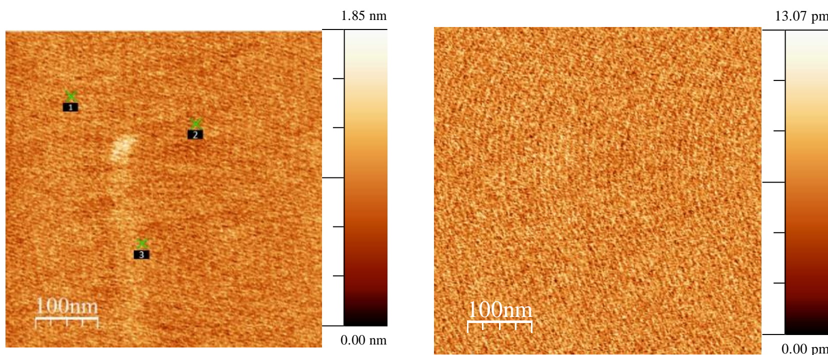

Thermal map scale bar conversions

pm to V: 8.85 pm/V

pm to °C: 1.09 pm/°C

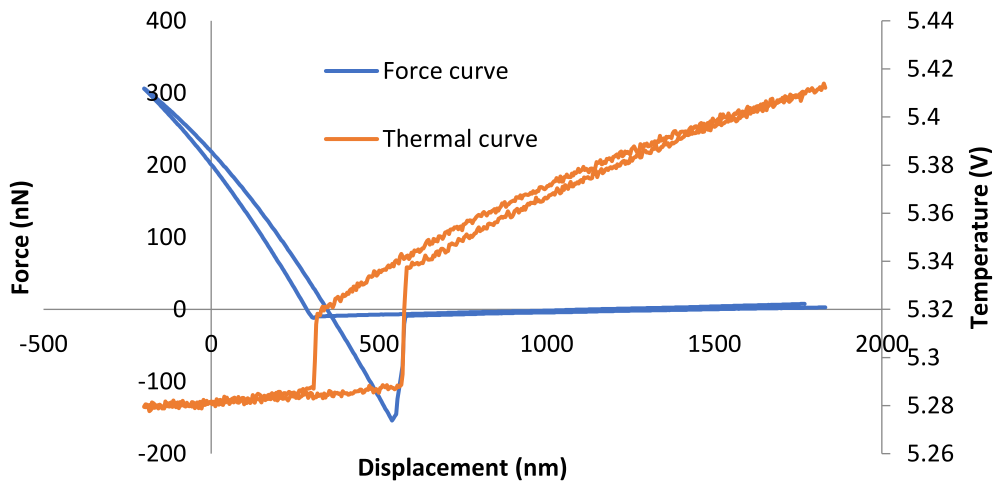

Figure 5.11 Thermal results of Mica in air.

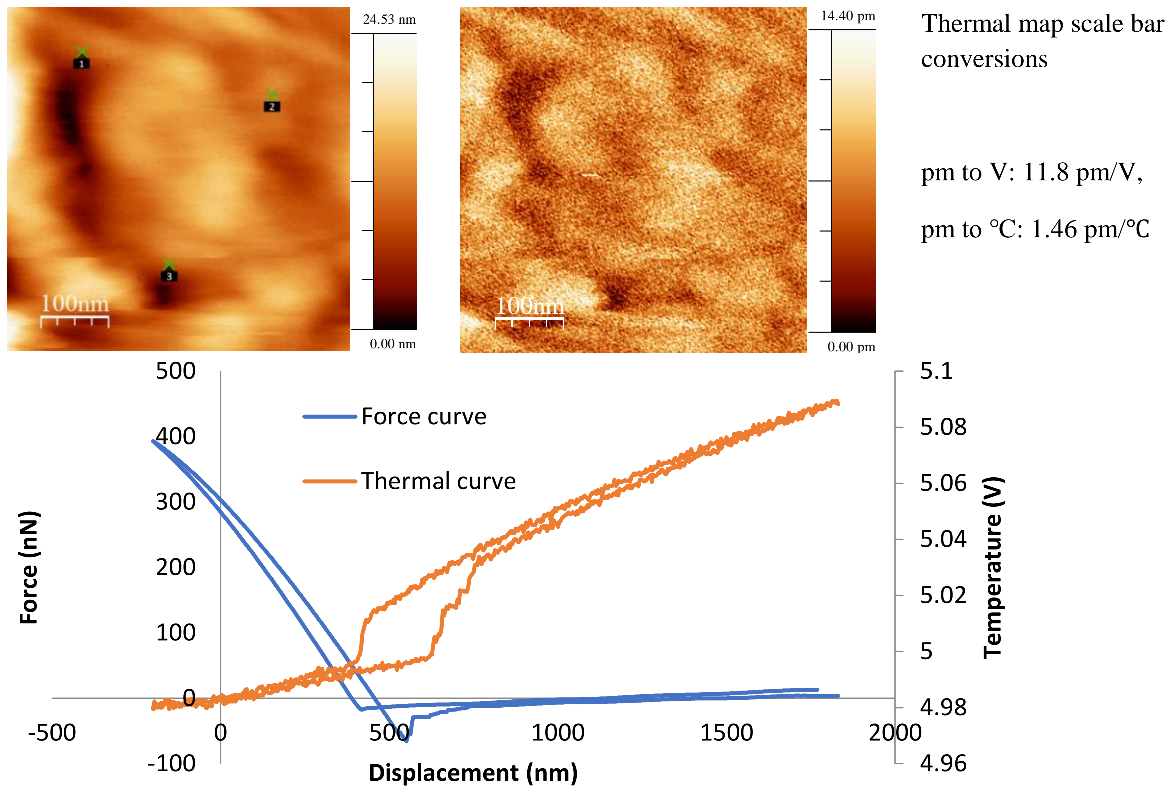

Figure 5.12 Thermal results of PTFE in air.

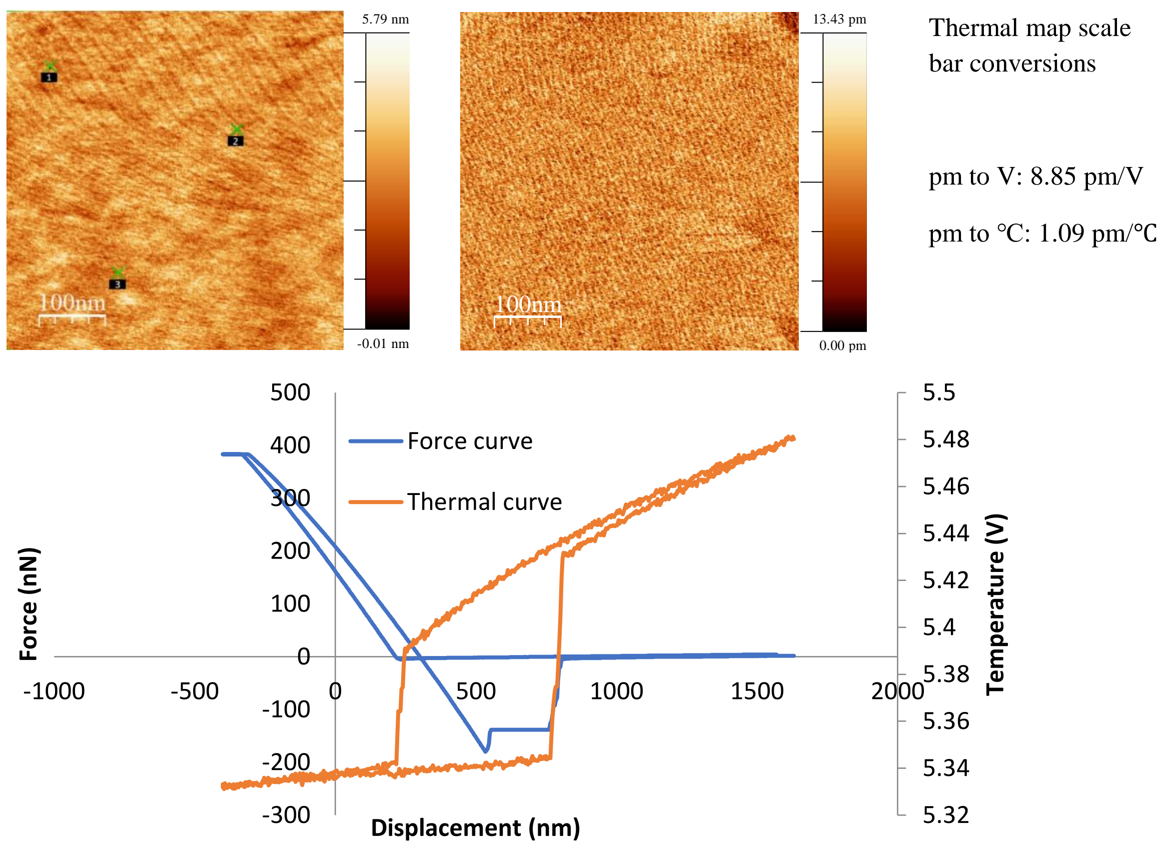

Figure 5.13 Thermal results of Silicon in air.

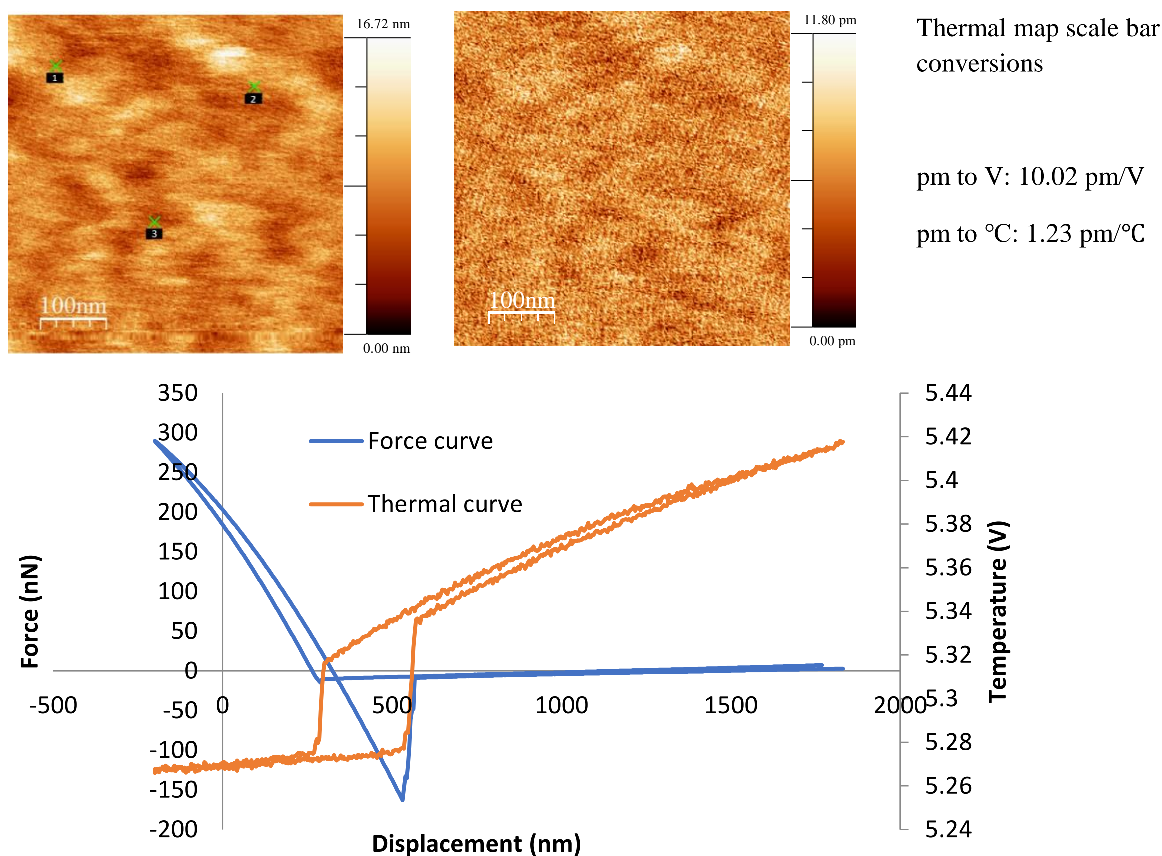

Figure 5.14 The results of silicon carbide in air.

The first discussion would be the comparison of the thermal map and the thermal curves. The first result presented was the thin film gold, the sample with an unknown thermal conductivity. The hardness of the material was expected to be softer than Silicon but harder than mica because of the bulk elastic modulus value of gold. The topography shows that there are some surface features. The thermal curve shows that there is a slight deformation after the tip contacts with Au as the temperature dropped after the tip is in contact.

In the previous chapter, the mica did not show any features on the topography, the thermal map supports this observation by having a low contrast image. The thermal map is picking up a strong interference signal and the surface structure did not show on the thermal image. The possible reason is the effect of the mica surface features were smaller than the interference signal, so only the interference was measured. The thermal curve shows some temperature drop after the contact point.

The PTFE showed some features on the topography. The thermal curve shows that there is a clear gradient drop after the tip approached the surface as described earlier in this section. The thermal curve in figure 5.12 shows the step change at the retract temperature path that was described in figure 5.7. This is due to the soft surface of PTFE that causes different responses between each area.

The thermal image of silicon is similar to mica, a strong interference signal was collected and affects the clarity of the thermal map. Although the silicon thermal image showed some surface features, the noise signal is very similar to mica. The thermal curve shows a clear change in temperature for approach and retract.

Silicon carbide is the hardest material in the sample set, the topography and thermal map both collected the interference signal. Some features on the topography can be seen on the thermal map. The change in temperature was expected to be the largest due to the highest thermal conductivity from the set, however the temperature change is smaller than Si.

Table 5.2 presents the change in temperature measured in air. The table is arranged with a descending order of thermal conductivity. The thin film gold was arranged at the bottom of the table because it is the sample with unknown thermal conductivity.

Environment	Material	Thermal Conductivity (W/m·K)	dT (approach) (℃)	%error	dT (retract) (℃)	%error	dT Data logger (℃)	%error
In Air with atmospheric pressure	SiC	420	0.35±0.01	2.6	0.48±0.05	1.0	5.80±0.07	1.2
	Si	124	0.388±0.004	0.9	0.69±0.01	1.1	5.68±0.08	1.4
	Mica	0.53	0.26±0.01	3.7	0.41±0.01	2.4	5.51±0.08	1.3
	PTFE	0.2	0.14±0.02	11	0.23±0.01	3.3	4.43±0.09	1.9
	Au	314(bulk)	0.24±0.02	6.8	0.44±0.02	4.5	5.90±0.08	1.3

Table 5.2 Table of temperature measurements from the thermal probe in air, with a current of 0.8mA.

The first observation is comparing the numerical results from the different parts of the measurement to verify the characteristics of the thermal measurements as discussed in chapter 2. The change in temperature recorded by the data logger is higher than the retract or the approach value in air. This is because the tip was approaching from far away and heated. As the distance between the sample and the tip gets closer, the air conduction and convection effect will increase and the tip will cool down. The approach temperature values are smaller than the retract temperature in general, this is because the air conduction dominated the temperature measurements, as described in chapter 2. When comparing the retract and approach value, the approach value is more important for interpretation with the thermal conductivity. The reason is that there is no extra force such as the adhesive force measured in the previous chapter to affect the contact with the sample.

The approach temperature for all samples showed three different categories of temperature change, the silicon and silicon carbide at the highest end of the temperature table; the mica and thin film gold at the middle; and the PTFE being the lowest of the table. When comparing the three categories with the thermal conductivity, the first observation is the sample with larger

change in temperature would have higher thermal conductivity. The PTFE has the lowest thermal conductivity and change in temperature.

The silicon has a higher value of approach temperature than the silicon carbide. The error for silicon is small, which indicates that the results are consistent. Recalling the results from chapter 4, the silicon also has the largest adhesive force value, however the adhesive force measurements only affect the retract temperature. The possible explanation for this is whether the silicon carbide change in temperature was lower than expected, or the silicon value being higher than expected.

Comparing the mica result to silicon carbide and silicon, the approach temperature of mica was consistently significantly lower than silicon carbide. The explanation follows the same argument of thermal conductivity of the materials. This indicates that the silicon is showing a higher value than expected.

The thin film gold approach temperature is observed to be smaller than mica. The thermal conductivity of thin film gold was expected to be similar to bulk gold material. However, the observation indicated the thin film gold had as similar value of thermal conductivity to mica.

Figure 5.15 to 5.19 will continue presenting the graphical measurements for each sample, the results were measured in vacuum. The presentation of the figures will continue with the previous sequence. The vacuum pressure was measured at 1.7×10^{-4} mbar and the probe current was the same at 0.8mA. Table 5.3 summarises the change in temperature and the comparison will be discussed after the graphical results in table 5.4.

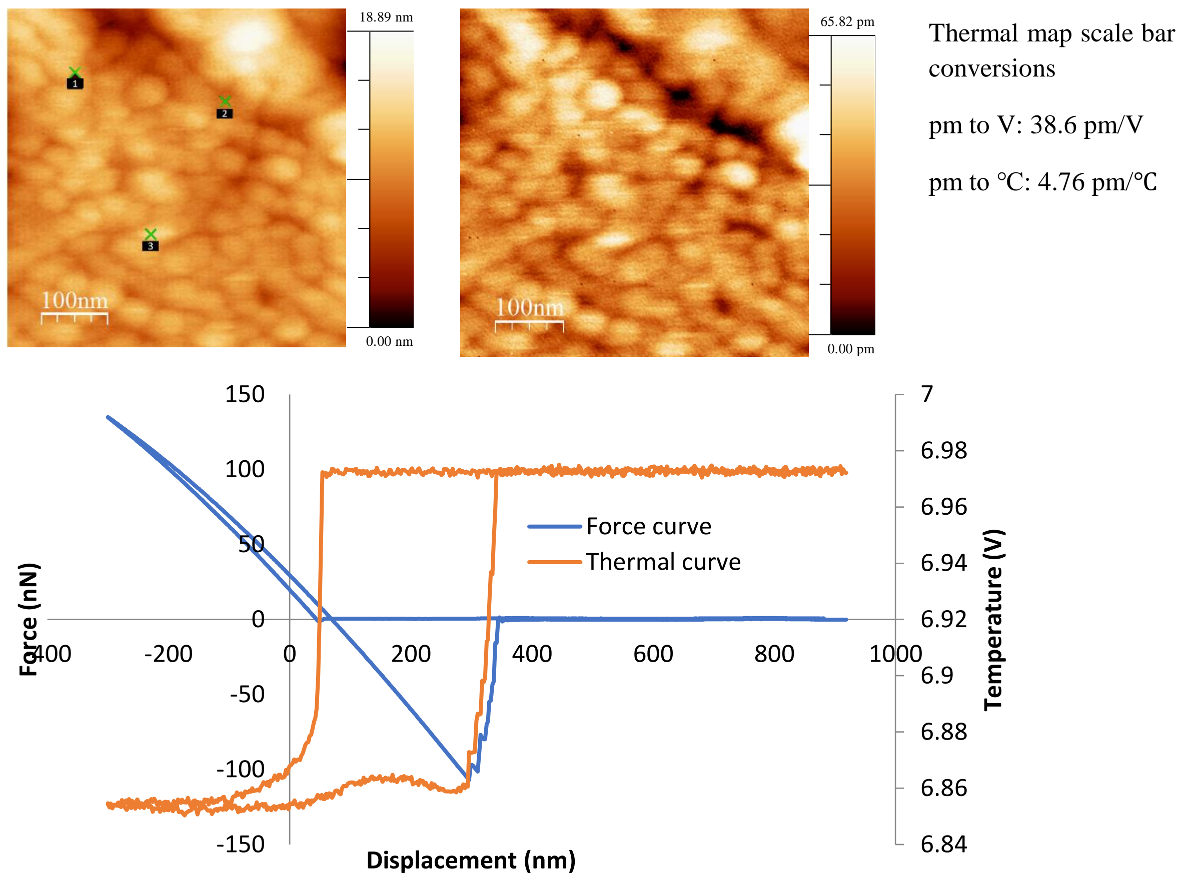

Figure 5.15 Thermal results of thin film gold in vacuum.

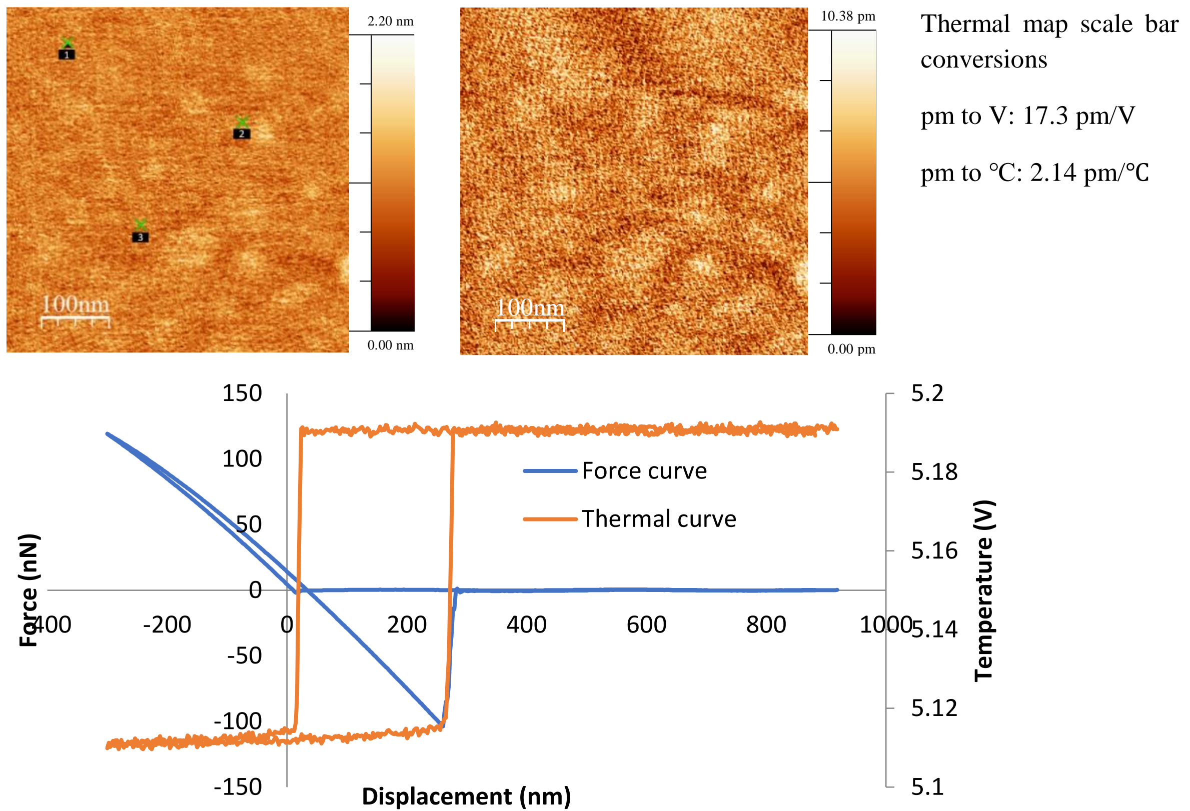

Figure 5.16 Thermal results of Mica in vacuum.

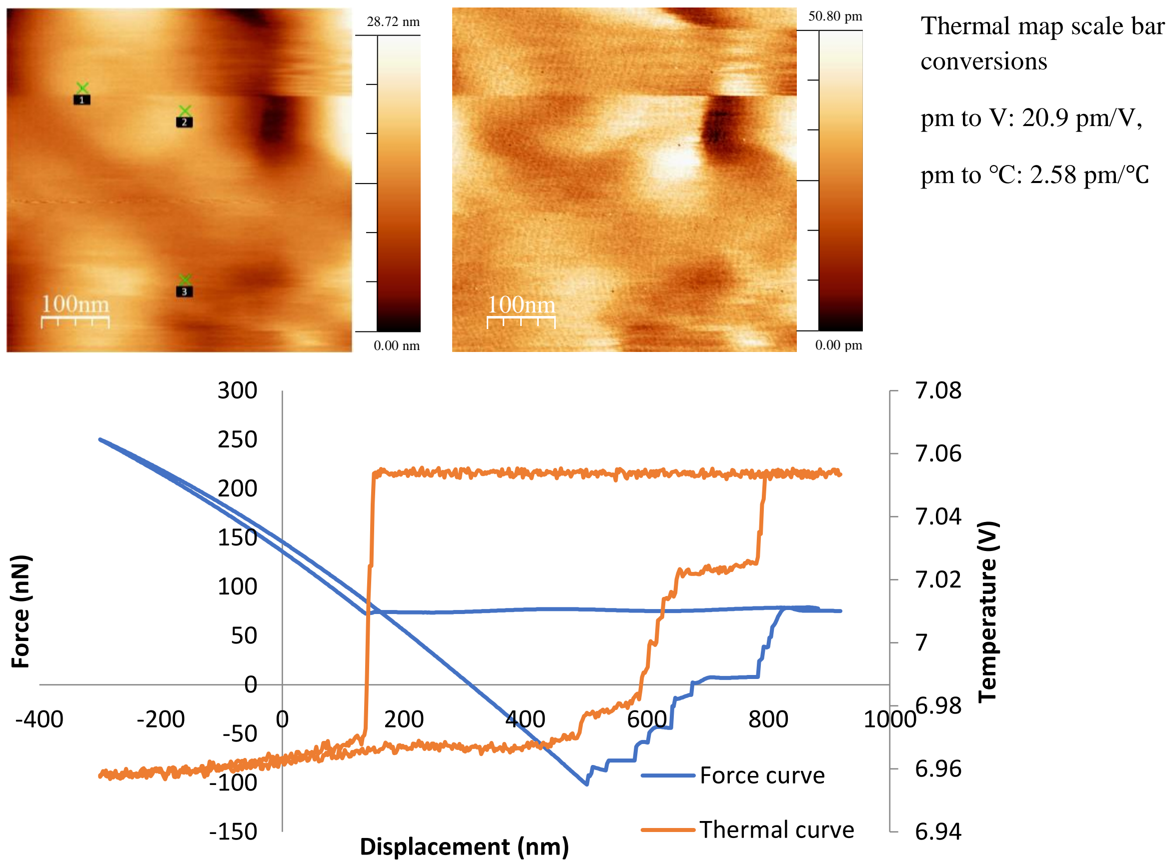

Figure 5.17 Thermal results of PTFE in vacuum.

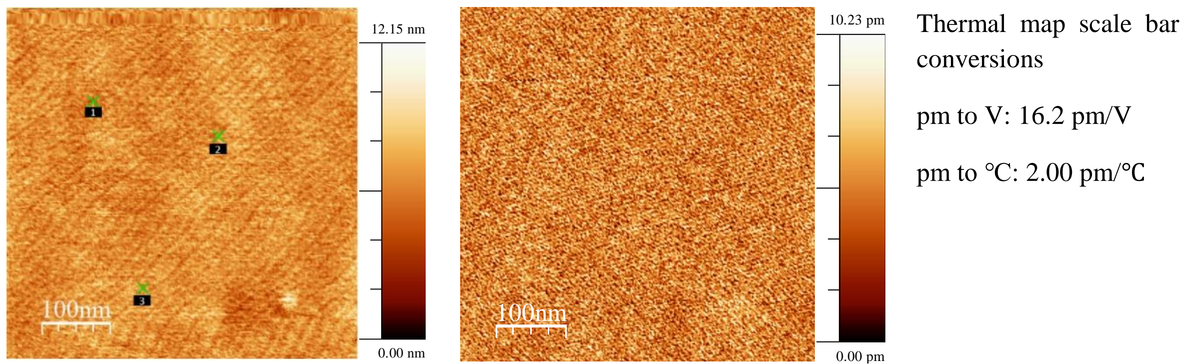

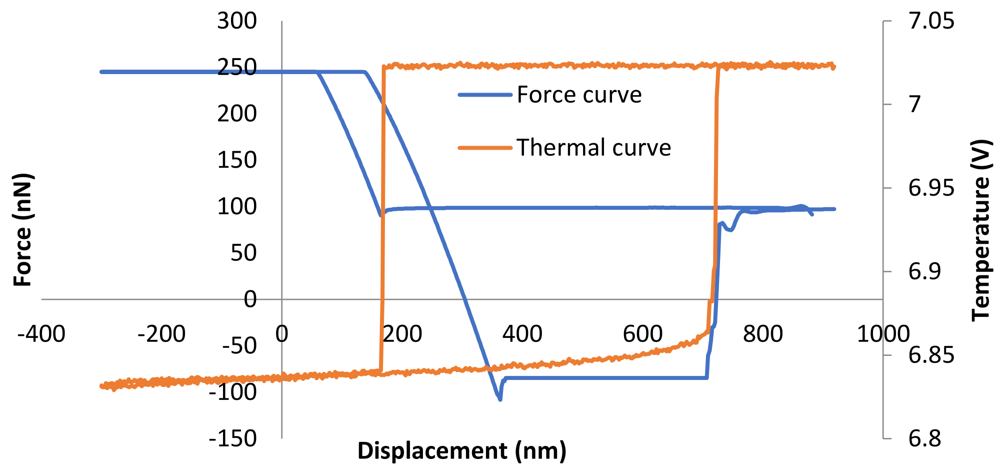

Figure 5.18 Thermal results of silicon in vacuum.

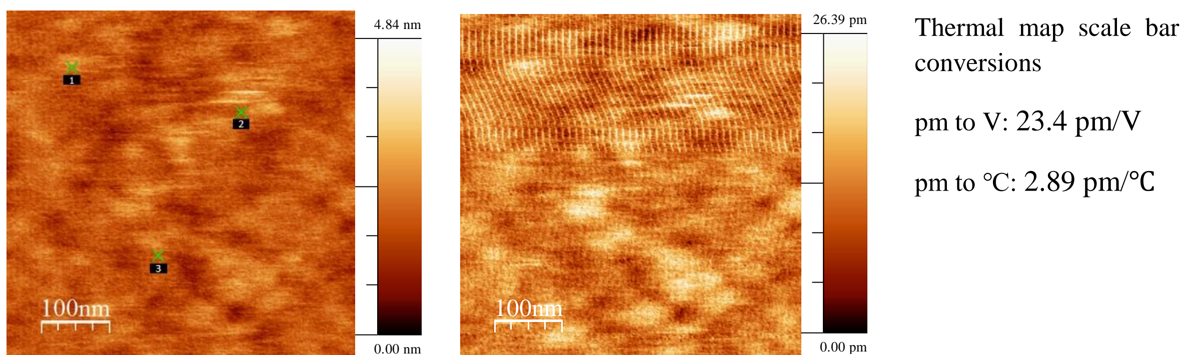

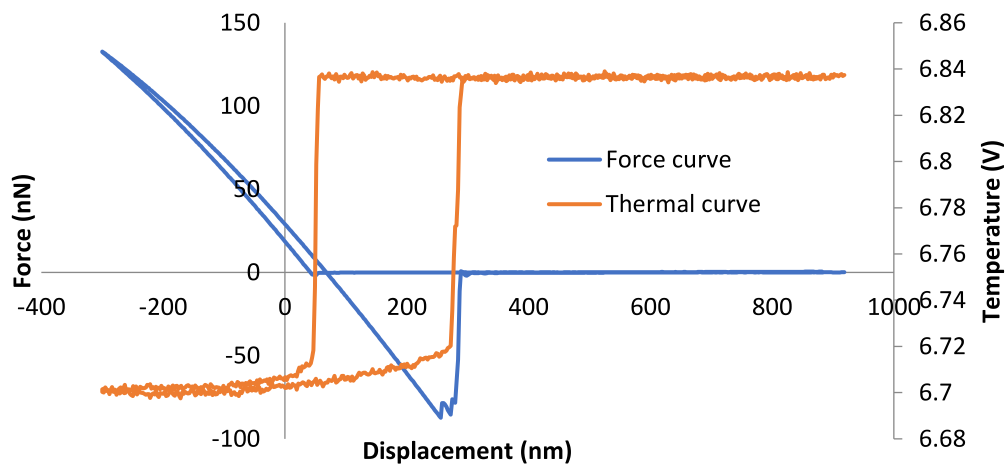

Figure 5.19 Thermal results of silicon carbide in vacuum.

The thin film gold showed some patterned island features on the topography, this is consistent with the results in air. Although the thin film gold does not have a dedicated fabrication pattern, the topography shows the surface structural difference between the thin film sample and bulk samples. There is a small temperature variation before the tip snaps out the surface, this is consistently showing in all 9 points measured on the gold sample. The reason for this is not known and it has not been investigated.

For mica, the topography result has shown a clearer result in air. The interference noise was not significant enough to interfere the surface features on the topography results. A clear change in temperature is shown in the thermal curve and is synchronised with the force curve.

The topography of PTFE showed the same feature characteristic as the result in air. The thermal curve shows more clearly the variation between areas, the step jump at the retract area was noted and discussed in the earlier of this section.

The topography of silicon in vacuum has the same characteristic as measured in air, the thermal map showed the strong interference. The thermal curve shows the biggest temperature drop from the sample set measured in vacuum, the force curve verified the position of where the probe snapped in and snapped out. This has the same characteristic as the results from air.

The thermal map of silicon carbide collected the interference at the top of the map. The interference signal was hugely reduced during the measurement. The cause of it is not known. The features on the silicon carbide also showed on the thermal map.

Environment	Material	Thermal Conductivity (W/m·K)	dT (approach) (℃)	%error	dT (retract) (℃)	%error	dT Data logger (℃)	%error
In Vacuum Pressure: 1.7×10^{-4} mbar	SiC	420	1.03±0.01	1.3	0.95±0.02	2.6	1.19±0.02	1.0
	Si	124	1.48±0.01	0.33	1.29±0.01	0.88	1.52±0.03	2.3
	Mica	0.53	0.82±0.01	1.4	0.80±0.01	1.7	0.83±0.03	3.6
	PTFE	0.2	0.68±0.02	2.3	0.58±0.05	9.4	0.90±0.01	1.1
	Au	314(bulk)	0.76±0.04	5.9	0.90±0.03	2.6	1.07±0.03	3.2

Table 5.3 Table of temperature measurements from the thermal probe in vacuum, with a current of 0.8mA.

Table 5.3 shows the vacuum temperature results arranged in the descending order of thermal conductivity. The first observation is that the data logger change in temperature is similar to both the approach and the retract temperature, unlike the big difference observed in air. This is because there was no air conduction in vacuum, the gas cooling dependence on the tip-sample distance is eliminated, hence the variation of the change in temperature is small. With the same reason, the approach and retract values are also similar. The approach temperature in vacuum generally follows the same order of thermal conductivity.

The first comparison is to compare the silicon and silicon carbide approach temperature. The silicon approach temperature is larger than silicon carbide, which is consistent with the results in air. The same occurs with the retract temperature. The error for both samples are small and the results are consistent. The silicon carbide approach temperature is larger than mica, which is consistent with the expected result.

The mica approach temperature follows the same observation as in air, where the change in temperature is larger than gold. When comparing the retract temperature to the approach temperature, both temperature measurements are the same for mica.

The change in temperature for PTFE is the smallest, the result is expected as the PTFE has the smallest thermal conductivity from the sample set. The PTFE has the soft surface and the error is expected to be large. However, from the figure 5.8 the variation of the approach temperature

was not so large. The PTFE error result showed that the retract value has greater percentage error of 9.4% than the approach error of 2.3%.

For the measurements of gold, the temperature value is similar to mica for both approach and retract. The gold approach temperature is smaller than mica in vacuum, however the difference is small. This observation supports the deduction of the gold sharing the similar range of thermal conductivity with mica. However, the error for approach temperature is big, this is because the gold did not show a clear drop on the thermal curve, this causes a large variation when taking the measurements. The gold surface has a high variation across the area that is similar to PTFE described in figure 5.8. This variation is also causing difficulties on making the measurements, hence the 5.9% error on approach value.

Table 5.4 will compare the temperature measurements of each sample in the two environments. The characteristic of each environment was discussed individually in the above section. The conversion coefficient used the measured value in air of 0.12 V/℃.

Environment	Material	Thermal Conductivity (W/m·K)	dT (approach) (℃)	%error	dT (retract) (℃)	%error	dT Data logger (℃)	%error
In Air with atmospheric pressure	SiC	420	0.35±0.01	2.6	0.48±0.05	1.0	5.80±0.07	1.2
	Si	124	0.388±0.004	0.9	0.69±0.01	1.1	5.68±0.08	1.4
	Mica	0.53	0.26±0.01	3.7	0.41±0.01	2.4	5.51±0.08	1.3
	PTFE	0.2	0.140±0.02	11	0.23±0.01	3.3	4.43±0.09	1.9
	Au	314(bulk)	0.24±0.02	6.8	0.44±0.02	4.5	5.90±0.08	1.3
In Vacuum Pressure: 1.7×10^{-4} mbar	SiC	420	1.03±0.01	1.3	0.95±0.02	2.6	1.19±0.02	1.0
	Si	124	1.48±0.01	0.33	1.29±0.01	0.88	1.52±0.03	2.3
	Mica	0.53	0.82±0.01	1.4	0.80±0.01	1.7	0.83±0.03	3.6
	PTFE	0.2	0.68±0.02	2.3	0.58±0.05	9.4	0.90±0.01	1.1
	Au	314(bulk)	0.76±0.04	5.9	0.90±0.03	2.6	1.07±0.03	3.2

Table 5.4 Table of temperature measurements from thermal probe, measured in 0.8mA.

When comparing the numerical results from the different environments, the first observation is the change in data logger temperature is about 5 times larger than in vacuum. The data logger result measures the heat loss from far away of the sample to after the tip approaches. In the air case, when the tip is far away from the sample, the tip loses heat to the air hence the change in temperature is larger in air. In vacuum, the air was eliminated, when the tip is far away from the sample, the tip temperature loss by the thermal radiation is negligible and could not be measured. This can be showed by the change in temperature are similar between approach, retract and the data logger.

The results show that the vacuum change in temperature is generally larger, for both approach or retract. In air, the tip is cooling as it approaches to the sample, when it snaps in, the temperature difference between the tip and the sample has greatly reduced. In vacuum, the

temperature was not cooled by the air conduction, when the tip snaps in, the change in temperature is then larger. Although there is a much smaller contact area in vacuum, the signal is larger.

From both environments, the gold results are similar to mica. In both cases, the approach temperature of gold is larger than mica. The retract temperature and the data logger results are smaller, however, the retract values are less reliable as described in chapter 2. Therefore, judging by the approach temperature, the gold thin film is expected to have similar thermal conductivity to mica.

The error presented in the table is the variation of the measurements taken at all the 9 areas, it was calculated using the standard deviation of the repeated values. The error for retract values was expected to be larger in air than the approach values because the snap out point is not repeatable. However, the variation was not big and the error is similar for both attract and retract.

The error analysis for this section only discusses the numerical error that was able to be measured during the measurements. However, there are more factors that could affect the numerical results. During the experiment in both environments the pressure and the humidity were not controlled, this could affect the amount of water forming on the sample surface. The hysteresis effect described in figure 5.5 was noted as an error when measuring the thermal calibration. This effect was not taken into account when calculating the change in temperature. However, since all of the temperatures were converted through the same calibration coefficient and only the change in temperature was measured, the contribution of this error would be the same for all thermal values.

The thermal calibration was performed before the thermal readings were taken with the samples on the heater during the calibration process. This causes the samples to be heated at a certain temperature and then cooled down while the thermal measurements were being taken. Figure 5.20 presents the data logger result of silicon, which was the first sample being measured in the data set.

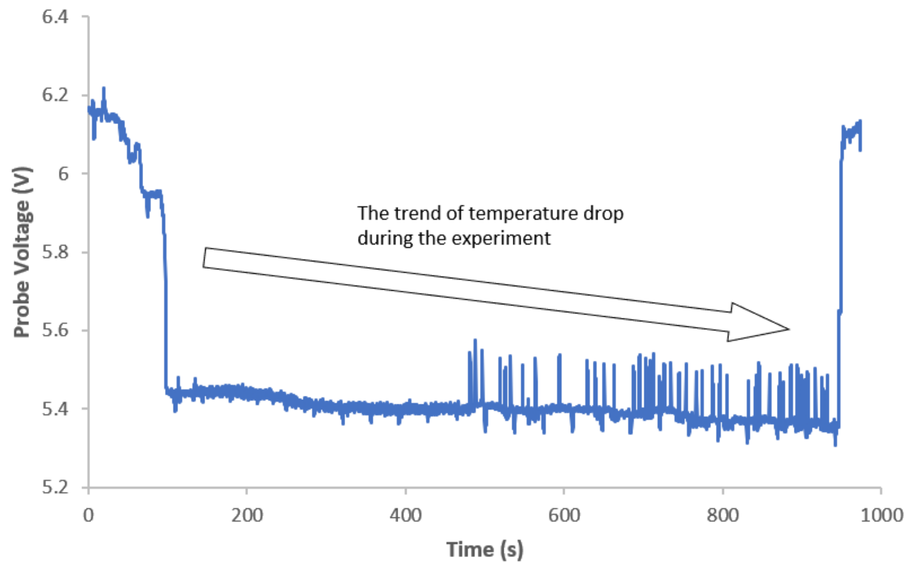

Figure 5.20 The data logger results of silicon in air showing the sample cooling during the experiment.

In figure 5.20, after the tip snapped in, the temperature voltage dropped to about 5.4V and by the end of the experiment, the temperature has dropped to approximately 5.3V. This shows that the sample was cooling during the measurements and might result in dT being smaller than expected. However, as the data presented were collected towards the end of the measurement, the temperature difference was expected to be small.

5.3 Discussion and interpretation of thermal measurements and thermal conductivity

In section 5.2, the graphical results measured in both air and vacuum were presented, the general observations and the comparison were discussed according to the environment. The numerical result of approach, retract and the data logger change in temperature were compared for both environments.

This section will continue the analysis of the thermal data, the analysis will discuss the interpretation of the physics from the results of both chapters 4 and 5 as presented in the summary table 5.5.

Environment	Material	Thermal Conductivity (W/m·K)	Elastic modulus (GPa)	dF(retract) (nN)	dT (approach) (℃)	dT (retract) (℃)	dT Data logger (℃)	Deformation (℃)	Deformation to dT(approach) %	Percentage heat loss (%)
In Air with atmospheric pressure	SiC	420	302	175±1.96	0.35±0.01	0.48±0.05	5.80±0.07	0.107±0.001	31	94
	Si	124	179	179±1.6	0.388±0.004	0.69±0.01	5.68±0.08	0.119±0.001	31	93
	Mica	0.53	170	165±0.3	0.26±0.01	0.41±0.01	5.51±0.08	0.103±0.002	39	95
	PTFE	0.2	0.4	77±1.1	0.140±0.02	0.23±0.01	4.43±0.09	0.166±0.003	119	96
	Au	314(bulk)	79(bulk)	144±0.54	0.24±0.02	0.44±0.02	5.90±0.08	0.180±0.005	75	97
In Vacuum Pressure: 1.7×10^{-4} mbar	SiC	420	302	133±5.2	1.03±0.013	0.95±0.02	1.19±0.02	0.139±0.003	13	13
	Si	124	179	153±5.8	1.48±0.005	1.29±0.01	1.52±0.03	0.118±0.001	7.9	2.7
	Mica	0.53	170	144±3.2	0.82±0.012	0.80±0.01	0.83±0.03	0.090±0.001	11	1.1
	PTFE	0.2	0.4	160±3.9	0.68±0.015	0.58±0.05	0.90±0.01	0.157±0.003	23	9.8
	Au	314(bulk)	79(bulk)	145±9.7	0.76±0.04	0.90±0.03	1.07±0.03	0.299±0.009	39	24

Table 5.5. A summary table for overall the data. The table showed the material, the thermal conductivity, the elastic modulus, the retract force, the change in temperature for approach, retract and for the data logger. The new elements are the deformation column, where measuring the temperature dropped after the tip deforms the sample. The percentage heat loss is calculating the percentage ratio of approach to data logger.

The table 5.5 summarised the results in section 5.2, the extra columns are attempts to analyse the change in temperature with surface hardness, the deformation temperature, and with the environment the percentage heat loss.

The first discussion will be the deformation temperature. The deformation temperature is the temperature change detected while the tip is in contact with the samples. The deformation is taking the difference of V_{min} used for measuring the approach temperature and the V_{deform} at the contact region. The difference of this value was divided by the approach temperature and converted to a percentage. The range of values are illustrated in figure 5.21.

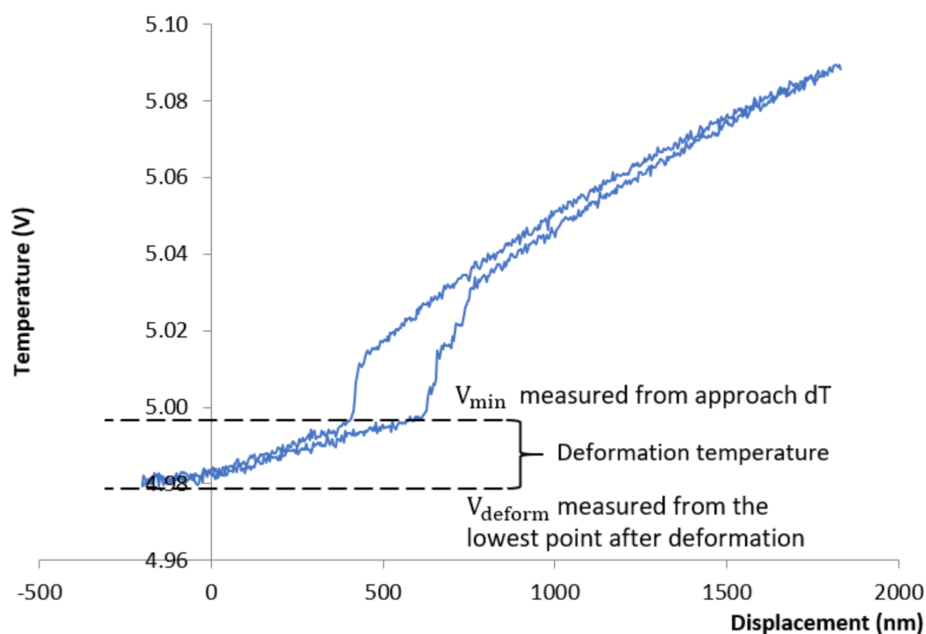

Figure 5.21 Result of PTFE illustrating the method of calculating deformation temperature changes.

For the soft samples, the deformation temperature is expected to be larger than hard materials. This is because when the tip is in contact with the sample, the tip is pushing towards the sample surface, which for soft materials would increase the contact area for mechanical conduction and solid liquid conduction. However, the tip might also deform while in contact with a hard material.

In the air result, the deformation for PTFE is significantly larger than other samples. The harder materials such as silicon and silicon carbide are similar with 31%. The thin film gold showed a high percentage deformation of 75%. In vacuum, the samples showed a different trend with air. The gold was observed have a larger deformation temperature than PTFE. The possible explanation is in vacuum, the elimination of gas conduction and solid liquid conduction affected the trend observed in air. Since the thermal conduction is depending on the thermal conductivity of the material and the gold was expected to have a higher thermal conductivity than PTFE, the deformation results are then explained. The tip deformation of gold provides evidence that the gold thin film is a soft material.

The next discussion will be the percentage heat loss, this calculation is an attempt to find out the amount of heat loss due to the environment. For the calculation, the data logger change in temperature was used to be the overall temperature change. The approach temperature was used as the heat transported between the tip and the sample, also the approach temperature is more reproducible. The heat loss by the environment is calculated by the difference between the data logger temperature and approach temperature, then converted into percentage of the data logger value. From the result in air, the percentage heat loss is generally above 90%. In vacuum, the heat loss is expected to be lower than in air, the average heat loss from the data is approximately 10%.

The following part will present the thermal measurements against the thermal conductivity and discuss the method to determine the unknown conductivity of a sample. Throughout the chapter 4 and 5, the properties of gold thin film were not known. From both force and thermal results, there is evidence that the gold thin film would have a similar hardness and thermal conductivity with mica, this is shown by similarity of the two sample values measured in the previous sections.

In order to determine the thermal conductivity of gold, the relationship between the approach temperature and the sample thermal conductivity would first need to be investigated. The approach temperature measurements are the important values used to determine the relationship with the thermal conductivity. The reason is the approach temperature has a consistent snap in point that is reproducible. The approach temperature is plotted against the thermal conductivity in figure 5.22.

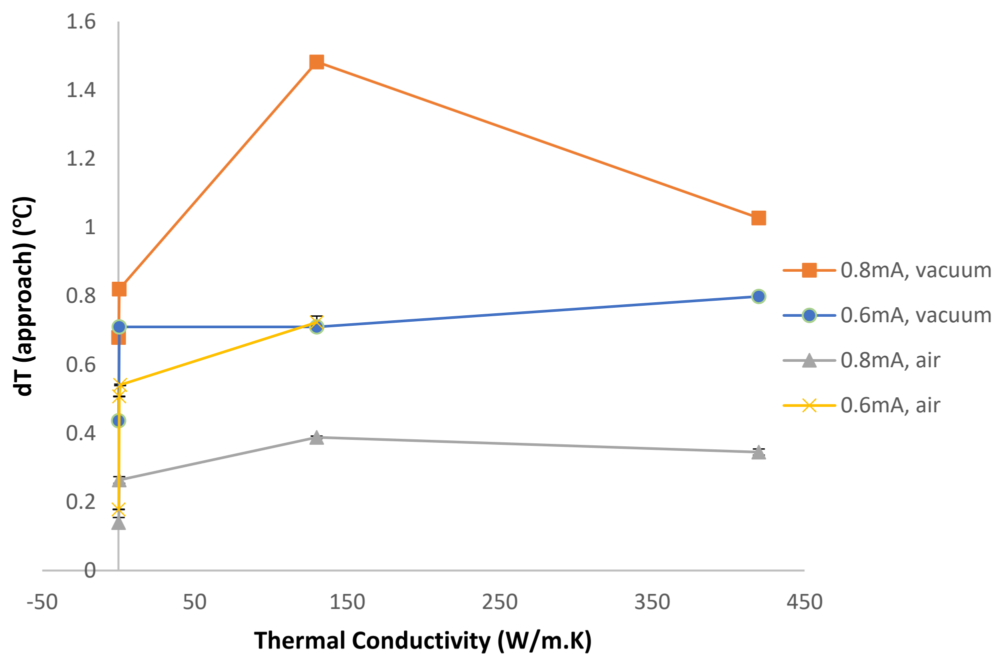

Figure 5.22 The approach temperature change against the thermal conductivity.

Figure 5.22 shows all samples in all environments at different probe currents, without the gold values. The first observation is that with the same current, the vacuum measurements are consistently larger than in air. The results in figure 5.22 was measured with three different tips (A, B and C as described in chapter 4). For the results of 0.6mA, the measurements in air and vacuum were using two different tips. The different tips could have different contact areas and can cause an inconsistency, therefore the data with the same probe current was only used to compare within the set. The data of 0.8mA was using the same tip, and so the results can be compared with different environments.

The silicon has an inconsistent result shown in figure 5.22. From the 0.8mA result, the silicon shows an approach temperature larger than the silicon carbide, while for 0.6mA the result is vice versa. There may have been surface changes to the sample or the tip. Although it is also the case that when the thermal sensitivity of the tip is similar to the sample, the tip reaches a limit on measuring the change in temperature. [12] The shape of the curve showed that there is a limit towards the higher thermal conductivity. Since the range of thermal conductivity is large, in order to compare mica and PTFE, the graph was replotted with a smaller horizontal.

Figure 5.23 shows the range of thermal conductivity for the samples with a smaller thermal conductivity, the vacuum results remained consistently larger than air.

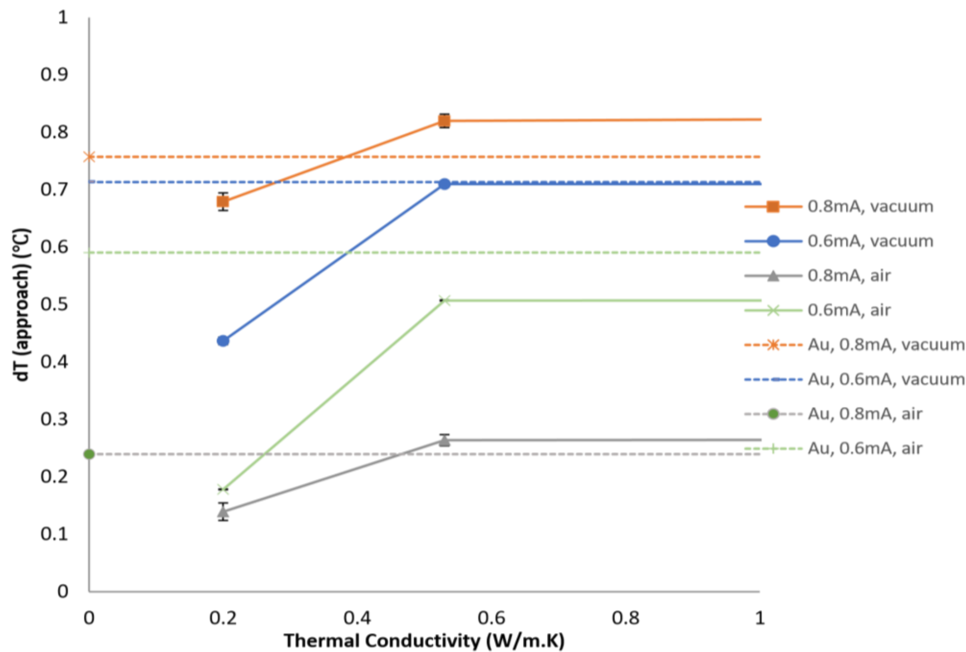

Figure 5.23 The approach temperature change against the thermal conductivity for small thermal conductivity. The gold is shown as a horizontal line as the thermal conductivity is not known.

The PTFE change in temperature is smaller than mica in all environments. The error in figure 5.23 shows more clearly than in figure 5.22, since the standard deviation of the samples are small in figure 5.22 the error bars are negligible. However, there are some inconsistencies from the gold and silicon result that are noticeable. Therefore, the reproducibility of the measurements is much poorer than the standard deviation is implying.

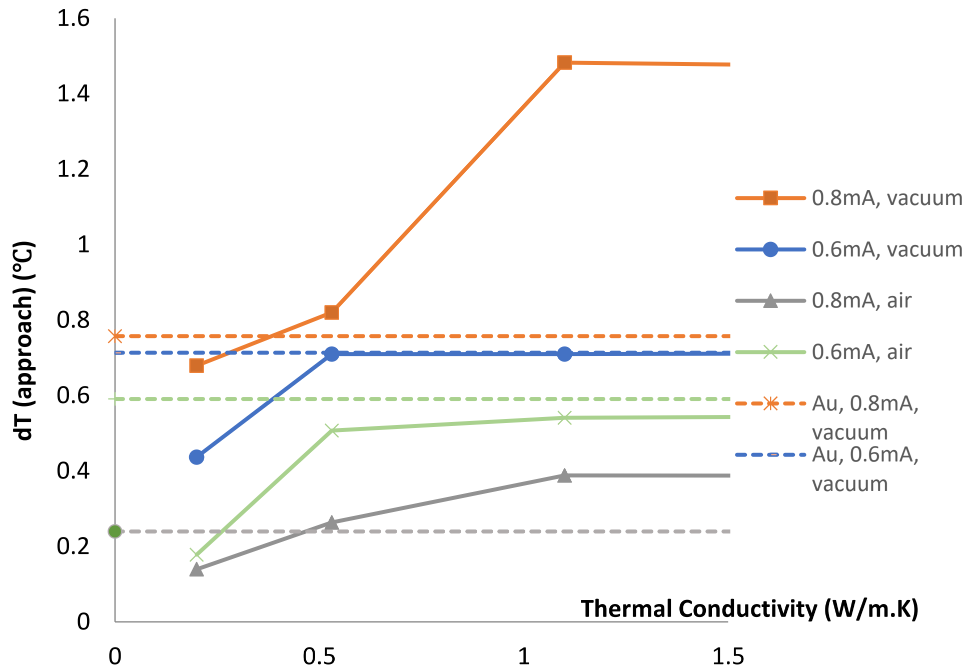

Figure 5.24 The approach temperature change against the thermal conductivity for small thermal conductivity. The silicon values have plotted with the silicon oxide thermal conductivity of 1.1 W/m·K.

Figure 5.24 has an additional point from figure 5.23, it has the silicon plotted with the silicon oxide thermal conductivity of 1.1 W/m·K. The reason is since the silicon is known to have a layer of silicon oxide on the surface, the heat transfer could be from the tip to the silicon oxide and the silicon change in temperature could be different from the measured value. With the silicon oxide thermal conductivity, the change in temperature was observed to have a better linear correlation with the lower range of thermal conductivity. However, the silicon oxide and silicon samples would need to be modelled and compared for a more conclusive deduction.

The discussion is now the thermal conductivity of the thin film gold. The gold thin film is believed to have a similar thermal conductivity as mica, since the mechanical and thermal results were similar. In the previous discussion on the tip sensitivity, the tip becomes less thermally sensitive when the thermal conductivity of the sample is comparable to the tip, however with low thermal conductivity materials, the temperature drop is dependent on the thermal conductivity.

The thermal conductivity of the thin film gold is estimated by comparing the percentage difference of the change in temperature with the thermal conductivity of mica. The gold change in temperature was first calculated as a percentage range of mica, which gives a 16% difference. The gold thin film thermal conductivity is estimated at the range of 0.44 – 0.62 W/ m·K, compared to the bulk material of 314 W/ m·K. The thin film value was expected to be much smaller than the bulk material due to the geometric constraints. [1] The thermal conductivity estimation of this gold thin film sample is likely to be due in part to its structure and surface, for example, the size of surface features, the thickness and roughness. Further investigation on thin film samples would require modelling layers of different materials, in this gold thin film example, the layer of silicon oxide on the silicon base and the chromium adhesive should also be modelled.

Chapter 6 Conclusions and further developments

This chapter will summarise the work completed, the results achieved and suggest future developments for this project.

Different methods for measuring the spring constant of the AFM cantilever were considered and the SEM method chosen and used due to its practicality. The spring constant for the thermal tips has successfully been measured as a range of $0.5 - 2.6\ \mathrm{N/m}$ and the contact tip spring constant has been measured as $23.1\ \mathrm{N/m}$. The spring constant of the contact tip has been shown to have a much higher spring constant than the thermal tip. The spring constant has been used in converting deflection to force units. One challenge for this is there are impurities on the cantilever, for which the effect on the spring constant is unknown. The Young’s modulus was estimated as that of silicon nitride, as the structure of the probes gets more complex, the Young’s modulus can directly affect the spring constant calculated. The thermal resistor was found to be peeling off from the tip after an experiment. Hence the tip verification using SEM was added as a standard procedure before thermal experiments.

The methodology of force and thermal measurements were presented in Part II of chapter 3. The topography, force and thermal measurements for each sample were presented in Chapter 4 and Chapter 5. For some samples having a high adhesive force such as silicon, the AFM reached a limit regardless of the measurement environment. A method for obtaining the adhesive force from this data was suggested using a line of best fit of the data, which inevitably introduced an additional error. Some force curves also could not be fitted with a straight line, due to deformation of the surface. The other method suggest was offsetting the range on the AFM, this then revealed a force curve with an unusual shape which it is thought is caused by a surface layer, which could be contamination, or an instrumental effect.

A method of thermal calibration of the thermal tips was presented. The data logger was used to monitor the potential of the tip and the temperature signal from the PT100 thermometer. For the thermal calibration, a hysteresis was observed between the heating and the cooling in both air and vacuum. Various calibration methods were attempted for vacuum however, the conversion coefficient was shown to be 20 times smaller than calibration in air due to the poorer thermal contact between the heater. The conversion coefficient in vacuum would give a result that is overestimating the changing of temperature of the sample. It was therefore decided that the thermal calibration coefficient measured in air be used for converting the temperature signal in vacuum as well. A 40-second periodic noise was observed throughout the experiment in vacuum. The conversion factor was measured as 0.124 V/℃, this was used for converting the signal to temperature for the results in chapter 5. In the thermal map analysis, a 40-second noise was also observed across the images. The thermal probe holder broke during the experiment due to the heavy usage on the SThM. The probe holder was consequently improved by having extra glue placed at the gold pin to increase the strength for secure the tip, however further design improvements are desirable.

The thermal measurements showed that the retract changes of temperature are not consistent for interpretation due to the effect of the adhesive force, therefore the approach temperature should be used for interpreting the material properties. In the last discussion on the force curves, a contamination layer of material was shown to affect the thermal curve as well. The contamination layer could be oxidized material or a thin layer of liquid. This leads to a discussion on the approach temperature. When there is a layer of material on the surface while making the thermal measurement, the tip will first arrive at the contamination material before reaching the sample, the contamination material can cause a change in temperature and provide a misleading impression of the measurement. Thermal modelling, for example using a simulation program such as COMSOL, is necessary to interpret multilayer effects.

The topography was measured on scan areas of 500nm x 500nm. A spatial resolution of approximately 20nm for both the topography and thermal measurements was achieved. This provides a much better spatial resolution for thermometry than traditional methods. The data was repeated at three different points and three repeated measurements at each point. The idea was to measure the variation of the measurements across the surface. The error on the adhesive force and temperature has been shown to be small in general. However, for samples with a soft surface such as PTFE, the roughness variation of 33% was shown to be large across the different areas on the same scan indicating a large distribution in both adhesive force and temperature measurements. Recording the change in tip temperature as the tip presses into the sample also gives a measure of sample hardness, it has shown that for the soft surface, there is a larger deformation temperature. The PTFE has shown a range 23-119% of deformation-approach temperature ratio. The gold sample has shown to have a soft surface with the deformation temperature of 39-75%.

The comparison between each sample was presented in both chapter 4 and 5, as well as a comparison of measurements made in air and vacuum. The results showed that there is a 90% heat loss of heat from the tip to the air in ambient conditions, whilst the losses are only about 10% in vacuum. This suggests that the vacuum environment can provide a better temperature signal as the temperature difference between the tip and the sample is greater leading to a larger temperature drop despite losing the solid-liquid conduction path. It was demonstrated across all sample sets that the temperature drop in vacuum was greater than in air.

Silicon carbide was the hardest material from the sample set, and does have the highest thermal conductivity. The mechanical and thermal properties gave consistent results in general, however, the adhesive force was smaller than expected when compared to silicon and mica. The change in temperature was also expected to have a higher value than observed, due to its

high thermal conductivity. The silicon carbide has a similar roughness to silicon, the average height for the silicon carbide is 1.7nm while the silicon has 1.2nm. Both samples exhibited an interference while measuring the topography.

The silicon gave the unusual shape when measuring the adhesive force which may be due to the silicon oxide layer. The temperature drop was less consistent than the silicon carbide and similar to mica. This may be a result of the additional layer of silicon oxide reducing the value of thermal conductivity.

The PTFE is the softest material and had the lowest thermal conductivity from the sample set. The soft surface of PTFE caused a large variation for both force and thermal measurements. The adhesive force was shown to be low as expected. However, the PTFE showed the force curves have shown an unusual shape in all environments. The possible reasons could be the moisture left on the surface, or the sample surface deforming during the measurements. Another possible reason is the PTFE absorbed the isopropanol that has applied for cleaning however, further investigation would be required to test this. Although the deformation from PTFE caused a big variation when measuring the approach temperature, the PTFE has the lowest value of temperature drop for all environment.

The mica results were consistent being at the centre of each scale. The mica is expected to be the cleanest sample, due to the layered structure, mica is cleaned by simply cleaving the top layer. However, the surface features could not be seen from the topography because of the smooth surface, only some features were detected in the vacuum topography measurements. The thermal properties are similar to gold, and consistently larger than the PTFE.

The thin film gold is known to have a 150nm thickness, it is the targeted material for estimating the thermal conductivity. The thin film gold surface was shown to be islanded due to the

evaporation process and appeared very different to the other bulk materials. Both the force and thermal results are similar to mica, which implied that the range of thermal conductivity would also be similar to mica. The curve of approach temperature against the thermal conductivity was then plotted in chapter 5. The gold thin film thermal conductivity was estimated to be in the range of 0.44 – 0.62 W/m·K. The thermal conductivity of thin film gold is expected to have a smaller value to bulk material due to size effects.

This project has explored the use of SThM and provided an experimental procedure for quantitative measurements using the SThM. There are some key results that could improve the future development for the SThM at the University of York, and possible directions for future research.

One of the key outcomes of this project is to examine the tip condition before performing any experiment. This thesis has shown that the condition of the tip could vary during the experiment. Using the SEM for inspection is suggested as a standard routine.

Most significantly, the vacuum environment was shown to provide a larger temperature drop and has a potential to achieve higher resolution than air because of absence of water meniscus formed. The flatter curve gives a more accurate representation of the sample change in temperature. The pressure of the vacuum was left until it stabilized, it would be interesting to see the effect on the same sample with different pressure.

When recording the temperature change, the experimenter should monitor the sample temperature from the data logger. This thesis has shown that the sample can sometimes still be cooling during the experiment adding an additional error, particularly in vacuum, where the cooling paths are limited. In addition, it would be useful to mark the area on the sample for reproducibility by returning to the same area.

The probe holder was shown to not be very robust under frequent use. The design of the holder could be improved by following the similar design to the standard AFM holder, where a wire is used to lock the tip position rather than slotting it in. This could reduce the chance for the probe hitting the gold pin during the insertion process and improve the durability.

There are several areas that could possibly develop in the future from this research. The sample selection could be expanded by including samples with thermal conductivity between mica and silicon. This could provide more evidence for the relationship between the change in temperature and thermal conductivity. The direction of using different materials as the tip resistor would be an interesting research. The tip used in this project was a palladium resistor, which has the thermal conductivity about 70W/m·K. From the results, the probe reached the sensitivity limit when the sample thermal conductivity is similar or higher than the tip. If the thermal conductivity of the tip material is increased, it could potentially increase the range of materials which can be studied to higher thermal conductivity samples. The result has highlighted the impact on the thermal transport measurements due to the material properties.

For example, the surface structure such as islands on a thin film, the dimensions such as bulk material and thin film material all affect the measurements. The surface properties such as the silicon oxide can also impact on the surface thermal properties. Modelling is needed to further interpret the data, however there is a potential to apply the technique to study these effects.

In summary, this thesis has achieved the objectives for exploring the potential of using an SThM for quantitative thermal measurements. If the points raised in this thesis are put into practice, then the SThM can be successfully used to measure the thermal properties with a spatial resolution of approximately 20nm, with the temperature resolution up to 0.01℃. The range of thermal conductivities which can be measured is limited to the tip properties, currently 70 W/m·K.

List of reference

[1] D. Zhao, “Measurement Techniques for Thermal Conductivity and Interfacial Thermal Conductance of Bulk and Thin Film Materials,” J. Electron. Package, no. 4, p. 138, 2016.

[2] G. Chen, “Nanoscale Energy Transport and Conversion,” Oxford University Press, 2005.

[3] J. Christofferson, D. Vashaee and A. Shakouri, "Real Time Sub-micron Thermal Imaging Using Thermoreflectance," Defense Technical Information Center, 2001, 2001.

[4] F. Menges, P. Mensch, H. Schmid, H. Riel, A. Stemmer, B. Gotsmann, “Temperature Mapping of Operating Nanoscale Nevices by Scanning Probe Thermometry," Nature Communication , vol. 7, no.10874, 10 Sep 2015.

[5] G. Binnig, “Atomic Force Microscope,” USA: IBM San Jose Research Laboratory, 1986.

[6] G. Binnig, “Scanning Tunneling Microscopy,” Switzerland: IBM Zurich Research Laboratory, 1983.

[7] P. Eaton, “Atomic Force Microscopy”, Oxford Scholarship Online, 2010.

[8] A. Majumdar, "Scanning Thermal Microscopy," Annual Review of Material Science, vol. 29, no. 1, pp. 505-585, 1999.

[9] C. Williams, H. Wickramasinghe, "Scanning Thermal Profiler," Appl. Phys. Lett. , vol. 49, no. 23, pp. 1587-1589, 1986.

[10] Department of Pharmacology, University of Virgina, [Online]. Available: https://pharm.virginia.edu/files/2014/01/AFM2.jpg. [Accessed 11 10 2017].

[11] V. Gorbunov, "Probing Surface Microthermal Properties by Scanning Thermal Microscopy," Langmuir, vol. 15, no. 24, pp. 8340-8343, 1999.

[12] S. Gomès, "Scanning Thermal Microscopy: A Review," Phys. Status Solidi, vol. 212, no. 3, pp. 477-494, 2015.

[13] L. Shi, A. Majumdar, “Thermal Transport Mechanism at Nanoscale Point Contacts," J. Heat Transfer, vol. 124, no. 2, pp. 239-337, 2001.

[14] P. Hawkes, “Advances in Imaging and Electron Physics", France: Elsevier, 2015.

[15] P. Dobson, J. Weaver and G. Mills, "New Methods for Calibrated Scanning Thermal Microscopy (SThM)," in Sensors, IEEE, 2007.

[16] R. Pylkki, "Scanning Near-field Optical Microscopy and Scanning Thermal Microscopy," Japanese Journal of Applied Physics, vol. 33, pp. 3785-3790, 1994.

[17] S. Gomès, "DC Thermal Microscopy: Study of the Thermal Exchange Between A Probe and A Sample," Measurement Science and Technology, vol. 10, pp. 805-811, 1999.

[18] " Scanning Thermal Microscopy (SThM)," Park system, [Online]. Available: http://www.parkafm.com/index.php/park-spm-modes/99-thermal-properties/252-scanning-thermal-microscopy-sthm%0A.. [Accessed 11 10 2017].

[19] P. Tovee, "Nanoscale Spatial Resolution Probes for Scanning Thermal Microscopy of Solid State Materials," Journal of Applied Physics, vol. 112, no. 11, 114317, 2012.

[20] J. Weaver. et. al., "Microelectronic Engineering Batch Fabricated Dual Cantilever Resistive Probe for Scanning Thermal Microscopy," Microelectronic Engineering, vol. 88, no. 8, pp. 2435-2438, 2011.

[21] C. Prater, "Nanospectroscopy and Nanospectrometry - Using Heat to Map Materials at Nanoscale," in University of York, York, UK, 2016.

[22] B. Robinson, "Correlation of Heat Transport and Shear Forces in Nanoscale Junctions," in University of York, York, UK, 2016.

[23] F. Menges, Heike Riel, A. Stemmer, B. Gotsmann, "Nanoscale Thermometry by Scanning Thermal Microscopy," Review of Scientific Instruments, vol. 87, 2016.

[24] K. Kim, W. Jeong, W. Lee, P. Reddy, "Ultra-High Vacuum Scanning Thermal," ACS Nano, vol. 6, no. 5, pp. 4248-4257, 2012.

[25] S. Poon, "Thermal Imaging and Magnetotransport on the Nanoscale?," in University of York, York, UK, 2016.

[26] K. Luo, Z. Shi, A. Majumdar, "Sensor Nanofabrication, Performance, and Conduction Mechanisms in Scanning Thermal Microscopy," Journal of Vacuum Science & Technology B: Microelectronics and Nanometer Structures, vol. 15, no. 2, p. 349, 1997.

[27] J. Booth, "Defining the Role of Gas Conduction in Scanning Thermal Microscopy," University of Glasgow, 2013.

[28] JPK Instruments, "A Practical Guide to AFM Force Spectroscopy and Data Analysis," JPK Instruments, [Online]. Available: https://www.jpk.com/app-technotes-img/AFM/pdf/jpk-tech-force-spectroscopy.14-2.pdf. [Accessed 02 01 2018].

[29] Instructions JSPM-5200 Scanning Probe Microscope, Japan: JEOL, 2005.

[30] M. Poggi, "A Method for Calculating the Spring Constant of Atomic Force Microscopy Cantilevers with a Nonrectangular Cross Section," Analytical Chemistry, vol. 77, no. 4, p. 1192, 2005.

[31] J. Cleveland, S. Manne, "A Nondestructive Method for Determining the Spring Constant of Cantilevers for Scanning Force Microscopy," Review of Scientific Instruments, vol. 64, no. 2, p. 403, 1993.

[32] J. Sader, J. Chon, P. Mulvaney, "Calibration of Rectangular Atomic Force Microscope Cantilevers," Review of Scientific Instruments, vol. 70, no. 10, p. 3967, 1999.

[33] A. Torii, M.Sasaki, K. Hane, "A Method for Determining the Spring Constant of Cantilevers for Atomic Force Microscopy," Measurement Science and Technology, vol. 7, no. 2, p. 179, 1999.

[34] J. Weaver, [Private Communication], UK, 2006.

[35] "Material Property Data," MatWeb, [Online]. Available: http://www.matls.com/. [Accessed 11 10 2017].

[36] "Material: Silicon (Si), Bulk - MEMS Clearinghouse," Memsnet, [Online]. Available: https://www.memsnet.org/material/siliconsibulk/. [Accessed 11 10 2017].

[37] "Properties Handbook - Teflon PTFE," DuPont Fluoroproducts:, [Online]. Available: http://www.rjchase.com/ptfe_handbook.pdf. [Accessed 11 10 2017].

[38] M. Hopcroft, W, Nix, T. Kenny, "What is the Young's Modulus of Silicon?," Journal of Microelectromechanical Systems, vol. 199, no. 2, p. 229, 2010.

[39] A. Vick, [Private Communication], UK, 2016.

[40] "F-d Spectroscopy," Park AFM, [Online]. Available: http://www.parkafm.com/images/spmmodes/Force/Force-Distance-Spectroscopy.pdf. [Accessed 11 10 2017]